SENSING TECHNOLOGY FOR DAMAGE ASSESSMENT OF SIGN SUPPORT STRUCTURES

by

Xuan Zhu

B. S. in Mechanical Engineering,

Beijing University of Aeronautics and Astronautics, Beijing, China, 2008

Submitted to the Graduate Faculty of

Swanson School of Engineering in partial fulfillment

of the requirements for the degree of

Master of Science in Civil Engineering

University of Pittsburgh

2010

UNIVERSITY OF PITTSBURGH

SWANSON SCHOOL OF ENGINEERING

This thesis was presented

by

Xuan Zhu

It was defended on

August 20, 2010

and approved by

Albert To, PhD, Assistant Professor

Kent A. Harries, PhD, Associate Professor

Thesis Advisor: Piervincenzo Rizzo, Ph.D., Assistant Professor

STRUCTURAL HEALTH MONITORING OF HIGHWAY SIGN SUPPORT STRUCTURES

Xuan Zhu, M. S.

University of Pittsburgh, 2010

In the last few years the use of guided ultrasonic waves (GUWs) for the health monitoring of engineering structures increased rapidly, with the most recent studies focusing on the application of GUWs to complex structures or under varying environmental conditions. In fact, the health monitoring of complex structures is complicated because of reflections, scattering, and mode conversion. In addition, sensitivity to temperature and surface wetting can degrade the performance of a GUW-based structural health monitoring system.

This thesis presents the results of an experimental investigation where GUWs and the Electro-mechanical Impedance (EMI) method were used for the health monitoring of a truss, which was part of a highway variable message structure removed from service and tested in laboratory. The monitoring strategy proposed here combines the advantages of GUWs and EMI with the extraction of defect-sensitive features to perform a multivariate diagnosis of damage. The effectiveness of the presented approach is tested by monitoring the propagation of waves along one of the main chords of the truss and by observing the onset and growth of two artificial cracks. The ability to diagnose the presence of these defects located around the welds that join two diagonal angular members to the chord is discussed.

In the last portion of the thesis, the results from field application are presented. Two overhead sign support structures deployed along I-279 were monitored by using the proposed SHM methodology developed in laboratory.

TABLE OF CONTENTS

PREFACE ..... **xv**

1.0 INTRODUCTION **1**

1.1 PROBLEM STATEMENT AND MOTIVATION 1

1.2 SCOPE OF WORK 5

1.3 THESIS OUTLINE 5

2.0 NONDESTRUCTIVE TESTING METHODS **7**

2.1 CURRENT METHODS 7

2.1.1 Visual inspection 7

2.1.2 Liquid penetrant 8

2.1.3 Magnetic particle inspection 10

2.1.4 Ultrasonic Testing 12

2.2 POTENTIAL INSPECTION/MONITORING TECHNIQUES **13**

2.2.1 Eddy Current 14

2.2.2 X-ray 15

2.2.3 Guided ultrasonic waves 16

2.2.4 Acoustic Emission 17

2.2.5 Electromechanical Impedance 18

2.3 SUMMARY AND CONCLUSIONS 19

3.0 LABORATORY TESTS 20

3.1 THE STRUCTURE 20

3.2 HARDWARE – SOFTWARE – SETUP 24

3.2.1 The sensors 24

3.2.2 The Data Acquisition System 24

3.2.3 Test Protocol 1 29

3.2.4 Test Protocol 2 32

3.2.5 Test Protocol 3: Environmental Test 33

3.3 DIGITAL SIGNAL PROCESSING 39

3.3.1 UGW-related Signal Processing Algorithm 39

3.3.2 EMI-related Signal Processing Algorithm 47

4.0 EXPERIMENTAL RESULTS FROM UGWS 48

4.1 TEST 1 48

4.1.1 Univariate Analysis 48

4.1.2 Multivariate Analysis 52

4.1.3 Multiple frequencies analysis 56

4.2 TEST 2 63

4.3 TEST 3 68

5.0 EXPERIMENTAL RESULTS FROM EMI 82

5.1 LOW-COST CIRCUITRY 82

5.2 EMI-RELATED SIGNAL PROCESSING ALGORITHM 87

5.3 EXPERIMENTAL RESULTS: LABORATORY TEST 93

6.0 FIELD TEST 97

6.1 TEST 1: SETUP 97

6.2 TEST 1: RESULTS 100

6.2.1 May tests 100

6.2.2 June tests 109

6.3 TEST 2: SETUP 113

6.4 TEST 2: RESULTS 116

7.0 CONCLUSIONS 124

7.1 DISCUSSION 124

7.2 SUMMARY OF FINDINGS 125

APPENDIX A 128

APPENDIX B 130

APPENDIX C 132

BIBLIOGRAPHY 134

LIST OF TABLES

Table 3.1 - Experimental setup configuration for Test 3. 37

Table 3.2 - Damage Index in the form of Waveform path in..... 44

Table 4.1 - Univariate Analysis: the percentage of outliers detected using statistical features applied to waveform data associated with some of the actuator-sensor pairs considered in this study……..…… 52

Table 4.2 - Test 3. Summary of boundary condition, steel temperature, and joint condition..... 68

Table 6.1 - The record of measurement environmental effect……..……..…102

Table 6.2 - Weather condition during the field test during the month of June 2010. 109

Table 6.3 - The record of temperature of the air and of the steel pole..... 117

LIST OF FIGURES

Figure 1.1 – Main sign support structure types used in Pennsylvania.(a) overhead cantilever with single pole; (b) overhead bridge truss with truss poles..... 1

Figure 1.2 - Examples of sign support structures. Clockwise from top left: overhead truss with single pole supports, cantilevered single pole, overhead truss with truss supports, cantilever with double pole, a structure mounted sign, pole mounted VMS, monotube structure. 3

Figure 1.3 - (a) Collapse of a sign structure along I-65 in Tennessee. http://updatewindowssecurity.com/?id=34452915477 (b) Cantilever Sign Structure Failure: (Source: http://www.fhwa.dot.gov/BRIDGE/signinspection03.cfm..... 4

Figure 2.1 - Steps of an inspection conducted by using liquid penetrant testing. (a) Sample before testing; (b) liquid penetrant applied; (c) surplus wiped off leaving penetrant in crack; (d) developer powder applied, dye soaks into powder; (e) View coloured indications, or UV lamp shows up fluorescent indications. (http://www.twi.co.uk/content/ksijm001.html) 9

Figure 2.2 - Magnetic particle testing of a welded area..... 12

Figure 2.3 - Bulk UT configurations. Top: pitch catch. Top right: pulse echo. Bottom right: pulse/echo with angular wedge (angle beam transduction). Photo source: http://www.olympus-ims.com/data/File/panametrics/panametrics-UT.en.pdf..... 12

Figure 2.4 - AE principles. Source: http://www.pacndt.com/index.aspx?go=research 18

Figure 2.5 - PZT bonded on aluminum and steel beams. 18

Figure 3.1 – (a) Photo of the sign support structure when in service; (b) Original location 21

Figure 3.2 – Location of cracks found during the investigation conducted in [27]. 22

Figure 3.3 - Photo of the delivery at the University of Pittsburgh. 22

Figure 3.4 - (a) 3-D rendering of the truss. (b-c) Photo of truss set onto the supports 23

Figure 3.5 - Mode of vibration of the PZTs used in this study. 24

Figure 3.6 - (a) Hardware setup for the UWG. (b) LabView program front panel created to control the UGW measurements. (c) LabView program front panel created to conduct the EMI-based experiments 26

Figure 3.7 - (a) Sketch of the truss structure. (b) Location and relative distance of PZTs S0,…,S10. (c) Close up view of PZT S5. (d) Close up view of PZT S1. Dimensions are expressed in mm. 29

Figure 3.8 - (a) Sketch of the truss structure. (b) View from the top of the joint under investigation and PZT EM1. (c-e) Close up view pf for EM1 located between two joints (d) close up view for EM2 located inner side of the chord (e) close up view for EM3 located outer side of the chord. 30

Figure 3.9 - (a) Close-up view of the artificial notch machined along the weld between the chord and one angular diagonal member. (b) Loading setup (c) Crack size and acquisition number as a function of cycle loading number. 31

Figure 3.10 - (a) Close-up view of the joint where artificial notch was machined (b) the artificial notch along the weld between the chord and one angular diagonal member. (c) Crack size and acquisition number as a function of cycle loading number. 33

Figure 3.11 - (a) Sketch of the truss structure. (b) Location and relative distance of PZTs S0,…,S4. (c) Close up view of PZT S1. (d) Close up view of PZT S3. Dimensions are expressed in mm. 34

Figure 3.12 - (a) Sketch of the truss structure. (b) View from the top of the joint under investigation and PZT EM1. 35

Figure 3.13 - (a) Close-up view of the artificial notch machined along the weld between the chord and one angular diagonal member. (b) Close-up view of enlarged crack. (c) Snowing condition 36

Figure 3.14 - Flowchart of the defect detection procedure. 40

Figure 3.15 - Time waveforms recorded at the beginning of the experimental program from actuator-sensor pairs: (a) S5=>S4 (b) S5=>S8 (c) S5=>S0 (d) S9=>S6 (e) S0=>S4 (f) S1=>S4 (g) S9=>S0 (h) S9=>S1 (i) S5=>S6 (j) S6=>S5 (k) S6=>S4 (l) S6=>S9 (m)S9=>S8 (n) S6=>S7 (o) S0=>S5 (p) S0=>S1. 42

Figure 3.16 - Statistical features as a function of the loading number of cycles. (a) RMS S5=>S4 (b)Ppk S5=>S4 (c) RMS S5=>S8 (d) Ppk S5=>S8 (e) RMS S5=>S0 (f) Ppk S5=>S0 (g) RMS S9=>S6 (h) Ppk S9=>S6. 45

Figure 4.1 - Univariate analysis. Discordancy as a function of the crack size for the following features andactuator-sensor pairs: (a) RMS_S5=>S8/S5=>S4 (b) Ppk_S5=>S8/S5=>S4; (c) RMS_S9=>S6/S9=>S8 (d) Ppk_S9=>S6/S9=>S8 (e)

RMS_S5=>S0/S5=>S4 (f) Ppk_S5=>S0/S5=>S4; (g) RMS_S5=>S6/S5=>S4 (h) Ppk_S5=>S6/S5=>S4 (i) RMS_S5=>S1/S5=>S4 (j) Ppk_S5=>S1/S5=>S4; (k) RMS_S0=>S4/S0=>S2 (l) Ppk_S0=>S4/S0=>S2 (m) RMS_S0=>S5/S0=>S1 (n) Ppk_S0=>S5/S0=>S1; (o) RMS_S0=>S4/S0=>S1 (p) Ppk_S0=>S4/S0=>S1 (q) RMS_S9=>S1/S9=>S8 (r) Ppk_S9=>S1/S9=>S8; 51

Figure 4.2- Multivariate analysis. Mahalanobis squared distances as a function of the crack size for theactuator-sensor pairs considering all 7 features: (a) S5=>S0/S5=>S4; (b) S9=>S6/S9=>S8; (c) S5=>S8/S5=>S4; (d) S5=>S6/S5=>S4; (e) S5=>S1/S5=>S4; (f) S0=>S4/S0=>S2; (g) S0=>S5/S0=>S1; (h) S0=>S4/S0=>S1..... 54

Figure 4.3 - Multivariate analysis. Mahalanobis squared distances as a function of the crack size for the..... 55

Figure 4.4 - Time waveforms of S5=>S0 in different frequencies: (a) 100 KHz; (b) 125 KHz; (c) 150 KHz; (d) 175 KHz; (e) 200 KHz; (f) 225 KHz; (g) 250 KHz; (h) 275 KHz..... 59

Figure 4.5 - Univariate analysis. Detection rate as a function of frequency for the following features: (a) S5=>S0/S5=>S4 (b) S5=>S6/S5=>S4; (c) S5=>S8/S5=>S4 (d) S0=>S4/S0=>S1 (e) S6=>S5/S6=>S7 (f) S0=>S5/S0=>S1..... 62

Figure 4.6 - MSD considering all 7 features: path (1) S5=>S0/S5=>S4; (2) S9=>S6/S9=>S8; (3) S5=>S8/S5=>S4; (4) S5=>S6/S5=>S4; (5) S5=>S1/S5=>S4; (6) S0=>S4/S0=>S2; (7) S0=>S5/S0=>S1; (8) S0=>S4/S0=>S1;..... 63

Figure 4.7 - Multivariate analysis. Mahalanobis squared distances as a function of the crack size for the actuator-sensor pairs considering all 7 features: (a) S9=>S6/S9=>S8; (b) S9=>S1/S9=>S8; (c) S5=>S6/S5=>S4; (d) S5=>S1/S5=>S4; (e) S0=>S4/S0=>S2; (f) S0=>S5/S0=>S1; (g) S0=>S4/S0=>S1; (h) S5=>S0/S5=>S4..... 66

Figure 4.8 - Multivariate analysis. Mahalanobis squared distances as a function of the crack size for the actuator-sensor pairs: (a) S1=>S4/S1=>S2 with rms and var (b) S0=>S5/S0=>S1 with krt, var, cf, kf, and ppk (c) S1=>S5/S1=>S2 with krt, var, cf, and kf (d) S9=>S6/S9=>S8 with rms, var, cf, and ppk; (e) S0=>S4/S0=>S2 with rms and var; (f) S1=>S4/S1=>S2 with krt and max;(g) S5=>S0/S5=>S4 with krt, rms, kf, max and ppk; (h) S5=>S6/S5=>S4 with krt, rms, var, cf, kf, and max. 67

Figure 4.9– Root Mean Square values as a function of the measurement number for: (a) S3=>S4/S3=>S2; (b) S3=>S0/S3=>S2; (c) S0=>S3/S0=>S1; (d) S0=>S4/S0=>S1. 70

Figure 4.10 – Test 3. RMS for path: (a) S3=>S2; (b) S0=>S1; (c) Normalized RMS for S0=>S1 (red circles) and S3=>S2 (black dots) 72

Figure 4.11 – Test 3. Path S3=>S2 (a) K–factor, (b) peak-to-peak. Path S0=>S1 (c) K–factor, (d) peak-to-peak. 73

Figure 4.12– Test 3. Path S3=>S2 (a) variance, (b) maximum. Path S0=>S1 (c) variance, (d) maximum. 74

Figure 4.13 – Test 3. Path S3=>S2 (a) crest factor, (b) kurtosis. Path S0=>S1 (c) crest factor, (d) kurtosis..... 74

Figure 4.14 – Damage Index as a function of the measurement number associated with six features. (a) Ratio S3=>S4 /S3=>S2. (b) Ratio S0=>S4 / S0=>S1. The value of the temperature at each measurement number is scaled on the y-axis on the right..... 75

Figure 4.15 – Percentage variation of the damage index as a function of the measurement number associated with six features with respect to the value calculated during the first measurement. (a) Ratio S3=>S4 /S3=>S2. (b) Ratio S0=>S4 / S0=>S1. The value of the temperature at each measurement number is scaled on the y-axis on the right..... 76

Figure 4.16 – Time waveforms generated by actuator S3 and sensor S2. From top to bottom: measurement number 1. 25. 61, 68..... 78

Figure 4.17 – Time waveforms generated by actuator S3 and sensor S4. From top to bottom: measurement number 1. 25. 61, 68..... 79

Figure 4.18 - Multivariate analysis. Mahalanobis squared distances as a function of the measurement number considering all 7 features for: (a) S3=>S4/S3=>S2; (b) S3=>S0/S3=>S2; (c) S0=>S3/S0=>S1; (d) S0=>S4/S0=>S1..... 80

Figure 4.19 – MSD as a function of measurement number for paths (a) C3=>C4/C3=>C2, (b) C3=>C0/C3=>C2, (c) C0=>C3/C0=>C1, and (d) C0=>C4/C0=>C1. The first 51 measurements were considered as baseline..... 81

Figure 5.1 – Design of the circuit and its connection to the PXI for EMI measurement..... 82

Figure 5.2 – Comparative study between LCR and low-cost circuit conducted on PZT. Results from PXI and LCR meter for (a) Conductance and (b) Susceptance as a function of frequency; Results from PXI of different measurements for (c) Conductance and (d) Susceptance as a function of frequency..... 84

Figure 5.3 - Design of the circuit and its connection to the PXI and the switch for multiple EMI measurement..... 84

Figure 5.4 – Hardware for the EMI measurement. (a) PXI, switch module, terminal block and screw terminal. (b) Inside view of the screw terminal..... 86

Figure 5.5 - (a) Conductance resulted from PXI and LCR meter for EM1 bonded with the truss structure; (b) Susceptance resulted from PXI and LCR meter for EM1 bonded with the truss structure..... 87

Figure 5.6- Connection topology adopted for the NI Switch front panel and first PZT. 87

Figure 5.7 - Flowchart of the defect detection procedure 88

Figure 5.8 - (a) Conductance signature for EM1 resulted from PXI at 5 different periods; (b) Conductance signature for EM2 resulted from PXI at 5 different periods. 89

Figure 5.9 - RMSD values from 100 KHz to 500 KHz of (a) EM1; (b) EM2 90

Figure 5.10 - Statistical features as a function of the loading number of cycles. (a) Var EM1; (b) Var EM2; (c) RMS EM1; (d) RMS EM2; (e) Krt EM1; (f) Krt EM2; (g) Peak EM1; (h) Peak EM2; (i) Skw EM2; (j) Skw EM1; (k) Area EM2; (l) Area EM1. 92

Figure 5.11 - Multivariate analysis. Mahalanobis squared distances as a function of the cycle number considering all seven features for: (a) EM1; (b) EM2. 94

Figure 5.12 - Multivariate analysis. Mahalanobis squared distances as a function of the cycle number for: (a) EM1 with krt, rms, peak, area, skw, var and rmsd (b) EM1 with krt, peak, area, var and rmsd (c) EM1 with krt, rms, peak and skw (d) EM1 with peak, area and rmsd; (e) EM2 with rms, peak, area and skw; (f) EM2 with krt, rms, peak, area, skw, var and rmsd;(g) EM2 with peak, skw and var ; (h) EM2 with peak, area and rmsd. 95

Figure 6.1 - (a) Photo of the structure monitored in the field. (b) particular of the welded connections 98

Figure 6.2 - (a) Photo of the structure. (b) Close-up view of the part that was monitored. (c) Location of the sensing system. The red circles show the joints involved in the field test. Distances are expressed in mm. 99

Figure 6.3 – Field testing. (a) Photo of the data acquisition system. (b-c) Bonding the PZTs to the structures. (d) Connecting the coaxial cables to the screw terminal. 99

Figure 6.4 the original time waveforms of (a) S0=>S2; (c) S0=>S5; (e) S0=>S3; (g) S1=>S3; (i) S5=>S0; and the filtered time waveforms of (b) S0=>S2; (d) S0=>S5; (f) S0=>S3; (h) S1=>S3; (j) S5=>S0; 103

Figure 6.5 the magnitude and phase response of the simulated Butterworth band pass filter ... 104

Figure 6.6 RMS Damage Index at May from path: (a) C0=>C2/C0=>C5; (b) C0=>C3/C0=>C5; (c) C1=>C3/C0=>C5 and (d) C5=>C0/C0=>C5 105

Figure 6.7 - K factor Damage Index at May from path: (a) C0=>C2/C0=>C5; (b) C0=>C3/C0=>C5; (c) C1=>C3/C0=>C5 and (d) C5=>C0/C0=>C5 106

Figure 6.8 - Variance Damage Index at May from path: (a) C0=>C2/C0=>C5; (b) C0=>C3/C0=>C5; (c) C1=>C3/C0=>C5 and (d) C5=>C0/C0=>C5 107

Figure 6.9 - Considering all 7 features MSD from path: (a) C0=>C2/C0=>C5; (b) C0=>C3/C0=>C5; (c) C1=>C3/C0=>C5 and (d) C5=>C0/C0=>C5 108

Figure 6.10 - RMS DI at June from path (a) C0=>C2/C0=>C5; (b) C0=>C3/C0=>C5; (c) C1=>C3/C0=>C5 and (d) C5=>C0/C0=>C5 110

Figure 6.11 - K factor DI at June from path (a) C0=>C2/C0=>C5; (b) C0=>C3/C0=>C5; (c) C1=>C3/C0=>C5 and (d) C5=>C0/C0=>C5 111

Figure 6.12 - Variance DI at June from path (a) C0=>C2/C0=>C5; (b) C0=>C3/C0=>C5; (c) C1=>C3/C0=>C5 and (d) C5=>C0/C0=>C5 112

Figure 6.13 – (a) Photo of the structure monitored in the field, the red circle shows the joint involved in the experiment. (b) Particular of the welded connections 114

Figure 6.14 - (a) Close-up view of the part that was monitored. (b) Location of the sensing system. The red arrows shows the diagonal members involved in the field test. (c) Close-up view of S0. (d) Close-up view of S1. (e) Close-up view of S2. Distances are expressed in mm. 115

Figure 6.15 - Field testing: (a) Set up the safety rope. (b) Measuring the geometry of the trusses. 116

Figure 6.16 - The original time waveforms of 175 kHz for paths: (a) S0=>S2; (c) S0=>S3; (e) S3=>S4; (g) S3=>S5; (i) S3=>S6; (k) S1=>S0 and the filtered time waveforms of (b) S0=>S2; (d) S0=>S3; (f) S3=>S4; (h) S3=>S5; (j) S3=>S6; (l) S1=>S0 at the fourth measurement on June 17th 120

Figure 6.17 - RMS Damage Index at June from path: (a) S0=>S2/S3=>S0; (b) S0=>S3/S3=>S0; (c) S3=>S4/S3=>S0; (d) S3=>S5/S3=>S0; (e) S3=>S6/S3=>S0 and (f) S1=>S0/S3=>S0 121

Figure 6.18 - K factor Damage Index at June from path: (a) S0=>S2/S3=>S0; (b) S0=>S3/S3=>S0; (c) S3=>S4/S3=>S0; (d) S3=>S5/S3=>S0; (e) S3=>S6/S3=>S0 and (f) S1=>S0/S3=>S0 122

Figure 6.19 - Variance Damage Index at June from path: (a) S0=>S2/S3=>S0; (b) S0=>S3/S3=>S0; (c) S3=>S4/S3=>S0; (d) S3=>S5/S3=>S0; (e) S3=>S6/S3=>S0 and (f) S1=>S0/S3=>S0 123

PREFACE

I would like express my thanks to Dr. Piervincenzo Rizzo for his guidance in this project and my first two years research in U.S.. His motivation for me kept me going and he played a key part in getting this document into its final form. I want to thank him for all of his time and input on this project.

I would also like to thank Dr. Kent Harries for his technical support and empirical guidance at the stage of experiment setup preparation which established the basis for the part of experimental study in this project. And I would like to thank Dr. Albert To for serving on my thesis defense committee and provided comments which was incredibly helpful throughout all of my research and will serve me well in my future life.

I must thank Mr. Evan Robinson for the guidance he provided in LabView programming and hardware setup. Without him I could not get where I am.

Thanks to Mr. Jerry Bruck of PennDOT for providing the necessary documents and helpful technical comments on this project. I would like to thank my Peers Mr. Venu Gopal Annamdas Mr. Tajari Mahdi and Mr. Xiangli Ni for their help and support on this project.

Lastly, I would like to thank my family for all of their love, support and encouragement.

1.0 INTRODUCTION

1.1 PROBLEM STATEMENT AND MOTIVATION

Sign support structures including cantilever, butterfly, and bridge support (also known as overhead or span type supports) can be found along any major highway across the United States. These are most commonly found on pedestals built into the highway side or median barriers or built into parapets or other parts of a bridge. These structures support signage that helps commuters navigate their way. Similarly, variable message sign (VMS) are used to control, inform, and warn the commuters through the display of a number of messages that may be changed or switched on or off as required.

Overhead cantilever signs consist of a mast arm extending out over the roadway supported by a single roadside column, typically a single or double pole or a box-truss structure. The vertical columns are sometimes referred to as uprights, posts, or poles.

Figure 1.1 – Main sign support structure types used in Pennsylvania.(a) overhead cantilever with single pole; (b) overhead bridge truss with truss poles.

The horizontal part of the structure is referred to as the mast arm (usually in reference to a monotube, that is a single tube without joints), the truss (for other than monotubes), or the cantilever. In the fourth edition of the Standard Specifications for Structural Supports for Highway Signs, Luminaires, and Traffic Signals [1], structures supported on both sides of the roadway are referred to as bridge supports. Bridge supports are also called span-type structures, sign bridges, or overhead structures (although this latter term is sometimes used to describe both cantilever and bridge supports) [2]. The roadside columns that support the mast range from single poles to box-truss structures. Each vertical upright forms a truss that is composed of two chord members braced by web members using the same pipe-to-pipe connections as in the overhead truss-type structure. Cantilevered support structures can be an attractive option because the cost is typically less than 40 percent of the cost of bridge supports. Also, the single upright increases motorist safety by reducing the probability of vehicle collision [2]. In Pennsylvania two types of overhead sign support structures are commonly used, namely the cantilever with single pole and overhead bridge truss with bridge pole.

Photos of these two structure types taken in the Pittsburgh area are shown in Fig. 1.1. Nationwide and through the years, the configuration of the full-span overhead sign supports has evolved, and today many structures consist of a truss-type structure that contains fully welded pipe-to-pipe connections [3]. A gallery of different sign support structures in provided in Fig. 1.2. Sign structures are made of structural steel and aluminum. However, aluminum structures are no longer being constructed, because steel structures have proven to be more cost effective [3].

In general, highway sign supports must withstand in-service dynamic loads, which largely constitute the fatigue environment. Sources of these loads include natural winds, seismic events (in seismic areas), artificial gusts created by passing vehicles, and vibrations induced into bridges by passing vehicles (sign supports mounted on a bridge). During the past two decades, sign structures have shown problems associated with reduced fatigue performance. Defective welds, aging material, and harsh environmental conditions have exacerbated these problems. Most of the underlying problems involve cracks induced into welds by weld-induced crack and fatigue loading. Generally, cracks are found propagating within the leg of a fillet weld or at the toe. Depending upon the amount of time the crack has to grow, these cracks can propagate into the main supporting member (e.g., the chord of a truss) [3].

Figure 1.2 - Examples of sign support structures. Clockwise from top left: overhead truss with single pole supports, cantilevered single pole, overhead truss with truss supports, cantilever with double pole, a structure mounted sign, pole mounted VMS, monotube structure.

As discussed in a report [2] for the National Cooperative Highway Research program (NCHRP), other factors that increased the number of such problems include a) the advent of backplates (used on signal fixtures to block the sun and enhance the visibility of the signal) has increased the susceptibility to galloping [4]; b) the size and location of flat panel signs —larger signs are now placed asymmetrically with their center of gravity above the center of gravity of the horizontal mast arm or support truss, increasing the torsional motion of the mast arms; c) the use of large VMSs that implies the presence of a large horizontal surface that increases the effect of truck-induced gusts [5]. It was also identified that the structural connections of all these types of sign supports are susceptible to fatigue loadings, wind induced vibration and crack propagations on the surface or welded connection inside.

While the optimal design of such structures is paramount to preventing damage and consequent collapse, the determination of proper inspection technology is important to prevent collapses such as those shown in Fig. 1.3.

The AASHTO specifications [6] affirm that "a regular maintenance program should be established that includes periodic inspection, maintenance, and repair of structural supports." Despite this, no regulations for the inspection of highway sign structures in the United States exist, and those states that do inspect, do so without any uniform process. Different states use different inspection methods over different time periods to make sure that their sign structures continue to function properly.

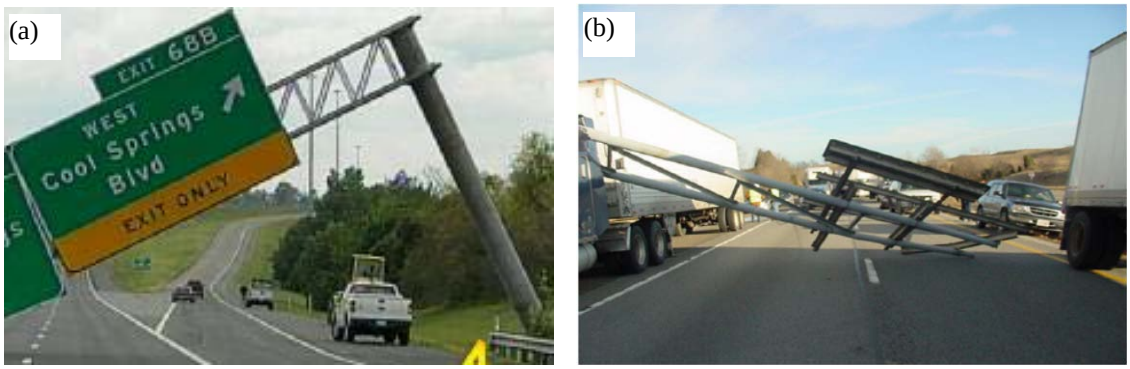

Figure 1.3 - (a) Collapse of a sign structure along I-65 in Tennessee. http://updatewindowssecurity.com/?id=34452915477 (b) Cantilever Sign Structure Failure: (Source: http://www.fhwa.dot.gov/BRIDGE/signinspection03.cfm.

1.2 SCOPE OF WORK

The main objective of this study was the development of a sensing technology to assess the structural soundness of sign supports, cantilever poles, and variable message sign (VMS) supports. The sensing technology is aimed to shift the maintenance paradigm from time-based (periodic inspection) to real-time monitoring.

This work focus on sensing technology coupled to signal processing and feature extraction for the purpose of providing a method to detect damage.

The project included the following research efforts:

a) Apply nondestructive evaluation (NDE) / Structural Health Monitoring (SHM) strategies able to monitor the structure in real-time

b) Use signal-processing algorithms for damage identification and classification.

The aim of the research activities is to develop a robust and low-cost sensing technology to assess the structural soundness of sign structures.

1.3 THESIS OUTLINE

The outline of the report is as follows.

Chapter 2 reports on the background and the technical requirements to use the NDE methods that have emerged from literature review. The methods of visual inspection, liquid penetrant, magnetic particles, and ultrasonic testing are illustrated. This chapter reviews the potential technologies that can be adapted especially from the oil and gas industry. In fact, many support structures are made of tubular components and therefore technologies used in the pipeline industry may be adapted. Attention is also given to the requirement needed to operate a transition

from time-based to condition-based monitoring approach. Several feasible techniques to develop the SHM approach are illustrated.

Chapter 3 presents the hardware, software, and equipment used in the experimental program conducted at the Laboratory for Nondestructive Evaluation and Structural health Monitoring studies and the Watkins-Haggart Structural Engineering Laboratory, both at the University of Pittsburgh. The test protocol and signal processing utilized to process the ultrasonic data are presented as well.

Chapter 4 describes the results obtained from the application of ultrasonic data applied to the three tests performed in the laboratory. The first test consisted of monitoring the onset and growth of an artificial crack under dynamic loading. The second test consisted of monitoring the onset and growth of a second artificial crack under dynamic loading. Finally, during the third test the structure was monitored under different environmental (dry, rainy, snowy) and temperature (cold, warm) conditions. Part of the work presented in this chapter was reported in the journal paper:

> Zhu, X., Rizzo, P., Marzani, A., and Bruck, J. (2010). "Ultrasonic Guided Waves for NDE/SHM of Trusses," Measurement Science and Technology, 21, 045701, doi: 10.1088/0957-0233/21/4/045701.

Chapter 5 illustrates the results obtained from the application of the electromechanical impedance method applied to some of the laboratory tests.

Chapter 6 presents the experimental results of tests conducted in the field. Two structures were monitored.

Chapter 7 concludes the report with some final remarks and recommendations for future studies.

2.0 NONDESTRUCTIVE TESTING METHODS

This chapter reviews the NDT methods that have been proposed or utilized to inspect sign support structures. The methods of visual inspection, magnetic particle, dye penetrant, and ultrasonic testing are discussed. A general outline of the inspection procedures is described. A description of potential transition of two types of maintenance methodology is also given at the last part.

2.1 CURRENT METHODS

2.1.1 Visual inspection

Aided or unaided or remote visual inspection methods (VIMs) are one of the most basic NDT techniques. Generally VIM is the first method utilized to locate suspected defects areas in large structures. Inspectors follow procedures that range from simply looking at a part to see surface imperfections to performing various gauging operations, which assure compliance with acceptable physical standards [7].

Once suspected areas are identified, they can be thoroughly examined using other approaches. In the past the successful result of a visual inspection laid upon the inspectors' skill, surface conditions of the structure under investigation, quality of any aid tools, and proper illumination. The development of sophisticated optical systems such as high-definition cameras,

special probes, spectrometers, and notebook computers has greatly improved the inspection outcomes.

Depending upon the field of application, visual inspection procedure can be tedious, time consuming and characterized by high implementation costs [8]. Sometimes, inspection requires dismantling of the critical components before inspections and reassembling afterwards [9], which could consume up to 45% of the entire inspection time, as in the case of the aviation sector [10].

Tools that inspectors can be used to perform visual inspection and to enhance the ability to remotely view critical area are: borescopes, videoscopes, and crawlers. Borescopes are optical instruments for remote viewing of objects. They have long been used for the inspection of pipe and tubing [7]. Analogue to borescopes, videoscopes reduces many of the deficiencies of traditional borescopes by adding the quality and the advantages of digital imaging.

In the sign supports, visual inspection is normally conducted using a pair of binoculars of at least ten power magnification or a telescope such as a shooter's spotting telescope. The latter offers higher magnification, with the ability to identify smaller cracks. Several efforts have also been made to develop a robotic device that can climb for instance the vertical poles [4].

Although VIM is the primary inspection method, it cannot detect all structural deficiencies. Examples include small fatigue cracks in welds, corrosion occurring on the interior of the structural element, and cracked anchor rods. Future improvement of remotely operated crawlers able to climb structures while carrying a video camera may bring the VIM to a superior level of performance.

2.1.2 Liquid penetrant

Liquid (or dye) penetrant testing (PT) is a rapid, simple, relatively inexpensive NDE method [11]. It can be considered as an extension of visual inspection and it is used for detection of surface-breaking flaws on any non-absorbent material's surface.

In penetrant testing the surface being inspected is cleaned thoroughly to remove all traces of dirt and grease. A bright coloured or fluorescent liquid having very low viscosity is applied to

the component surface and allowed to penetrate any surface-breaking cracks or cavities. After a pre-selected time interval (dwell time), the excess dye is removed from the surface. Another material, called the developer, is placed on the surface. The developer is usually a dry white powder. It draws some of the penetrant from the defects by reverse capillary action to produce indications on the surface, and it provides a contrasting background to make the penetrant easier to see. With fluorescent dyes, an ultraviolet lamp is used to make the "bleed out" fluoresce brightly. These (coloured) indications are broader than the actual flaw and are therefore more easily visible. After the indications from the penetrant/developer have been interpreted and perhaps recorded, the surface is cleaned a third time, to remove the developer and any remaining penetrant. The procedural steps are as shown in Figure 2.1 [11, 12].

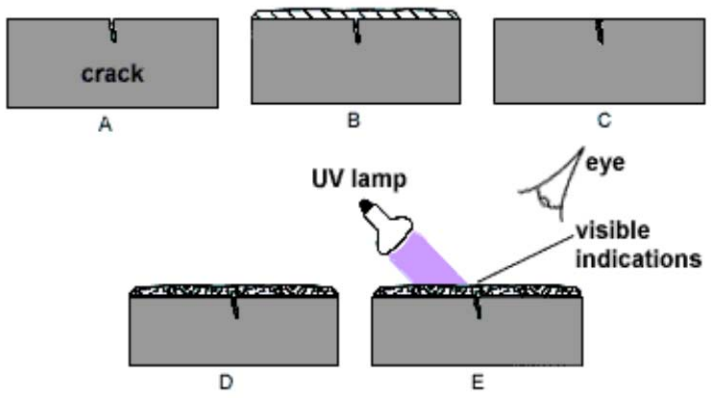

Figure 2.1 - Steps of an inspection conducted by using liquid penetrant testing. (a) Sample before testing; (b) liquid penetrant applied; (c) surplus wiped off leaving penetrant in crack; (d) developer powder applied, dye soaks into powder; (e) View coloured indications, or UV lamp shows up fluorescent indications. (http://www.twi.co.uk/content/ksijm001.html)

A number of different liquid penetrant systems are used. Fluorescent penetrants are normally used when maximum flaw sensitivity is required. However, these penetrants must be viewed under darkened conditions with an ultraviolet (UV) lamp, which may not always be practical. The most commonly used systems are solvent removable, or water washable, red dye systems, which typically comprise three aerosol cans - cleaning fluid, penetrant and developer. The aerospace industry uses fluorescent penetrant to look for fatigue cracking in turbine blades. The construction industry uses dye penetrant to check welds and other susceptible areas prone to

surface-breaking flaws. The drawbacks associated with such technique can be summarized as follows:

1. the test surfaces need to be cleaned adequately, the contact time between the penetrant and the test surface should be sufficiently long, and the excess penetrant must be removed carefully.
2. the inspection cannot be automated.
3. only surface discontinuities are detectable.
4. environmental and safety issues associated with the use of dye penetrant are present.

2.1.3 Magnetic particle inspection

Magnetic particle inspection (MPI) is used to detect surface and near-surface flaws in ferromagnetic materials, to look for cracking at welded joints and in areas identified as being susceptible to environmental cracking (e.g. stress corrosion cracking or hydrogen induced cracking), fatigue cracking or creep cracking. The procedure is relatively simple. A magnetic field is applied to the specimen, either locally or overall, using a permanent magnet, electromagnet, flexible cables. Fine ferromagnetic particles are then applied onto the specimen's surface. If the material is sound, most of the magnetic flux is concentrated below the material's surface and the particles follow the induced magnetic field [11, 12]. However, if a flaw is present, such that it interacts with the magnetic field, the flux is distorted locally and 'leaks' from the surface of the specimen in the region of the flaw. The particles create a visible indication of the flaw. Magnetic particles commonly used are black iron particles and red (Fig. 2.2) or yellow iron oxides. In some cases, the iron particles are coated with a fluorescent material enabling them to be viewed under a UV lamp in darkened conditions.

Magnetic particles are usually applied as a suspension in water or paraffin. This enables the particles to flow over the surface and to migrate to any flaws. On hot surfaces, or where contamination is a concern, dry powders may be used as an alternative to wet inks. On dark surfaces, a thin layer of white paint is usually applied, to increase the contrast between the

background and the black magnetic particles. The most sensitive technique, however, is to use fluorescent particles viewed under UV (black) light.

For the inspection of welded areas either by liquid penetrant or MPI, the American Welding Society (AWS) D1.1 - Structural Welding Code – Steel Inspection should be followed. The code establishes the acceptance criteria for production weld criteria, the standard procedures for performing visual inspection and NDT, and the qualifications and responsibilities of inspectors.

Some of the drawbacks associated with MPI are:

1. the low sensitivity to detect cracks that run parallel to the magnetic field. In this circumstance there is little disturbance to the magnetic field and it is unlikely that the crack is detected. To avoid this limitation it is recommended that the inspection surface is magnetised in two directions at 90° to each other. Alternatively, techniques using swinging or rotating magnetic fields can be used to ensure that all orientations of crack are detectable.
2. the selection of the magnetization method must be pondered. It depends on the geometry of the component and whether or not the whole specimen is to be magnetised. Permanent magnets are attractive for on-site inspection, as they do not need a power supply. However, they tend only to be used to examine relatively small areas and have to be pulled from the test surface. Despite needing their own power supply, electromagnets (yokes) find widespread application. Their main attraction is that they can be used to concentrate the field at the surface where it is needed, they are easy to remove (once the current has been switched off), and the magnetic field strength can be varied. Hand-held electrical prods are useful in confined spaces. However, arc strikes at the prod contact points can damage the specimen surface and, because the particles must be applied when the current is on, the inspection becomes a two-man operation.
3. residual magnetic fields left after the inspection is terminated may interfere with welding repairs. These can be removed by slowly wiping the surface with an energised AC yoke.
4. deeply embedded flaws cannot be detected
5. cannot be used for non-ferromagnetic materials, such as aluminium, copper or austenitic stainless steel.
6. length of the inspection time.

Figure 2.2 - Magnetic particle testing of a welded area.
(Source : http://www.fhwa.dot.gov/BRIDGE/signinspection03.cfm)

2.1.4 Ultrasonic Testing

Ultrasonic testing (UT) is one of the most widely used NDT methods today [11]. UT is based on the propagation of stress waves with frequencies higher than 20 kHz. A stress wave is characterized by its frequency, wavelength, and speed. In unbounded media two types (modes) of waves can propagate: the longitudinal bulk mode also referred to as P-wave (pressure wave), and the shear bulk mode (S-wave or T-wave).

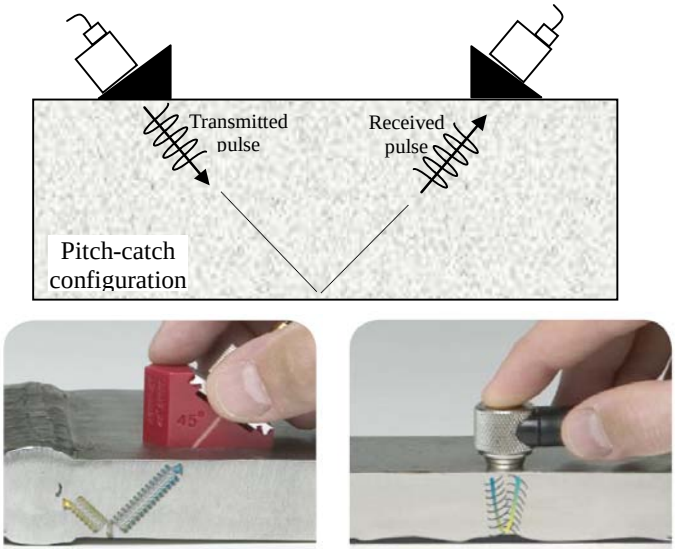

Figure 2.3 - Bulk UT configurations. Top: pitch catch. Top right: pulse echo. Bottom right: pulse/echo with angular wedge (angle beam transduction). Photo source: http://www.olympus-ims.com/data/File/panametrics/panametrics-UT.en.pdf

In the longitudinal mode, the particle displacement is parallel to the direction of wave propagation; conversely, in the shear waves the particle displacement is orthogonal to the propagation direction.

Ultrasonic NDT is known for common applications like thickness gauging, flaw detection, material properties characterization, and acoustic imaging. Changes in one or more of four measurable parameters associated with the passage of a wave through a material—transit time, attenuation, scattering, and frequency content—can often be correlated with changes in the material's physical properties or geometry, and with the presence of damage.

Bulk waves are the most commonly used waves because only two modes can be measured without the complication of the multimode wave propagation typical of the guided waves. Sound pulses are normally generated and received by piezoelectric transducers that are acoustically coupled to the test material. In most cases a single transducer coupled to one side of the test piece serves as both transmitter and receiver (pulse/echo configuration).

A sound wave is launched by exciting the transducer with either a voltage spike or a continuous wave impulse. The sound wave travels through the test material, either reflecting off the far side to return to its point of origin (pulse/echo), or being received by another transducer (pitch-catch) (Fig. 2.3). The received signal is then amplified and analyzed.

Disadvantages of bulk wave-based UT are the low sensitivity to: 1) detect discontinuities oriented parallel to the direction of propagation of the ultrasonic energy; 2) discontinuities that are similar or smaller than the material's grain structure; 3) thin sections for which very high frequencies are necessary.

2.2 POTENTIAL INSPECTION/MONITORING TECHNIQUES

In the last decade academia and industry have devoted an increasing attention toward advanced NDT methods and toward the implementation of inexpensive structural health monitoring (SHM)

solutions. The latter approach evolves the maintenance paradigm from “time-based” to “condition-based”. In “time-based” maintenance the inspection is conducted at predefined times or interval established by federal regulations, state policies, or owners’ guidelines regardless the condition of the components. Condition-based maintenance implies that a sensing system is integrated with the structure to provide real-time stream-like information of the structure’s health.

The trade-off associated with implementing such a philosophy is that it requires a more sophisticated monitoring hardware to be deployed on the system and it requires a sophisticated data analysis procedure that can be used to interrogate the measured data [13].

This section reviews other NDT methods and novel SHM techniques that show promise for implementation for the inspection (NDT approach) or real-time monitoring (SHM approach) of sign support structures. In the context of time-based maintenance the methods of eddy current and X-ray are reviewed. Guided ultrasonic waves (GUWs) and acoustic emission (AE) testing can be used instead either as NDT method or SHM approaches. Finally the SHM approach of the electromechnical impedance (EMI) is described.

2.2.1 Eddy Current

Eddy current testing (ECT) measures a materials response to electromagnetic fields over a specific frequency range, typically a few kHz to MHz [11].

An ECT is based on inducing electrical currents in the material under investigation and observing the interaction between the currents and the material. Eddy currents are generated by electromagnetic coils in the test probe, and monitored simultaneously by measuring the probe electrical impedance.

The basic principles are as follows. A current flowing in a wire generates a magnetic field that encircles the wire. A magnetic field in proximity with the metal surface under inspection (to be monitored) produces a voltage. The ECT measurement consists of 4 steps, namely ‘signal excitation’, ‘material interaction’, ‘signal pickup’, and ‘signal conditioning and display’. One coil (excitation coil) is excited with an AC signal and the other coil (pick-up coil) is connected to

a voltmeter**.** The first coil produces a magnetic field, part of which passes through second coil. The pickup voltage reading will remain constant until the whole set up (first and second coils) is placed near the metal surface (ferromagnetic material). The disturbance to magnetic field is measured in the form of voltage at second coil. This is because the first coil when placed near any ferromagnetic material induces current in the material, which travels in closed circular paths, known as eddy currents [11].

ECT is suitable to assess material conditions such as hardness and thickness or to detect the presence of corrosion or defects such as porosity and cracks. The method is adopted in automotive and aircraft manufacturing processes and it is an integral part of inspection and maintenance in the power generation and aircraft industries [11].

ECT has the advantages of being versatile, sensitive, contact between the probe and the surface is not required, the surface does not need to be specifically prepared (unlike for liquid penetrant, magnetic particle). However such method is limited to the inspection of conductors and it is sensitive to a wide range of parameters, which can represent a drawback. Other limitations include shallow-depth of penetration, lift-off effects, surface conditions, and sensitivity only to cracks perpendicular to the interrogating surface.

In the sign support industry the technique of eddy currents can be applied leveraging the experience of research outcomes in the area of crack detection in aircraft skins [14], stainless steel piping [15], structural steel [16], and welds [17].

2.2.2 X-ray

Radiographic techniques and specifically X-rays is one of the few NDT methods that can examine the interior of an object and the only NDT method that works on all materials [11]. An X-ray (or Röntgen ray) is a form of electromagnetic radiation with a wavelength in the range of 0.01 to 1 nanometers, corresponding to frequencies in the range $3x10^{17} – 3\ x10^{19}$ Hertz.

X-rays have high electromagnetic energy. These rays tend to pass through object that block visible light. The amount of X-rays that pass through a material is dependent on the elemental

composition, density, and thickness of the material, and the energy and amount of X-rays [11]. This method can detect cracks, flaws, and thickness reduction.

X-ray based NDT has the advantages of being accurate, inherently pictorial, adaptable to examine shapes and sizes, sensitive to the discontinuity that causes a reasonable reduction of cross-section thickness. However this method carries the burden of safety hazard concerns. It can be time-consuming and expensive. It also requires extensive experience and trained personnel to safely carry out the inspection and to properly interpret the images.

As radiographic methods were proposed to inspect corrosion in pipes [18] and more in general pipeline structures, the use of X-ray technology can be extended to monitor tubular components and welded areas in sign support structures.

2.2.3 Guided ultrasonic waves

When ultrasound propagates into a bounded media, a guided ultrasonic wave (GUW) is generated. The wave is termed “guided” because it travels along the medium guided by the medium’s geometric boundaries. Different types of guided waves exist: Rayleigh waves, Lamb waves, cylindrical waves. Rayleigh waves are waves propagating along the surface of an semi-infinite space. In plate-like structures Lamb waves propagate. They occur in two different basic modes, the symmetrical or dilatational mode, and the asymmetrical or bending mode. In a slender, isotropic, traction-free cylindrical waveguide three types of vibration modes can exist: longitudinal, flexural and torsional waves. The first two waves are analogous to symmetric and anti-symmetric Lamb waves, respectively.

The application of guided waves is more complicated than bulk waves because guided waves are multimode (many vibrating modes can propagate simultaneously) and dispersive (the propagation velocity and the attenuation depend on the wave frequency).

Methods based on GUWs gained popularity owing to the capability of inspecting moderately large areas using a single probe attached or embedded in the structure while maintaining high sensitivity to small flaws. GUWs can travel relatively large distances with little attenuation and offer the advantage of exploiting one or more of the phenomena associated with transmission,

reflection, scattering, mode-conversion and absorption of acoustic energy that have shapes. As sign support structures contain several hollow cylindrical components (mast, vertical poles, truss members) and these components may be welded, the use of GUWs is feasible and offers the same advantages offered by any general GUWs application.

2.2.4 Acoustic Emission

AE is a passive method that monitors the transient stress waves generated by the rapid release of energy from localized sources within a material. Elastic energy propagates as a stress wave in the structure and is detected as AE event by one or more sensors attached to or embedded in the structure (Fig. 2.4). Such events can be linked to the onset of new damage or to the growth and propagation of existing anomalies. AE differs from most other NDT techniques in two key respects. First, the signal has its origin in the material itself, not in an external source. Second, AE detects movement, while most other methods detect existing geometrical discontinuities. Different AE sources may produce different AE waveforms. The AE source mechanism results in different received signals if the source is oriented differently with respect to the geometry of the medium or the propagation path to the detector.

AE is suitable for global monitoring, real-time evaluation, and remote sensing. By using an array of AE sensors, a global region or volume of material can be monitored and damage onset and propagation can be detected. Other advantages are associated with the ability to discriminate among different sources of events, i.e. sources of damage. Finally in AE monitoring, time consuming and expensive point by point scanning is not required. As any method related to the propagation of stress waves, AE may suffer from attenuation and be subjected to extraneous noise. It is a contact method, i.e. it requires contact between the sensing technology and the structure under investigation. Not always the previous loading history of the structure can be determined. To determine the location of the AE event multiple sensors are required. There are countless applications of AE in the civil infrastructure industry. The feasibility of using to monitor pole connections in signal structures was carried out by Wang [19] in a laboratory setting.

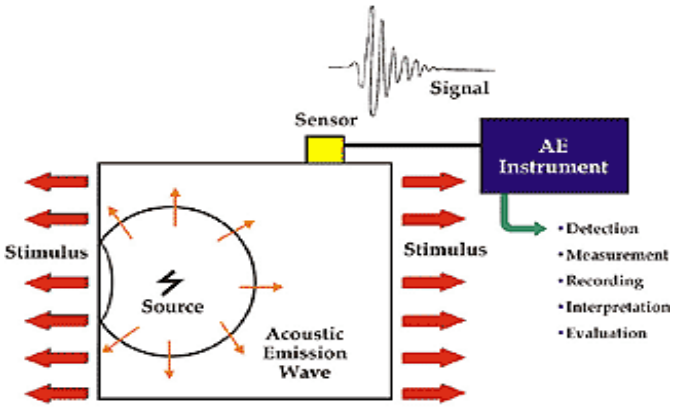

Figure 2.4 - AE principles. Source: http://www.pacndt.com/index.aspx?go=research

2.2.5 Electromechanical Impedance

The electromechanical impedance (EMI) method measures the resistance of a structure to vibrations. A damaged/cracked structure offers different resistance to vibration as compared to undamaged structure. Liang et al. [20] presented the first application of EMI on a one dimensional skeletal structure for NDE applications.

Figure 2.5 - PZT bonded on aluminum and steel beams.

In the last decade EMI applications spanned from small sized laboratory structures to real sized aerospace structures. In this technique piezoceramic or piezoelectric transducers are employed as source of vibration. These patches are surface bonded on the host structure to be monitored (Fig. 2.5). The governing principle is that an harmonic electric field excites the PZT transducer to produce a structural response which is known as ‘admittance signature’. The signature is a function of the stiffness, mass and damping of the host structure being monitored [21], and the

length, width, thickness and orientation of the patch [22]. The changes in the admittance signature, which is the inverse measure of the structure's mechanical impedance, are indicative of the presence of damage.

The EMI technique was employed for various prototypes line pipelines, aerospace and civil structures. However, as this method is relatively novel, its applications to real world structures are still rare.

In academia, methods based on EMI were proposed to monitor spot welded structural joints [23], fatigue cracks [24, 25] and bolted connections of pipeline systems [26].

2.3 SUMMARY AND CONCLUSIONS

This chapter reviewed the main NDT methods used in industry for different usages. The principles and the advantages/disadvantages of eddy current testing, guided ultrasonic waves approach and EMI were discussed. The first method is potentially feasible to inspect surface and near-surface defects. The method of guided ultrasonic wave can be used either for damage detection inspection or for damage detection monitoring of any tubular component. Finally the EMI-based method is suitable for monitoring approach of parts like bolts and tubular components.

3.0 LABORATORY TESTS

3.1 THE STRUCTURE

One real-size sign support structure was tested at the University of Pittsburgh. The structure was part of a variable message sign support structure located over I-80 Eastbound, one mile West of the junction with I-81 in Pennsylvania, USA in Penn DOT District 4-0. The truss information was specified in Appendix A. A photo of the structure in service is shown in Fig. 3.1 while its location is illustrated in Fig. 3.1 (b).

In May of 2006, a routine field inspection found two large cracks in two of the upper chords of this four chord galvanized steel truss. Cracks positions on truss are presented in Fig. 3.2. The structure was removed from service as a preventative measure. An investigation into the cause of the observed cracking a forensic investigation was conducted [27]. As a result, selected joints were requested by Robert J. Connor and Associates LLC for examination. Both cracked and uncracked joints were sent to the Bowen Laboratory of Purdue University in West Lafayette, IN for destructive examination.

The laboratory examination identified an additional crack in one of the connections. The results of the study suggest that the cracking was present when the structure was erected and no evidence of fatigue crack growth was observed on the crack surface. The cracking is believed to be the result of Liquid Metal Embitterment (LME), a phenomenon resulting in brittle fracture of usually ductile steel in the presence of liquid metal. The fractures likely initiated in the Zinc bath during the galvanizing process, but remained undetected until the field inspection. Upon finding the additional crack and suspecting LME was the cause of the cracks, Dr. Connor suggested that Penn DOT perform more in depth inspection on all similar structures in the inventory (i.e., those galvanized steel truss structures carrying VMS structures of the same vintage) using dye penetrant and ultrasonic inspection. Since the third crack was not found during the original

inspection, there was concern that other cracks may be present in other structures. The center to center bearing span of the original truss was 17.4 m (58.5 ft), with the bearings located on the vertical support columns. A bolted field splice was located mid-span of the truss. The chord is made from ASTM A-53 steel.

One of the two trusses connected with bolts in the original structure was delivered at the University of Pittsburgh. Photos of the delivery are presented in Fig. 3.3.

The 3-dimensional rendering of the truss and the dimensions is presented in Fig. 3.4 (a). The structure was accommodated at the Watkins-Haggart Structural Engineering Laboratory (Figs. 3.4 (b) and (c). The dimensions of the truss are reported in Fig. 3.4 (c) and (d).

(a)

(b)

Figure 3.1 – (a) Photo of the sign support structure when in service; (b) Original location

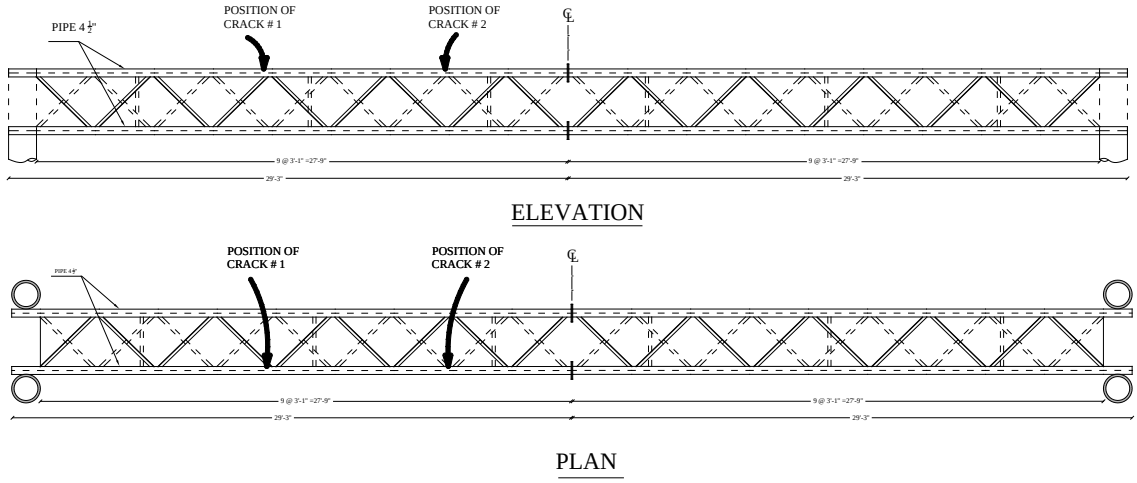

Figure 3.2 – Location of cracks found during the investigation conducted in [27].

Figure 3.3 - Photo of the delivery at the University of Pittsburgh.

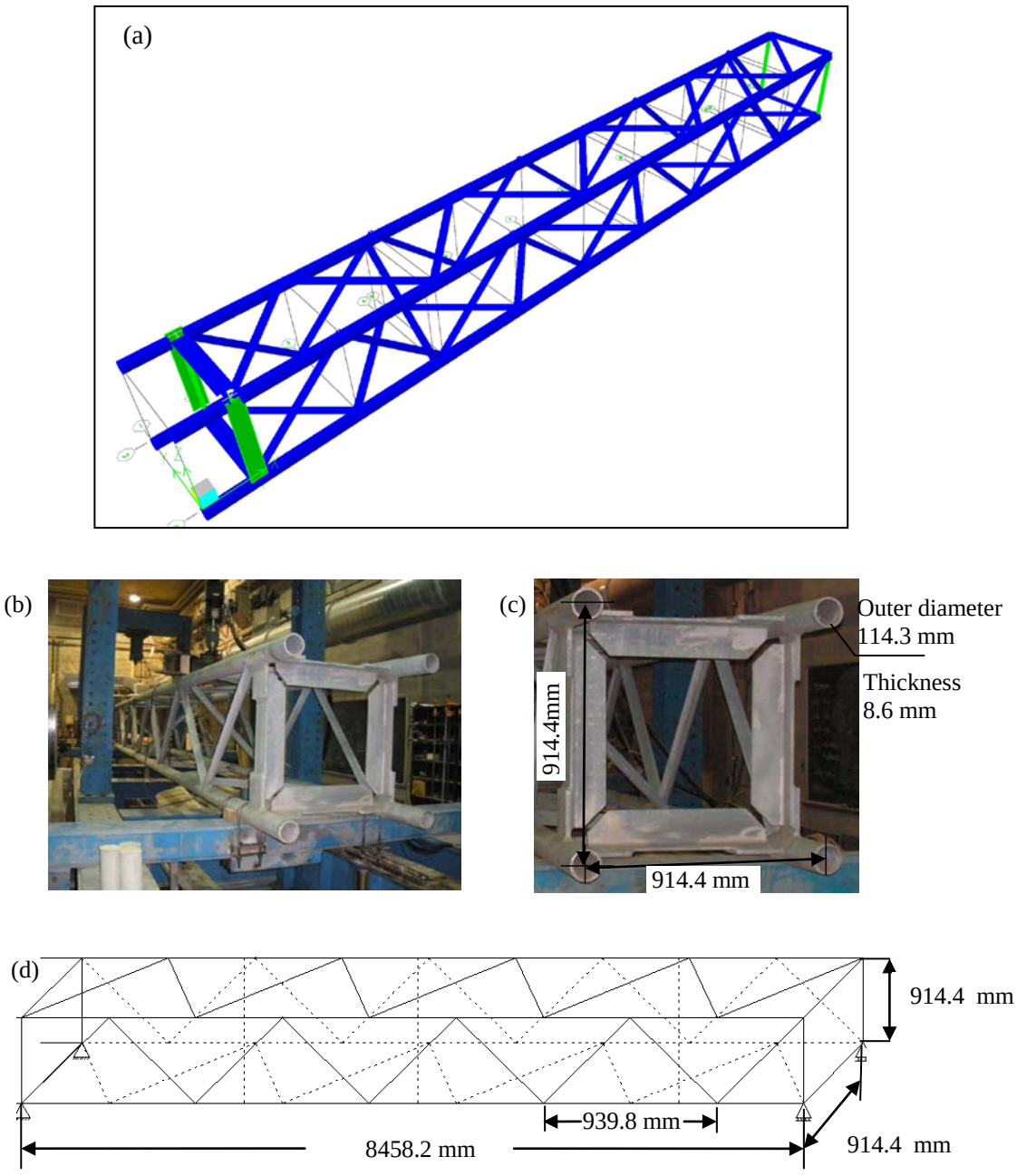

Figure 3.4 - (a) 3-D rendering of the truss. (b-c) Photo of truss set onto the supports (d) Sketch and dimensions. The standard sections for individual members were listed in Appendix A

3.2 HARDWARE – SOFTWARE – SETUP

In this section the hardware and the software utilized in this study is described. The experimental setup is illustrated in the second part of the chapter.

3.2.1 The sensors

PKI-502-Navy type II PZT transducers (Model# PKI P/N SP0.330-0.330-0.120-502) from Piezo-Kinetics (http://www.piezo-kinetics.com) were employed in this study. The dimensions of the transducers were 0.33 in × 0.33in × 0.12in. The applied field voltage output of these transducers can be in through thickness or horizontal shear as shown in Fig. 3.5.

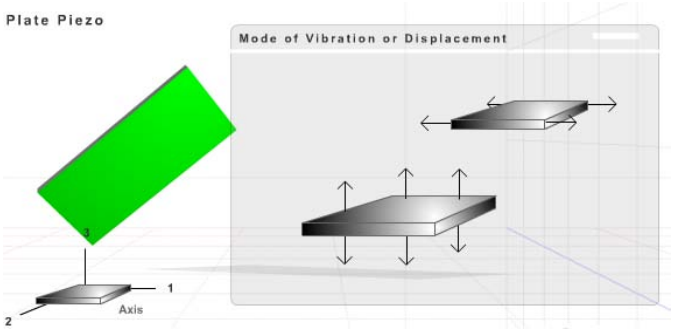

Figure 3.5 - Mode of vibration of the PZTs used in this study.
Source: http://www.piezo-kinetics.com/21_plate_movie.htm

3.2.2 The Data Acquisition System

A National Instruments PXI unit running under LabView, integrated with a reed relay matrix switch module PXI 2530, and combined with TB 2643 and SCB 264X as terminal block, was employed for signal generation, detection, and acquisition.

For the guided waves excitation, a 5-cycle, 10 V peak-to-peak sinusoidal toneburst, modulated with a Gaussian window was used. The detected signals were amplified 20 times by a linear amplifier, sampled at 10 MHz, averaged 10 times to increase the signal-to-noise ratio, and stored for post-processing analysis. A LabView program was designed to operate the switch so that every PZT could act as a transmitter or as a receiver. For instance, it will be seen that in Test 1 and Test 2, eleven transducers were used. For convenience these transducers were named S0, S1,…, S10. The switch module and the software was coded such that when PZT S0 was transmitting the toneburst, S1-S10 acted as sensors. Then PZT S1 was switched into an actuator and PZTs S0, S2-S10 acted as receivers. The operation was repeated for every PZT. The program was designed such that the operator can select the number of cycles and voltage amplitude. In addition the program provides the flexibility to select the center frequency of the toneburst and to execute a frequency sweep between a lower and an upper limit selected by the operator.

To apply the EMI measurement, an electric circuit was designed and a second Labview program was created. The PXI acted as a function generator directing a 1 Volt, 50-cycles sinusoidal wave in the frequency range 50 - 500 KHz with frequency step equal to 0.5 KHz. More detail of the circuitry and the mode of employment of the PXI to conduct the EMI measurements are provided in Chapter 5.

Photos of the hardware setup and of the software designed for both the UGW and the EMI studies are presented in Fig. 3.6. The front panel developed for the UGW measurement is presented in Fig. 3.6 (b). The Function Generator Parameter tab shown in this figure has the controls to select the following toneburst parameters: window function; initial, final, and step of the desired frequency sweep; amplitude; repetition rate; number of tonebursts per desired frequency. The front panel developed for the EMI measurement is presented in Fig. 3.6 (c). Some of the controls available in the panel are: initial, final, and step of the desired frequency sweep; type of wave being generated; number of cycles.

(a)

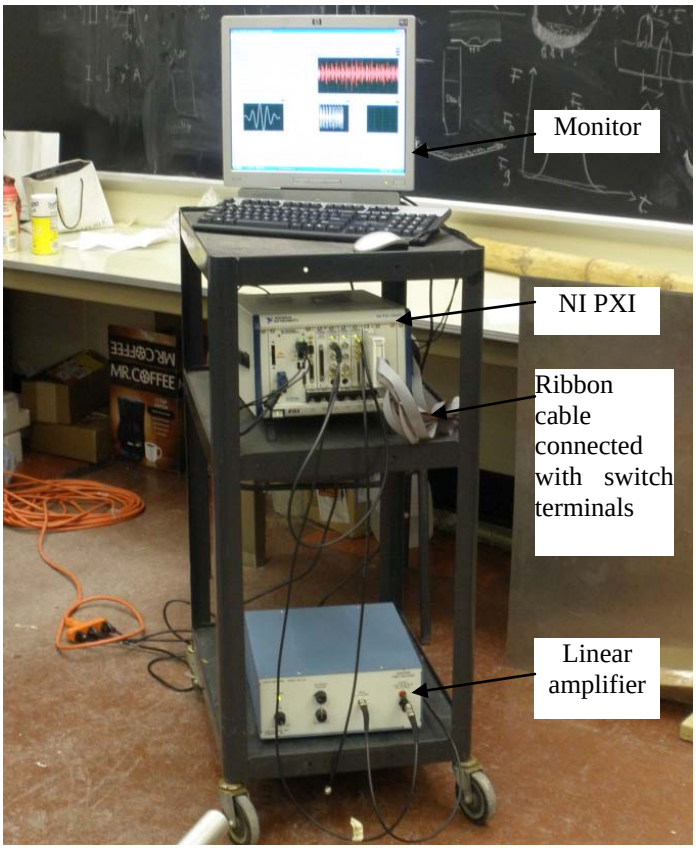

Figure 3.6 - (a) Hardware setup for the UWG. (b) LabView program front panel created to control the UGW measurements. (c) LabView program front panel created to conduct the EMI-based experiments

(b)

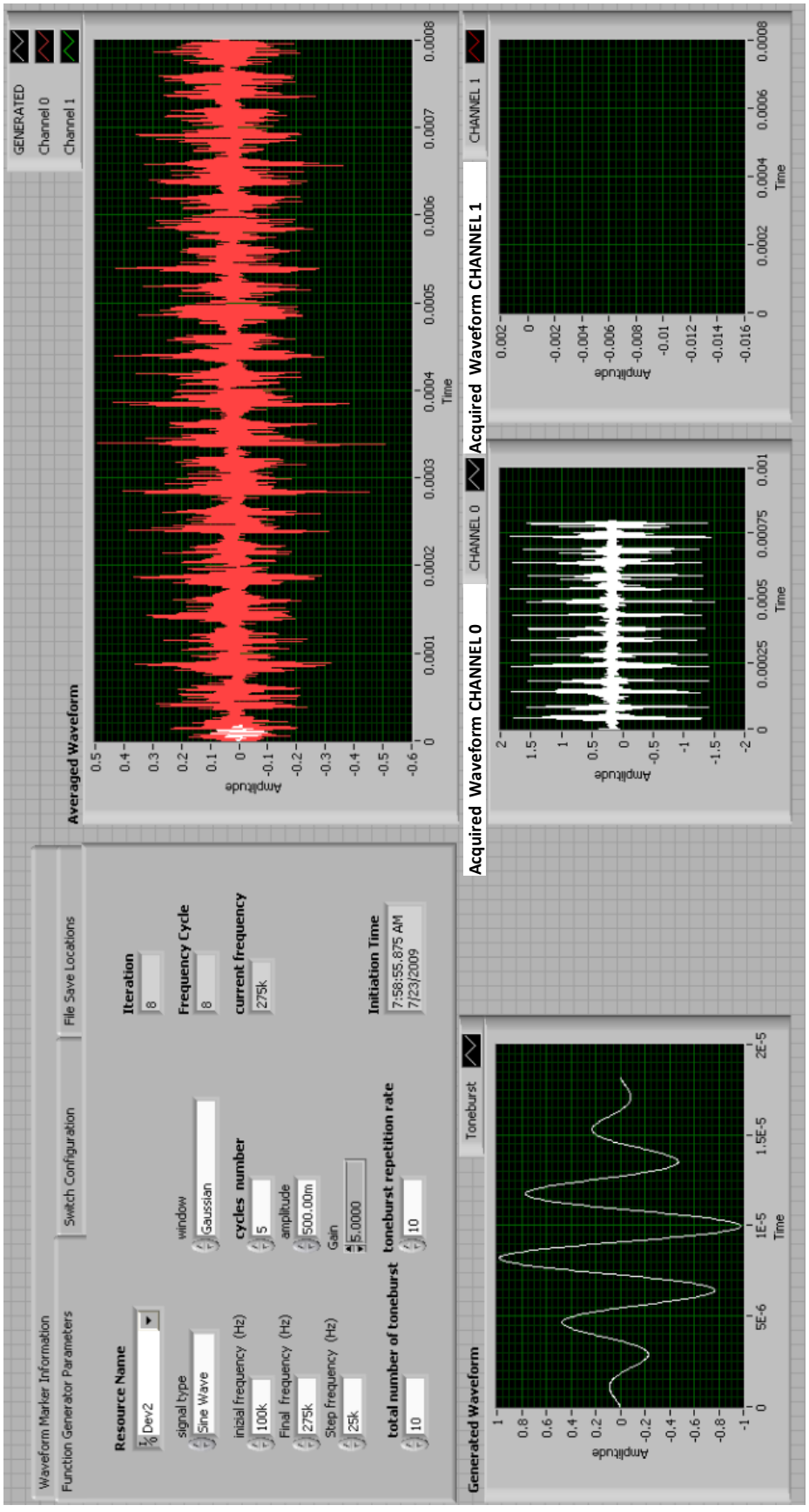
Waveform Marker Information
Function Generator Parameters
Switch Configuration
File Save Locations
Resource Name
Dev2
signal type
Sine Wave
window
Gaussian
Iteration
8
Frequency Cycle
8
inizial frequency (Hz)
100k
Final frequency (Hz)
275k
Step frequency (Hz)
25k
cycles number
5
amplitude
500.00m
Gain
5.0000
current frequency
275k
total number of toneburst
10
toneburst repetition rate
10
Initiation Time
7:58:55.875 AM
7/23/2009
Generated Waveform
Toneburst
Amplitude
Time
Averaged Waveform
GENERATED
Channel 0
Channel 1
Acquired Waveform CHANNEL 0
CHANNEL 0
Acquired Waveform CHANNEL 1
CHANNEL 1

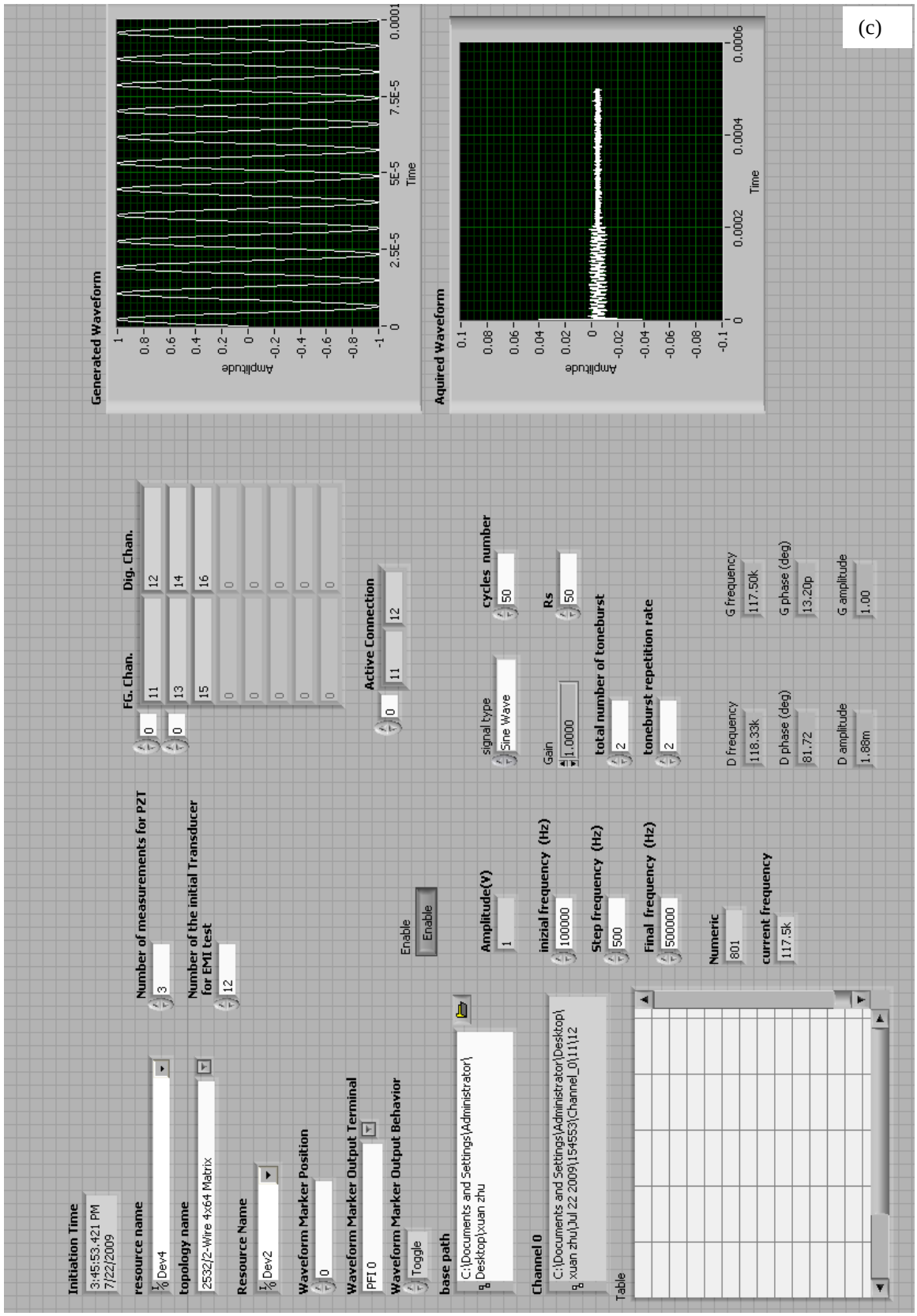
Initiation Time
3:45:53.421 PM
7/22/2009
resource name
Dev4
topology name
2532/2-Wire 4x64 Matrix
Resource Name
Dev2
Waveform Marker Position
0
Waveform Marker Output Terminal
PFI 0
Waveform Marker Output Behavior
Toggle
base path
C:\Documents and Settings\Administrator\Desktop\xuan zhu
Channel 0
C:\Documents and Settings\Administrator\Desktop\xuan zhu\Jul 22 2009\154553\Channel_0\11\12
Table
Number of measurements for PZT
3
Number of the initial Transducer for EMI test
12
Enable
Enable
Amplitude(V)
1
inizial frequency (Hz)
100000
Step frequency (Hz)
500
Final frequency (Hz)
500000
Numeric
801
current frequency
117.5k
FG. Chan.
Dig. Chan.
Active Connection
signal type
Sine Wave
Gain
1.0000
cycles number
50
Rs
50
total number of toneburst
2
toneburst repetition rate
2
D frequency
118.33k
D phase (deg)
81.72
D amplitude
1.88m
G frequency
117.50k
G phase (deg)
13.20p
G amplitude
1.00
Generated Waveform
Amplitude
Time
Aquired Waveform
Amplitude
Time

(c)

3.2.3 Test Protocol 1

For Tests 1 and 2, eleven through-thickness PZTs were used for the generation and detection of UGW. The relative position of these eleven transducers on the truss is shown in Fig. 3.7 (a) and (b), respectively. For convenience they are sequentially identified as S0, S1, …, S10. For illustrative purposes a close up view of PZT S5 and S1 is presented in Figs. 3.7 (c) and (d), respectively. The dimensions were plotted in Fig. 3.4 (d).

Three PZTs were used for the EMI method. The relative position of these three transducers, named EM1 EM2 and EM3, on the truss is shown in Fig. 3.8.

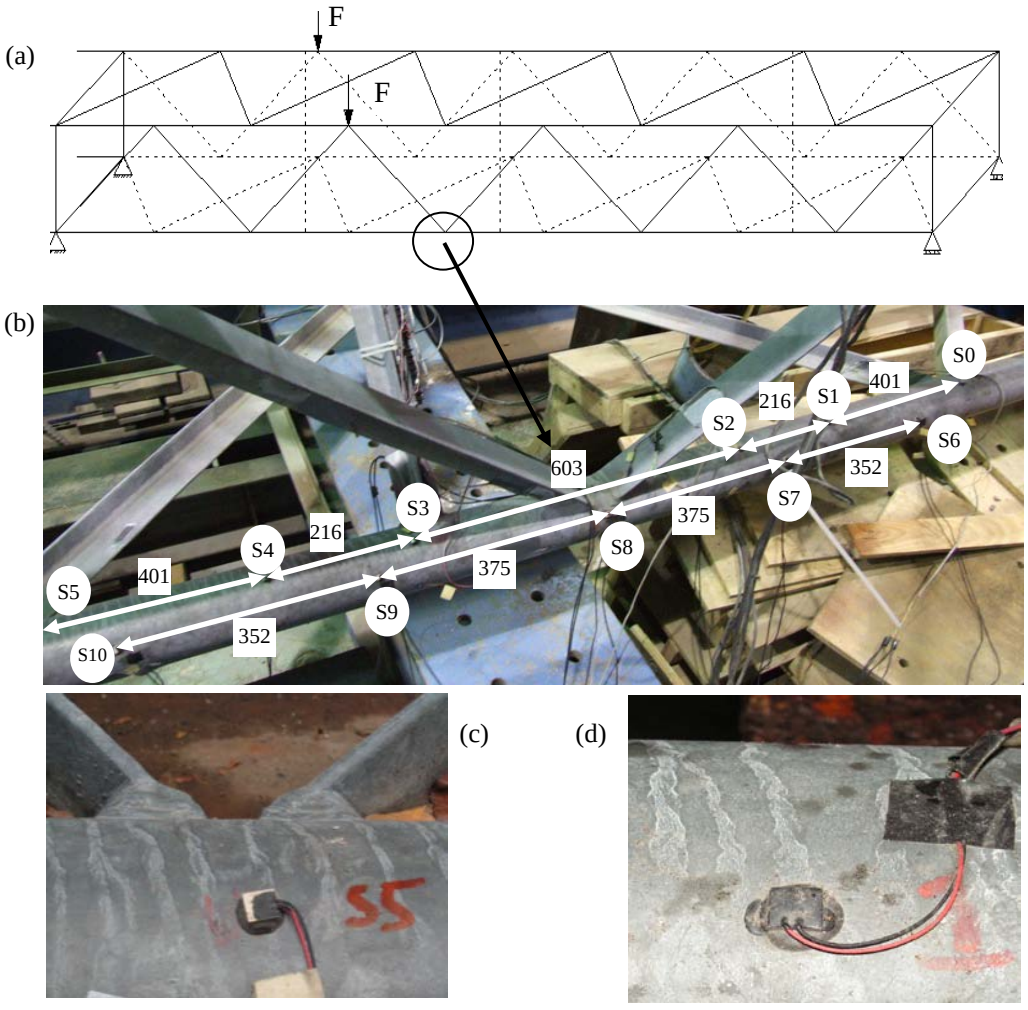

Figure 3.7 - (a) Sketch of the truss structure. (b) Location and relative distance of PZTs S0,…,S10. (c) Close up view of PZT S5. (d) Close up view of PZT S1. Dimensions are expressed in mm.

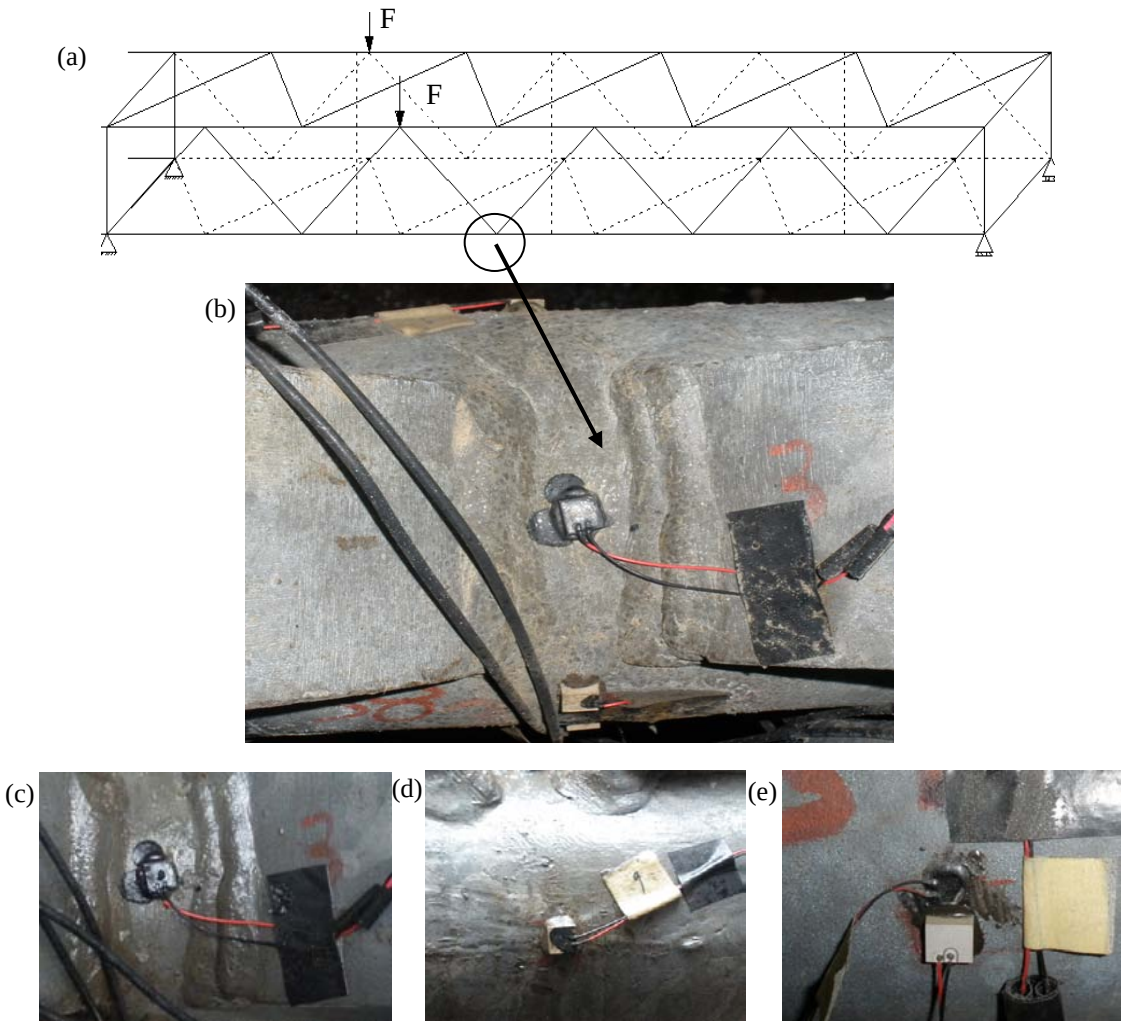

Figure 3.8 - (a) Sketch of the truss structure. (b) View from the top of the joint under investigation and PZT EM1. (c-e) Close up view pf for EM1 located between two joints (d) close up view for EM2 located inner side of the chord (e) close up view for EM3 located outer side of the chord.

To investigate the capability of UGWs and EMI to detect crack initiation and growth, two artificial notches were machined and progressively increased in size. The first one was devised near the weld toe at the joint illustrated in Fig 3.7 (a). The position and orientation of the notch are shown in Fig. 3.9 (a). The structure was subjected to 1 Hz sinusoidal cyclic load to simulate steady-state vibrations, induced by wind or traffic-induced gusts. The loading setup, shown in Fig. 3.9 (b), consisted of a 1290 mm-long steel beam that distributed over two joints the force

generated by a hydraulic actuator. The load was cycled from 8.9 kN to 125 kN, resulting in a load range of 116 kN. During the first 25,000 load cycles, the notch size was artificially increased using a Dremel MultiPro Machine. The load history of the crack, i.e. the crack size as a function of the number of cycles, is presented in Fig. 3.9 (c). The area of the crack is approximately the length of the notch along the surface multiplied by the depth. Following every few thousand cycles the cyclic loading was paused and a static load of 66.7 kN was applied. Under this constant load, the size of the crack was measured and ultrasonic and EMI-related data from the PZTs were collected.

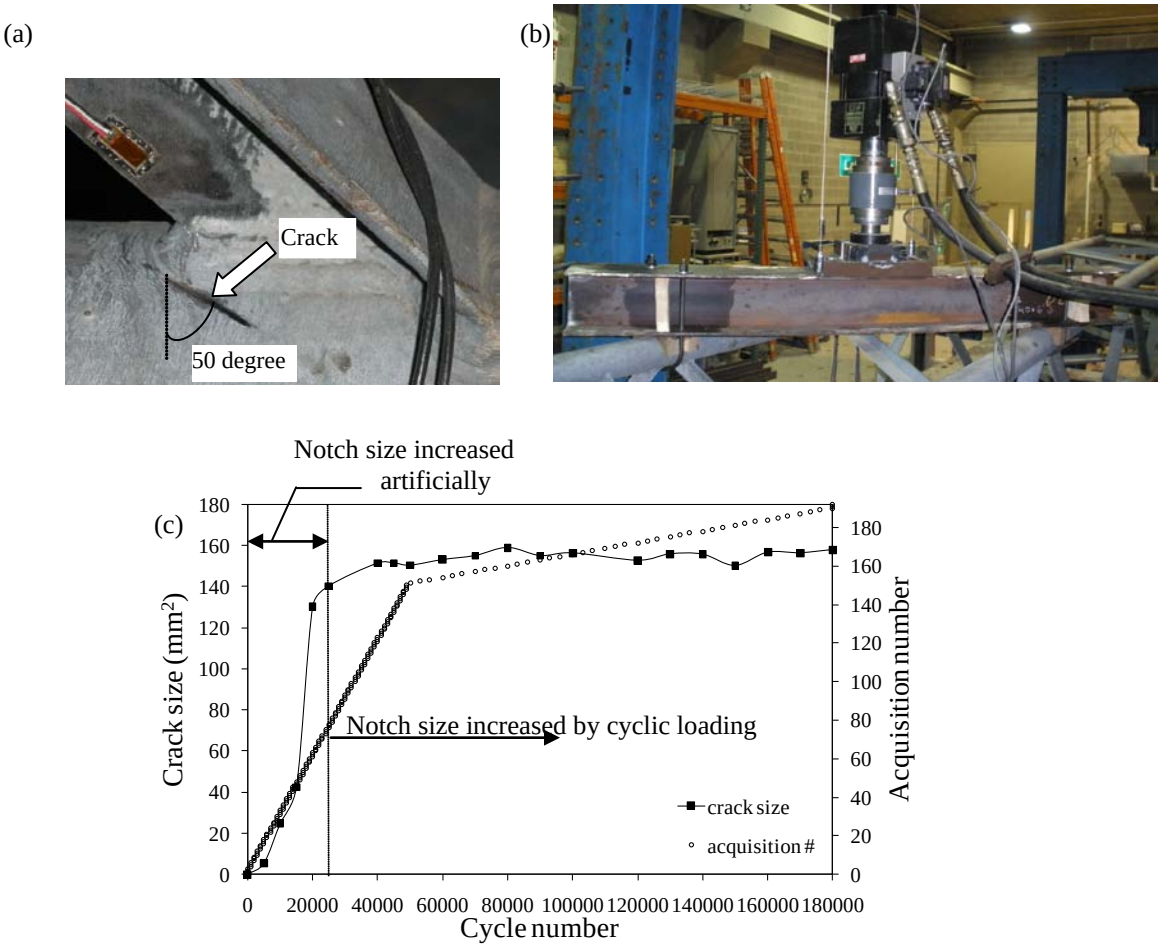

Figure 3.9 - (a) Close-up view of the artificial notch machined along the weld between the chord and one angular diagonal member. (b) Loading setup (c) Crack size and acquisition number as a function of cycle loading number.

The square dots in Fig. 3.9 (c) indicate the moment at which the crack size was measured. Measurements were also taken during the active cyclic loading. A total of 192 acquisitions were

taken. The acquisition number (1-192) as a function of the number of load cycles is superimposed in Fig. 3.9 (c).

It should be observed that the loading after 40,000 cycles had a limited effect on the crack growth. The modest scatter of the crack area value above 50,000 cycles is likely related to the variability of the manual measurement.

3.2.4 Test Protocol 2

A second crack was devised near the weld toe of the second diagonal member concurring in the same joint as illustrated in Fig 3.10 (a). Similarly to Test 1, the crack was progressively machined and its position and orientation are shown in Fig. 3.10 (b). The same loading setup visible in Fig. 3.9 (b) was adopted to apply a 1 Hz sinusoidal load ranging from 8.9 kN to 151.2 kN.

The load history of the crack, i.e. the crack size as a function of the number of cycles, is presented in Fig. 3.10 (c). As Test 2 followed Test 1, the cycle number count associated to Test 2 is considered starting at cycle 180,001. During the first 150,000 load cycles (cycles' range 180,001-330,000) the notch size was artificially increased. Following every 5,000 cycles the dynamic loading was paused and a static load of 80 kN was applied. Under this constant load, the size of the crack was measured and data from the PZTs were collected. The square dots in Fig. 3.10 (c) indicate the moment at which the crack size was measured. Measurements were also taken during the active cyclic loading. A total of 124 acquisitions were taken. The acquisition number (193-316) as a function of the number of load cycles is superimposed in Fig. 3.10 (c). The modest scatter of the crack area value above 330,000 cycles is likely related to the variability of the manual measurement.

For both tests, the size of the notch was estimated by inserting a small piece of paper inside the notch and penciling the contour along the external surface of the chord. It was assumed that the internal part of the paper was adherent to the internal portion of the crack.

Then the area under the penciled contour was measured. It is acknowledged that this approach might have some degree of inaccuracy.

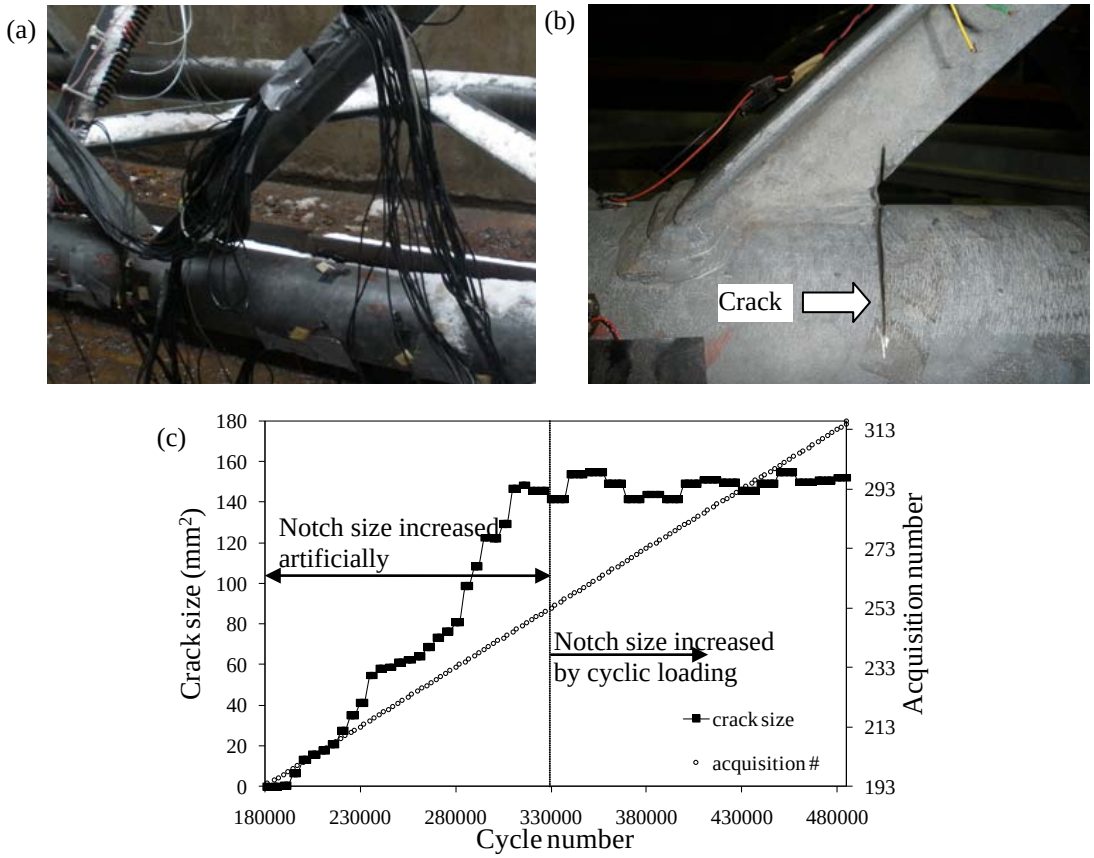

Figure 3.10 - (a) Close-up view of the joint where artificial notch was machined (b) the artificial notch along the weld between the chord and one angular diagonal member. (c) Crack size and acquisition number as a function of cycle loading number.

3.2.5 Test Protocol 3: Environmental Test

In practical SHM applications, environmental factors such as temperature, humidity, electromagnetic inference may affect the performance of the damage detection algorithm. Any temperature variation, for instance, slightly changes the geometric and mechanical properties of the structure. If sensors are used, the properties of the sensors and of the adhesive utilized to bond them to the structure may also change due to temperature or moisture. If the sensors are made by piezoelectric crystals, the piezoelectric coefficients and the dielectric permittivity terms are both temperature-sensitive. Finally the presence of snow or rain change the boundary

conditions around the structure and this may change the physical characteristic of the nondestructive method being used.

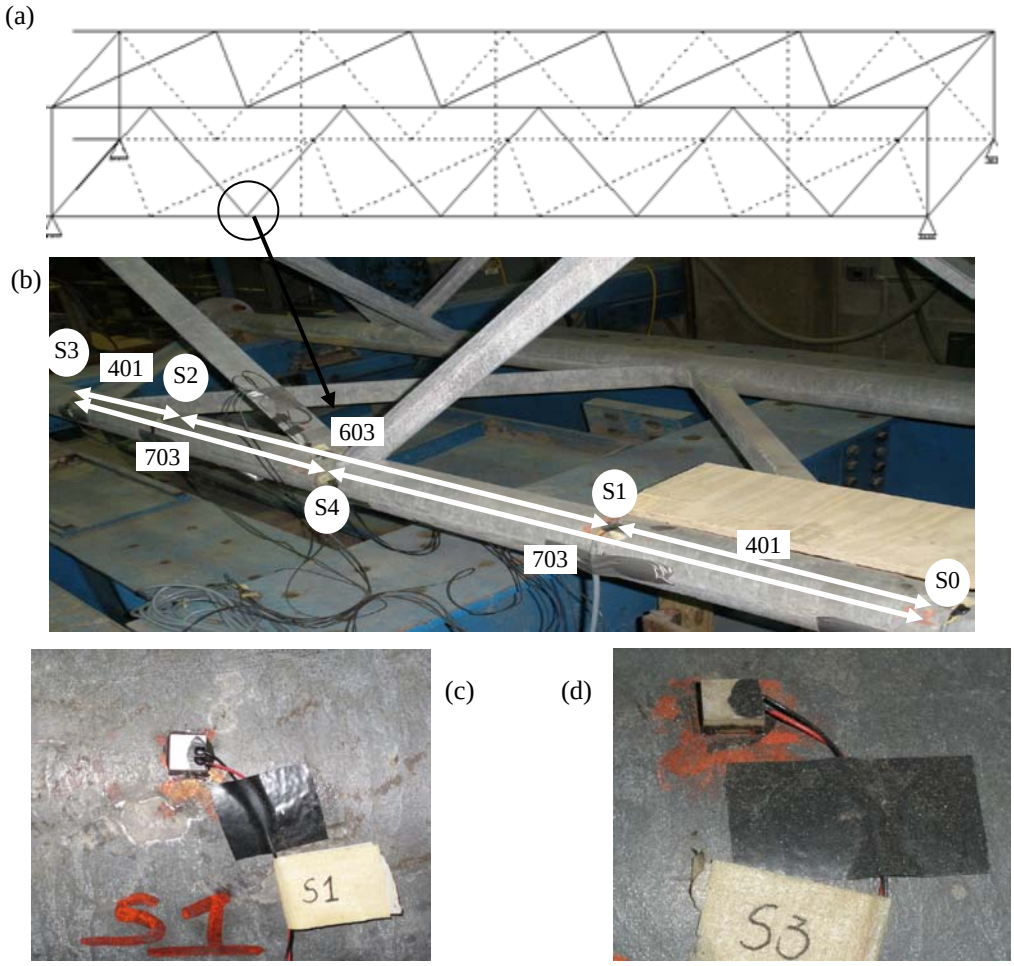

Figure 3.11 - (a) Sketch of the truss structure. (b) Location and relative distance of PZTs S0,…,S4. (c) Close up view of PZT S1. (d) Close up view of PZT S3. Dimensions are expressed in mm.

If the propagation of guided waves is being used for SHM purposes, all the factors mentioned above may contribute to the variation of wave velocity and wave distortion. Thus, any variation of the wave energy characteristics due to environmental factors might overshadow any effect associated with the presence of damage, or conversely may produce the presence of false positives.

To assess the role that environmental conditions play on the SHM of the truss structure being investigated a third experiment was conducted at the Pitt's WHSEL. With the same aim, a field

test was executed and will be discussed on Chapter 6. The welded joint under observation is circled in Fig. 3.11 (a). It must be remarked that in this third test, the horizontal chord under investigation was the one opposite to chord monitored in Tests 1 and 2. Therefore the joint under investigation was close to the splice that served to connect this truss to the truss studied in [27].

Five PZTs in shear displacement were used for the generation and detection of UGW. The relative position of these five transducers on the truss is shown in Fig. 3.11 (b). The transducers were named as S0, S1…S4. For illustrative purposes a close up view of PZT S5 and S1 is presented in Figs. 3.11 (c) and (d), respectively.

The sixth PZT was attached in between the diagonal members converging into the joint and serve to evaluate the effect of temperature and boundary conditions on the EMI measurement. The relative position of transducer, named EM1, on the truss is shown in Fig. 3.12. Unfortunately, this PZT was malfunctioned after few measurements and its role will not be discussed in this report.

(a)

.

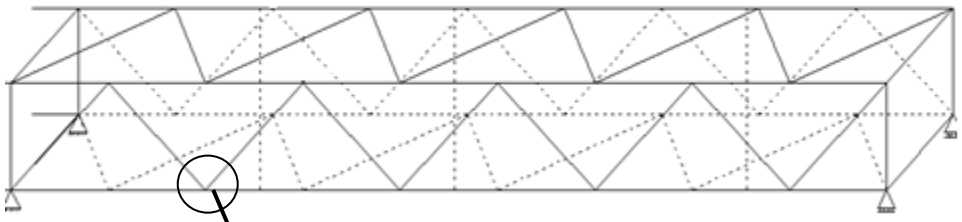

(b)

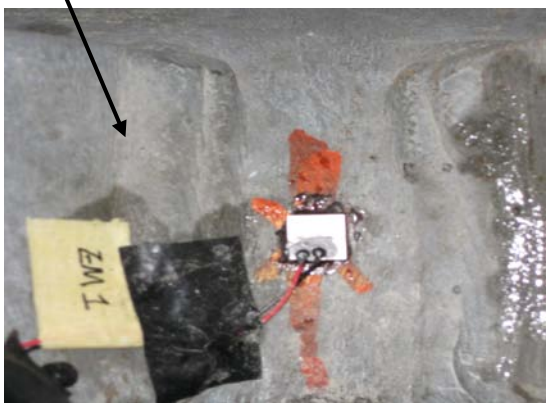

Figure 3.12 - (a) Sketch of the truss structure. (b) View from the top of the joint under investigation and PZT EM1.

In this third experiment, three control variables were considered: temperature, boundary condition and damage. Eighty-five measurements were taken under different combination of these parameters.

As the experiment was conducted during winter, the temperature was controlled by bringing the truss inside the laboratory or leaving it outside in the lab's pit. During internal measurement, the temperature was controlled by regulating the heating system. The temperature was measured attaching a portable thermocouple to the structure.

Figure 3.13 - (a) Close-up view of the artificial notch machined along the weld between the chord and one angular diagonal member. (b) Close-up view of enlarged crack. (c) Snowing condition

The boundary condition was varied by exposing the truss to snow or rain precipitation. When left inside, the structure was tested under dry conditions or under melting snow that was brought from the outside. To raise the temperature of the material a heat gun was used and the best efforts were made to make the chord's temperature along the wave paths as uniform as possible.

Finally the truss was monitored under three different structural conditions: pristine, crack, and enlarged crack. The latter is about twice as the first damage. The defect was devised near the weld toe at the joint illustrated in Fig. 3.12 (a) and 3.13 (a). As shown in Fig. 3.14 (a) and (b), the crack consisted of a notch oriented perpendicular to the orientation of the chord. The photo in Fig. 3.14 (c) shows, instead, the measurement conducted while the structure was exposed to snow.

The experimental setup configuration is presented in Table 3.1.

Table 3.1 - Experimental setup configuration for Test 3.

Measurement #	Temp C	Boundary	Inside/outside	Damage
1	17.7	dry	i	pristine
2	17.7	dry	i	pristine
3	17.7	dry	i	pristine
4	17.7	dry	i	pristine
5	17.7	dry	i	pristine
6	17.7	dry	i	pristine
7	17.7	dry	i	pristine
8	17.7	dry	i	pristine
9	17.7	dry	i	pristine
10	17.7	dry	i	pristine
11	6.7	melting snow	i	pristine
12	6.7	melting snow	i	pristine
13	6.7	melting snow	i	pristine
14	6.7	melting snow	i	pristine
15	6.7	melting snow	i	pristine
16	6.7	melting snow	i	pristine
17	6.7	melting snow	i	pristine
18	6.7	melting snow	i	pristine
19	6.7	melting snow	i	pristine
20	6.7	melting snow	i	pristine
21	8.2	dry	i	pristine

Table 3.1 (continued)

22	8.2	dry	i	pristine
23	2	dry	o	pristine
24	2	dry	o	pristine
25	2	dry	o	pristine
26	2	dry	o	pristine
27	2	dry	o	pristine
28	2.7	dry	o	pristine
29	2.7	dry	o	pristine
30	2.7	dry	o	pristine
31	2.7	dry	o	pristine
32	2.7	dry	o	pristine
33	0.2	snow	o	pristine
34	0.2	snow	o	pristine
35	0.2	snow	o	pristine
36	0.2	snow	o	pristine
37	0.2	snow	o	pristine
38	0.2	snow	o	pristine
39	0.2	snow	o	pristine
40	0.2	snow	o	pristine
41	0.2	snow	o	pristine
42	0.2	snow	o	pristine
43	-2	snow	o	pristine
44	-2	snow	o	pristine
45	-2	snow	o	pristine
46	-2	snow	o	pristine
47	-2	snow	o	pristine
48	6.5	dry	i	pristine
49	6.5	dry	i	pristine
50	22	dry	i	pristine
51	22	dry	i	pristine
52	17.2	dry	i	damage 1
53	17.2	dry	i	damage 1
54	22	dry	i	damage 1
55	22	dry	i	damage 1
56	3	melting snow	i	damage 1
57	3	melting snow	i	damage 1
58	3	melting snow	i	damage 1
59	3	melting snow	i	damage 1
60	3	melting snow	i	damage 1
61	3	dry	i	damage 1

Table 3.1 (continued)

62	3	dry	i	damage 1
63	3	dry	i	damage 1
64	3	dry	i	damage 1
65	3	dry	i	damage 1
66	3	dry	i	damage 2
67	3	dry	i	damage 2
68	3	dry	i	damage 2
69	3	dry	i	damage 2
70	3	dry	i	damage 2
71	0.3	melting snow	i	damage 2
72	0.3	melting snow	i	damage 2
73	0.3	melting snow	i	damage 2
74	0.3	melting snow	i	damage 2
75	0.3	melting snow	i	damage 2
76	10	dry	i	damage 2
77	10	dry	i	damage 2
78	10	dry	i	damage 2
79	10	dry	i	damage 2
80	10	dry	i	damage 2
81	22	dry	i	damage 2
82	22	dry	i	damage 2
83	22	dry	i	damage 2
84	22	dry	i	damage 2
85	22	dry	i	damage 2

3.3 DIGITAL SIGNAL PROCESSING

3.3.1 UGW-related Signal Processing Algorithm

The overall SHM algorithm implemented in this study for the UGW study is illustrated in the flowchart in Fig. 3.11. Among all the actuator-sensor pairs activated by the NI-switch, only a selected number of waveform paths were examined and presented in this report. For each of the selected paths, all the time waveforms acquired during the tests were analyzed.

Typical time waveforms recorded at the baseline, i.e. in pristine conditions, are shown in Fig. 3.12. The plots are relative to pairs S5=>S4, S5=>S8, S5=>S0, S9=>S6, S0=>S4, S1=>S4, S9=>S0, S9=>S1, S5=>S6, S6=>S5, S6=>S4, S6=>S9, S9=>S8, S6=>S7, S0=>S5, and S0=>S1, where the first number identifies the PZT acting as actuator and the second number indicates the PZT acting as sensor. The presence of several guided waves modes is visible. Many of these modes are flexural modes. Other wave packets are likely originated by mode conversion, generated from the interaction of the guided waves with the truss' angular members at the joints.

It is worth noting that although PZT 5 and PZT 0 were almost 2 m apart, the signal to noise ratio of the time waveform in Fig. 3.14 (c) was still high. This demonstrates that the method is promising to gauge long distance along the chord of the truss by means of a pair of transducers only.

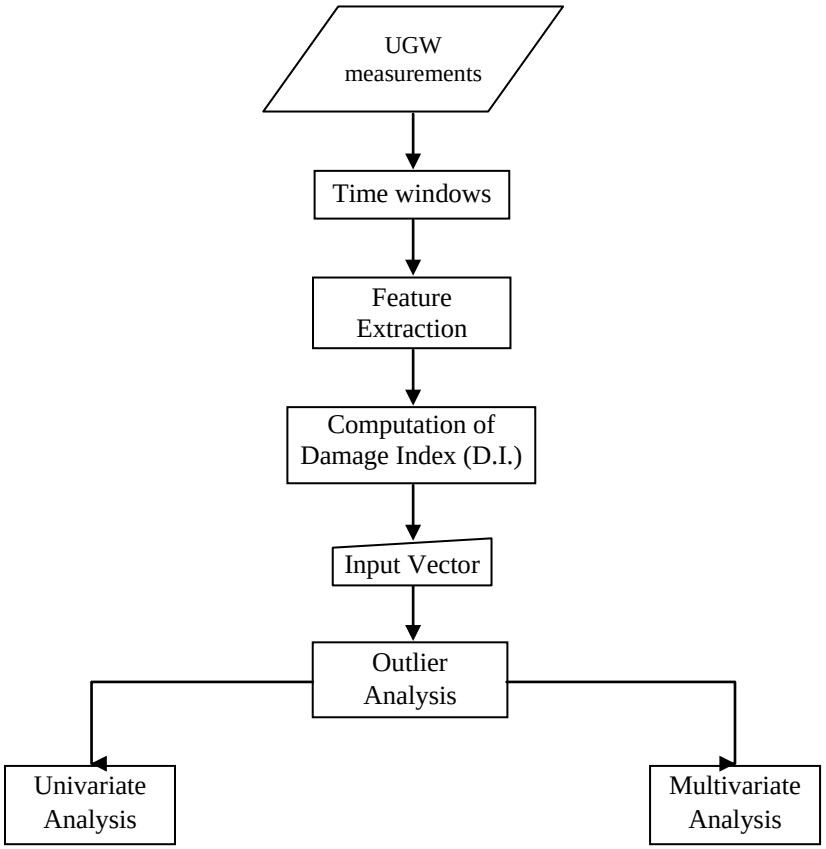

Figure 3.14 - Flowchart of the defect detection procedure.

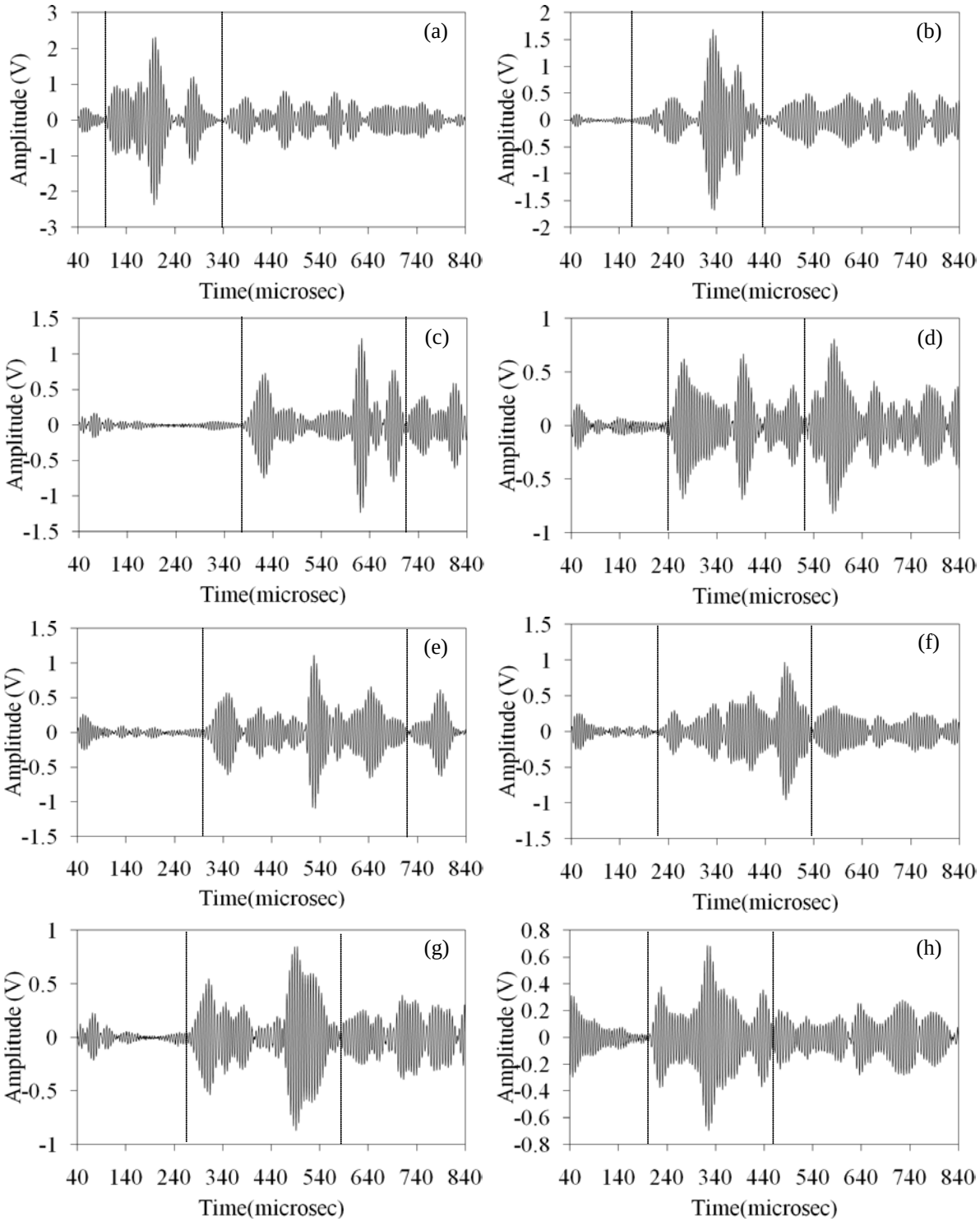
(a)
(b)
(c)
(d)
(e)
(f)
(g)
(h)
Amplitude (V)
Time(microsec)
40 140 240 340 440 540 640 740 840

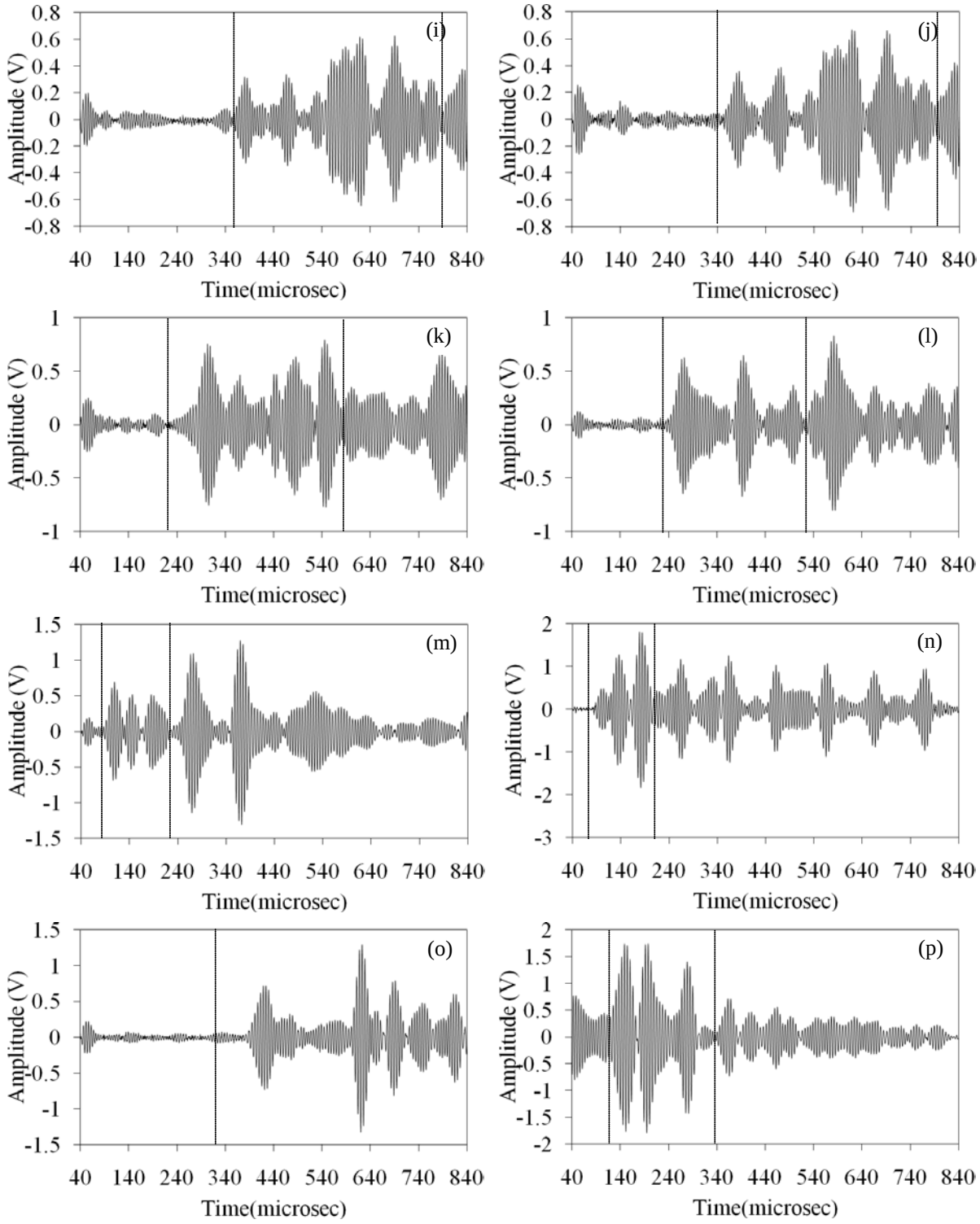

Figure 3.15 - Time waveforms recorded at the beginning of the experimental program from actuator-sensor pairs: (a) S5=>S4 (b) S5=>S8 (c) S5=>S0 (d) S9=>S6 (e) S0=>S4 (f) S1=>S4 (g) S9=>S0 (h) S9=>S1 (i) S5=>S6 (j) S6=>S5 (k) S6=>S4 (l) S6=>S9 (m)S9=>S8 (n) S6=>S7 (o) S0=>S5 (p) S0=>S1.

The first step of the damage detection algorithm was to retain the portion of the signal containing the three (or four) fastest modes, corresponding to the first three (or four) packets observed in each detected baseline waveform. The vertical dotted lines shown in Fig. 3.15 delimit the window applied to the time waveforms associated with the illustrated sensing paths.

Statistical features F_i were then extracted from the time-windowed waveforms. A feature is basically some set of values derived or calculated from measured data. Here maximum (max.) amplitude, peak-to-peak (ppk) amplitude, variance (var), root mean square (rms), kurtosis (krt), crest factor (cf), and k-factor (kf) were selected. Fig. 3.16 shows the rms and the ppk as a function of the number of loading cycles extracted from the retained time series associated with the actuator-sensor pairs discussed in Fig. 3.15. At a given actuator-sensor pair the rms and the ppk appear to be slightly different. As expected, different paths provide different results. Guided waves along path S5 =>S4 should not have been affected by the presence of the notch. This is confirmed by observing that values of the rms and ppk (Fig. 3.16 (a) and (b), respectively) are dispersed within 1.5%.

The statistical features shown in Fig. 3.16 (c) and (d), associated with path S5 =>S8, denote a strong dependency on the number of cyclic loadings, and therefore on the size of the damage. This result is expected, given that sensor S8 is few centimeters from the notch. The values of the ppk (Fig. 3.16 (d)) appear to be less dispersed. Overall, both statistical values at the most severe conditions are 25% less than the corresponding values at the pristine condition. The features associated with pair S5=>S0 (Fig. 3.15 (e) and (f)) have about 5% dispersion and they seem to slightly increase as the damage progressed. Because the sensing path is along two welded joints, wave scattering and leakage into the diagonal members is expected. The geometry along path S5=>S0 is complex, so any result associated with the features needs to be further investigated. Finally, the rms and the ppk associated with waveforms related to pair S9 =>S6 (Figs. 3.15 (g) and (f)) provide two opposite trends, with statistical values dispersed between 11%-13%.

It should be noted, when observing Fig. 3.15, that overall no significant difference exists between data obtained from static loading and dynamic loading. This demonstrates that low-frequency vibration does not affect the propagation of guided waves and their ability to probe small cracks.

Table 3.2 - Damage Index in the form of Waveform path in the D.I. numerator/ Waveform path in the D.I. denominator

Damage Index Number	Waveform path in the D.I. numerator/ Waveform path in the D.I. denominator
1	S5=>S2/S5=>S4
2	S5=>S1/S5=>S4
3	S5=>S0/S5=>S4
4	S0=>S4/S0=>S1
5	S0=>S5/S0=>S1
6	S0=>S4 / S0=>S2
7	S0=>S5 / S0=>S2
8	S6=>S8 / S6=>S7
9	S6=>S9 / S6=>S7
10	S9=>S7 / S9=>S8
11	S9=>S6 / S9=>S8
12	S5=>S8 / S5=>S4
13	S5=>S7 / S5=>S4
14	S5=>S6 / S5=>S4
15	S0=>S8 / S0=>S1
16	S0=>S9 / S0=>S1
17	S0=>S8 / S0=>S2
18	S0=>S9 / S0=>S2
19	S6=>S4 / S6=>S7
20	S6=>S5 / S6=>S7
21	S9=>S0 / S9=>S8
22	S9=>S1 / S9=>S8
23	S9=>S2 / S9=>S8
24	S1=>S4 / S1=>S2
25	S1=>S5 / S1=>S2
26	S9=>S0 / S9=>S8

The next step of the algorithm was to compute a Damage Index (D.I.) as the ratio between a certain statistical feature $F_{a=>b}$ and the same feature $F_{c=>d}$:

$$D.I._{ab/cd} = \frac{F_{a \Rightarrow b}}{F_{c \Rightarrow d}} \tag{3.1}$$

, where the generic subscript (a, b, c, and or d) indentifies one of the eleven PZTs.

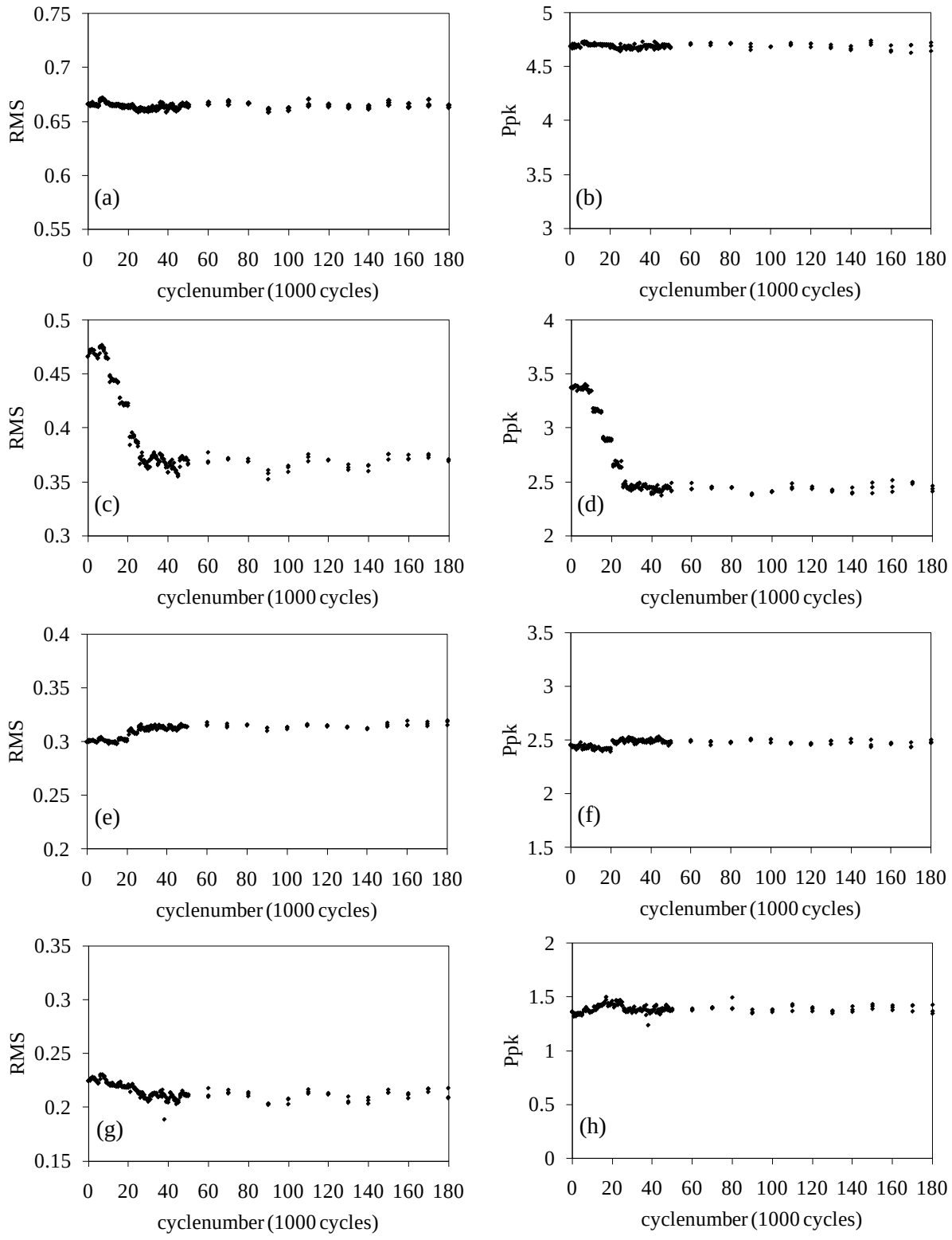

Figure 3.16 - Statistical features as a function of the loading number of cycles. (a) RMS S5=>S4 (b)Ppk S5=>S4 (c) RMS S5=>S8 (d) Ppk S5=>S8 (e) RMS S5=>S0 (f) Ppk S5=>S0 (g) RMS S9=>S6 (h) Ppk S9=>S6.

In this study the twenty-six D.I.s listed in Table 3.2 were considered. The statistical features Fi were the same as discussed above, but normalized with respect to the value found at zero loading cycle.

The D.I.s were then used to feed an unsupervised learning algorithm, based on the outlier analysis. An outlier is a datum that appears inconsistent with the baseline, i.e. a set of data that describes the normal condition of the structure under investigation. Ideally, the baseline should include typical variations in environmental or operative conditions (e.g. temperature, humidity, and loads) of the structure. In the analysis of one-dimensional elements, the detection of outliers is a straightforward process based on the determination of the discordancy between the one-dimensional datum and the baseline. Here the discordancy test based on the deviation statistics:

$$z_\zeta = \frac{\left| x_\zeta - \bar{x} \right|}{\sigma} \tag{3.2}$$

, where x_ζ is the potential outlier, and $\bar{x}$ and σ are the mean and the standard deviation of the baseline, respectively. The mean and standard deviation can be calculated with or without the potential outlier depending on whether “inclusive” or “exclusive” measures are preferred.

For p-dimensional (multivariate) elements, the discordancy test equivalent to Eq. (3.2) is expressed by the Mahalanobis Squared Distance (MSD), D_ζ, which is a non-negative scalar defined as:

$$D_\zeta = (\{x_\zeta\} - \{\bar{x}\})^T \cdot [K]^{-1} \cdot (\{x_\zeta\} - \{\bar{x}\}) \tag{3.3}$$

, where $\{x_\zeta\}$ is the potential outlier vector, $\{\bar{x}\}$ is the mean vector of the baseline, [K] is the covariance matrix of the baseline, and T symbolizes the transpose operation. Both vectors $\{x_\zeta\}$ and $\{\bar{x}\}$ are p-dimensional, whereas [K] is a square matrix of the order p.

As in the univariate case, the baseline mean vector and covariance matrix can be “inclusive” or “exclusive”. In the present study, because the potential outliers are always known a priori, both z_ζ and D_ζ are calculated “exclusively” without contaminating the statistics of the baseline data.

A new datum is an outlier if the corresponding value of z_ζ or D_ζ falls above a set threshold. In the present study, the baseline was computed from the first 18 time histories that, according to

Fig. 3.9 (c), were collected within the first 5,000 cycles. Once the values of the baseline distribution were determined, the threshold value was taken as the usual value of 3σ equal to 99.73% of the Gaussian confidence limit.

3.3.2 EMI-related Signal Processing Algorithm

The overall SHM algorithm applied to the EMI measurements is discussed in Chapter 5.

4.0 EXPERIMENTAL RESULTS FROM UGWS

This chapter describes the experimental results obtained from the measurement of the propagation of the guided waves. The chapter is divided in two sections. The first part describes the analysis of the UGW associated with the propagation of stress waves at 175 kHz. The remaining part of the chapter is devoted to the illustration of the data associated with the propagation of frequencies ranging from 125 kHz to 275 kHz.

4.1 TEST 1

4.1.1 Univariate Analysis

This section presents the outlier analysis result when the statistical features F_i were considered separately and the propagation of the wave at 175 kHz was exploited. Fig. 4.1 shows the discordancy as a function of the crack area for some of the features and wave paths considered in this study. In particular, the damage indexes $D.I._{58/54}$, $D.I._{96/98}$, $D.I._{50/54}$, $D.I._{56/54}$, $D.I._{51/54}$, $D.I._{04/02}$, $D.I._{05/01}$, $D.I._{04/01}$, and $D.I._{91/98}$ associated with the ppk and the rms are presented. The values of the respective thresholds are superimposed and illustrated by means of a horizontal line. It is evident that the rms and the ppk perform differently at a given wave path. For a small notch, a large number of inliers, i.e. false negative indications are visible. As discussed before, at a given damage size, measurements were taken under dynamic or static loads. Nonetheless, the dispersion of the damage index at a given crack extension is small.

The values of the discordancy show that only certain wave paths, both in terms of orientation and direction, are affected by the presence of damage. For instance, by comparing Fig. 4.1 (i)-

(o), it is evident that when the actuator is on the same side of the notch (with respect to the truss joint), the wave is more affected. In fact, the wave path S5=>S1 is symmetric to the path S0=>S4. However, as the notch is closer to the actuator S5 the first path is more affected by the presence of damage than the second path. This evidence suggests that the algorithm not only is effective to detect the presence of anomalies and estimate its severity, but it may represent a valuable mean to localize the position of the damage itself. In addition by observing the plots on the left side of Fig. 4.1 and comparing the corresponding values on the right side of Fig. 4.1 it is evident that the selection of the appropriate feature can be pivotal to enhance the sensitivity of the probing system.

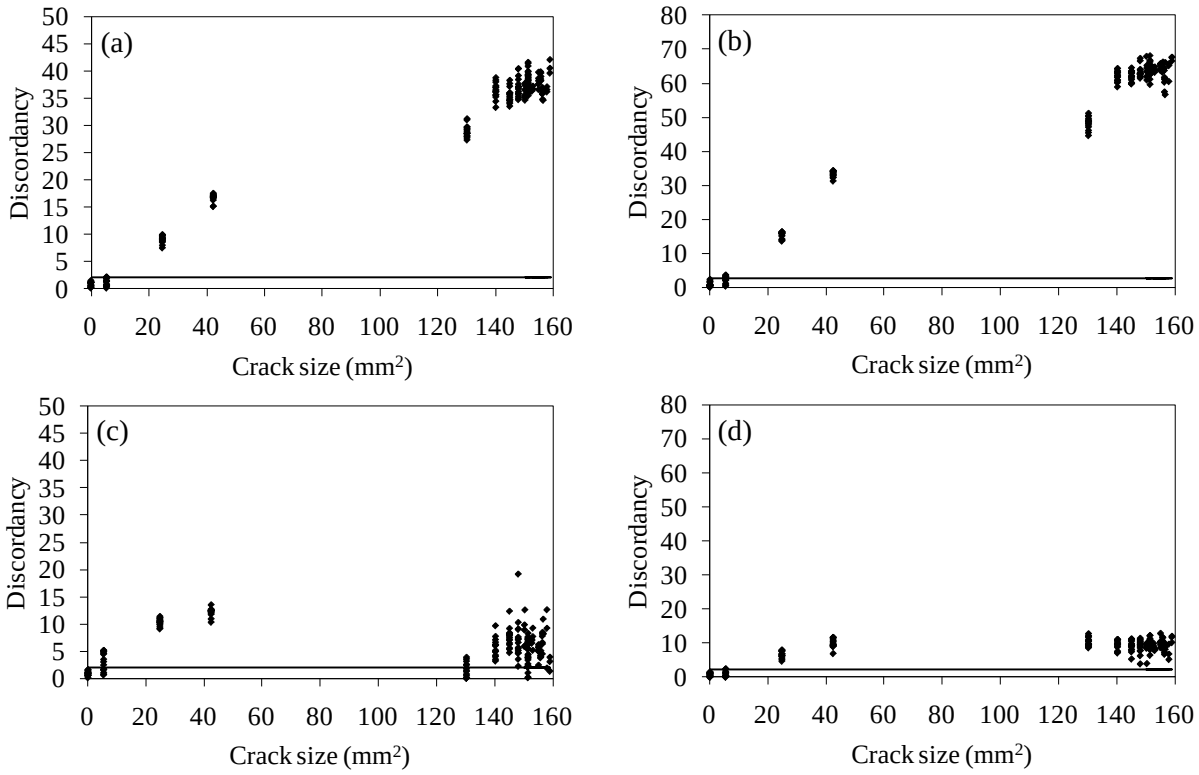

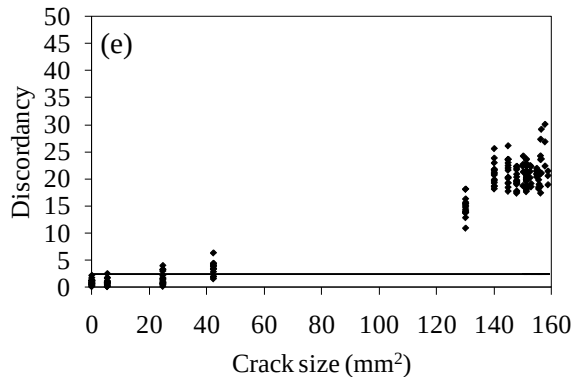
(e)
Discordancy
Crack size (mm²)

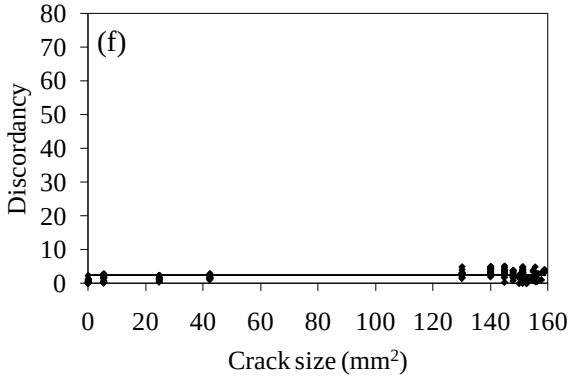
(f)
Discordancy
Crack size (mm²)

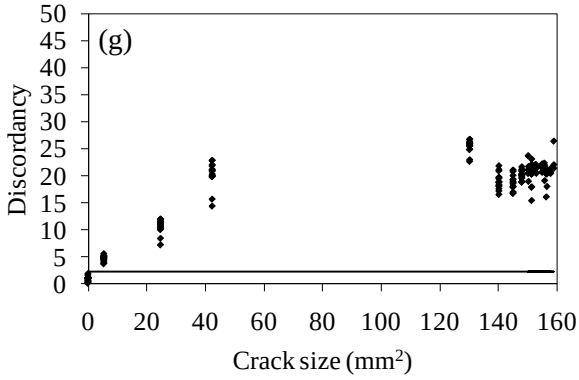
(g)
Discordancy
Crack size (mm²)

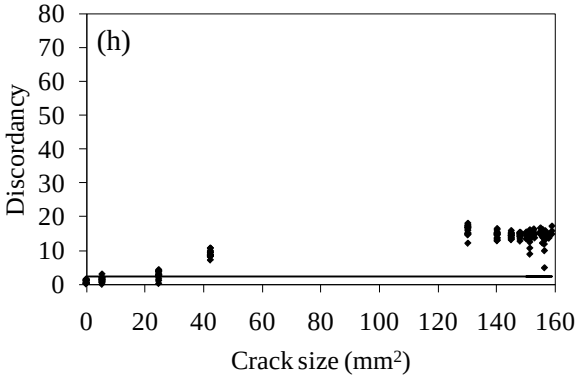
(h)
Discordancy
Crack size (mm²)

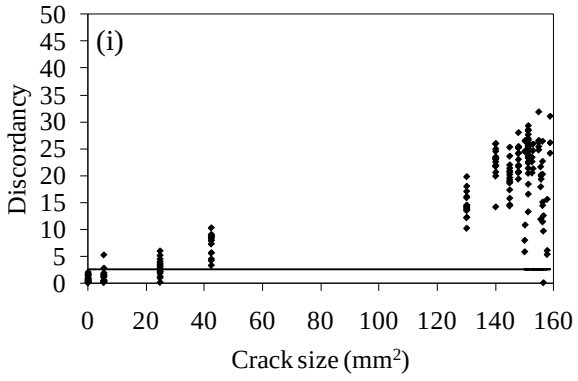
(i)
Discordancy
Crack size (mm²)

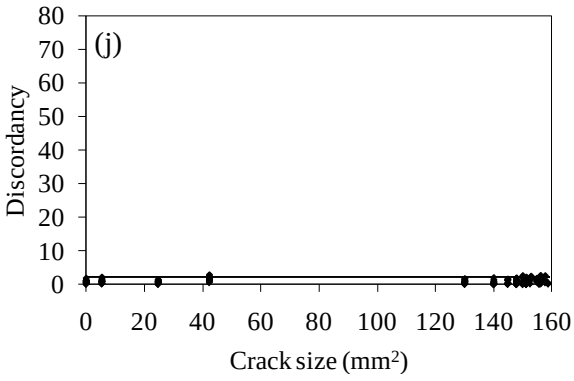
(j)
Discordancy
Crack size (mm²)

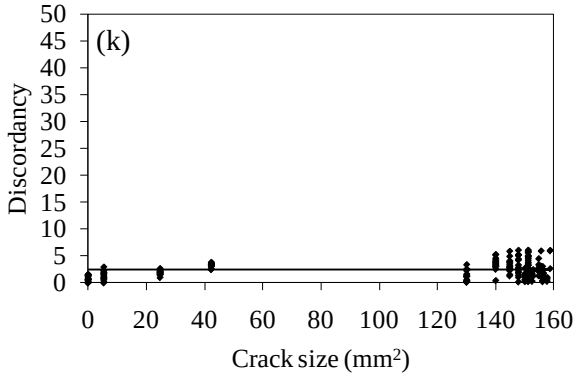
(k)
Discordancy
Crack size (mm²)

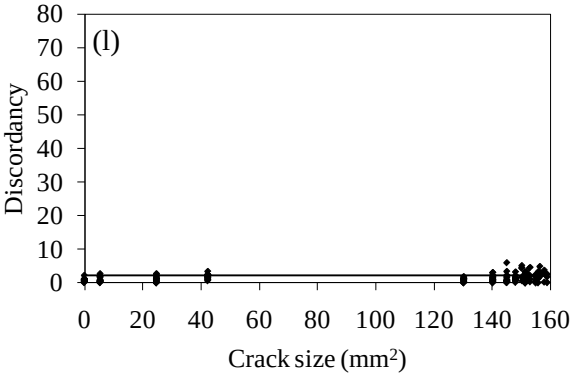
(l)
Discordancy
Crack size (mm²)

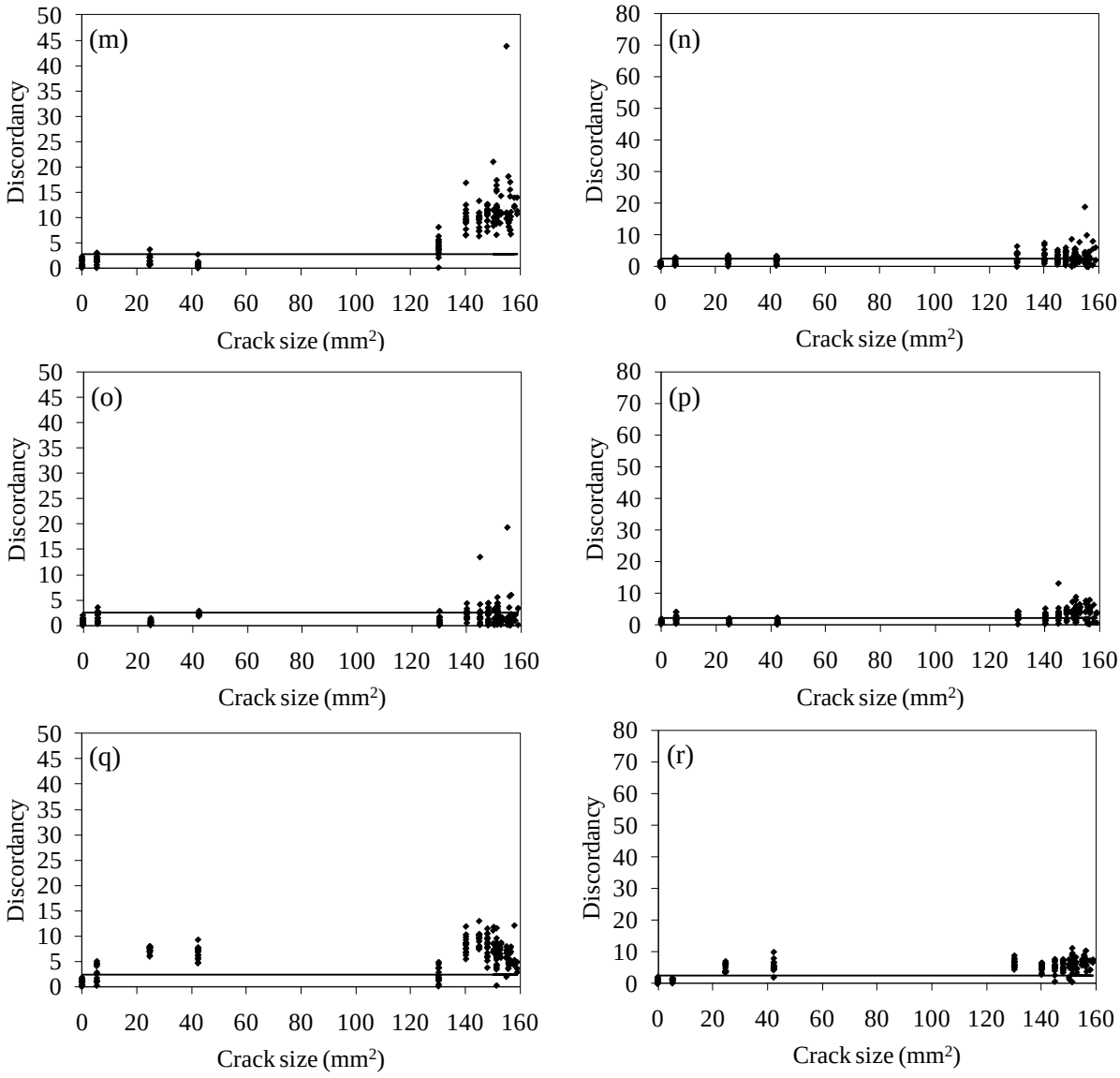

Figure 4.1 - Univariate analysis. Discordancy as a function of the crack size for the following features andactuator-sensor pairs: (a) RMS_S5=>S8/S5=>S4 (b) Ppk_S5=>S8/S5=>S4; (c) RMS_S9=>S6/S9=>S8 (d) Ppk_S9=>S6/S9=>S8 (e) RMS_S5=>S0/S5=>S4 (f) Ppk_S5=>S0/S5=>S4; (g) RMS_S5=>S6/S5=>S4 (h) Ppk_S5=>S6/S5=>S4 (i) RMS_S5=>S1/S5=>S4 (j) Ppk_S5=>S1/S5=>S4; (k) RMS_S0=>S4/S0=>S2 (l) Ppk_S0=>S4/S0=>S2 (m) RMS_S0=>S5/S0=>S1 (n) Ppk_S0=>S5/S0=>S1; (o) RMS_S0=>S4/S0=>S1 (p) Ppk_S0=>S4/S0=>S1 (q) RMS_S9=>S1/S9=>S8 (r) Ppk_S9=>S1/S9=>S8;

The damage detection rate, i.e. the percentage of outliers of the features selected in this study associated with six actuator-sensor pair's ratios, is summarized in Table 4.1. The table demonstrates that the proper selection of wave path and statistical features are pivotal to

enhancing the damage sensitivity of the hardware system. Because paths S5=>S4 and S0=>S1 should not be affected by the presence of damage at or around the joints, these paths can be used to normalize ultrasonic data in order to mitigate any effect due to changes in the environmental conditions, electronic noise/power, and PZT-structure interaction. Although the sensing paths S5=>S1 and S5=>S0 are similar, it is interesting to note that the detection rate for some features is quite different. The same can be said about sensing paths S0=>S4 and S0=>S5. Observing the last two columns of Table 4.1, it can be noted that although actuators S0 and S5 are placed symmetrically with respect to sensor S8, sensing path S5=>S8 is strongly affected by the presence of the crack. This result suggests that the algorithm can be indirectly used to identify the position of the crack. Somehow it is surprising to observe the effect of the damage on certain features associated with guided waves propagating along path S0=>S1.

Table 4.1 - Univariate Analysis: the percentage of outliers detected using statistical features applied to waveform data associated with some of the actuator-sensor pairs considered in this study.

Feature	S5=>S1 /S5=>S4	S5=>S0 /S5=>S4	S0=>S4 /s0=>S1	S0=>S5 /S0=>S1	S5=>S8 /S5=>S4	S0=>S8 /S0=>S1
Krt	58.05%	94.25%	80.46%	31.61%	95.40%	61.49%
RMS	87.93%	83.33%	23.56%	74.14%	92.53%	90.23%
Variance	87.93%	83.33%	23.56%	74.14%	92.53%	93.68%
K-factor	4.022%	36.21%	43.68%	55.17%	94.25%	10.34%
Max	5.172%	43.68%	55.75%	51.72%	95.40%	8.046%
Ppk	10.92%	54.6%	62.64%	35.06%	83.91%	57.47%
Crest	50.0%	78.74%	25.29%	81.03%	94.25%	27.01%

4.1.2 Multivariate Analysis

The features considered separately in the previous section were used simultaneously to construct a multi-dimensional D.I. vector for the outlier analysis. The “exclusive” MSD for each of the 192 measurements was calculated using Eq. 3.2. The purpose of combining features was to increase the sensitivity to damage compared to the single-feature analysis. However, the use of all may

not be necessary and the selection of all features may degrade the detection performance. To investigate this aspect, a parametric analysis was carried out. All of the features discussed in the previous section were considered, ranging from all combinations of two-dimensional D.I. vectors to the single combination of the 7-dimensional vector. A total of 3,120 cases were analyzed. The total is the result of the application of all 120 possible features' combinations to each of the 26 D.I.s considered in this study.

Fig. 4.2 shows the results of the single combination of the 7-dimensional vector formed by the statistical features applied to the following features' ratios: S5=>S0/S5=>S4, S9=>S6/S9=>S8, S5=>S8/S5=>S4, S5=>S6/S5=>S4, S5=>S1/S5=>S4, S0=>S4/S0=>S2, S0=>S5/S0=>S1 and S0=>S4/S0=>S1, respectively. The improvement of the sensitivity is immediately visible by comparing the ordinate axis of Fig. 4.2 with the ordinate axis of Fig. 4.1. The improvement implies that variation in crack sizes determine large variations of the MSD value. By comparing the MSD presented in Fig. 4.2, it also evident that a certain waveform path, i.e. position of the PZTs, outperforms other paths. For instance, the values presented in Fig. 4.2 (c) show a small scatter at a given damage size and better stepwise behavior. To find empirically the best feature combination and the best wave propagation path, a quantitative study was performed using the values of the MSD associated with each of the 3,120 cases. The selection was done on the logarithmic magnitude values of the measurements and it was based on the ranking of their performance as novelty detectors. Figure 4.3 shows the results associated with from the best to the worst combination cases. The combination ranked '1st' provided the largest number (100%) of outliers and the largest ratio of the Mahalanobis distance over the threshold. Figure 4.3 (a) shows the MSD as a function of the crack area from the time waveforms associated with paths S5=>S8/S5=>S4 and statistical features krt, cf, kf, ppk, and max. Fig. 4.3 (h) presents the result of the multivariate analysis associated with D.I.08/01 and features max and ppk. Only 12.07% of the outliers were properly identified.

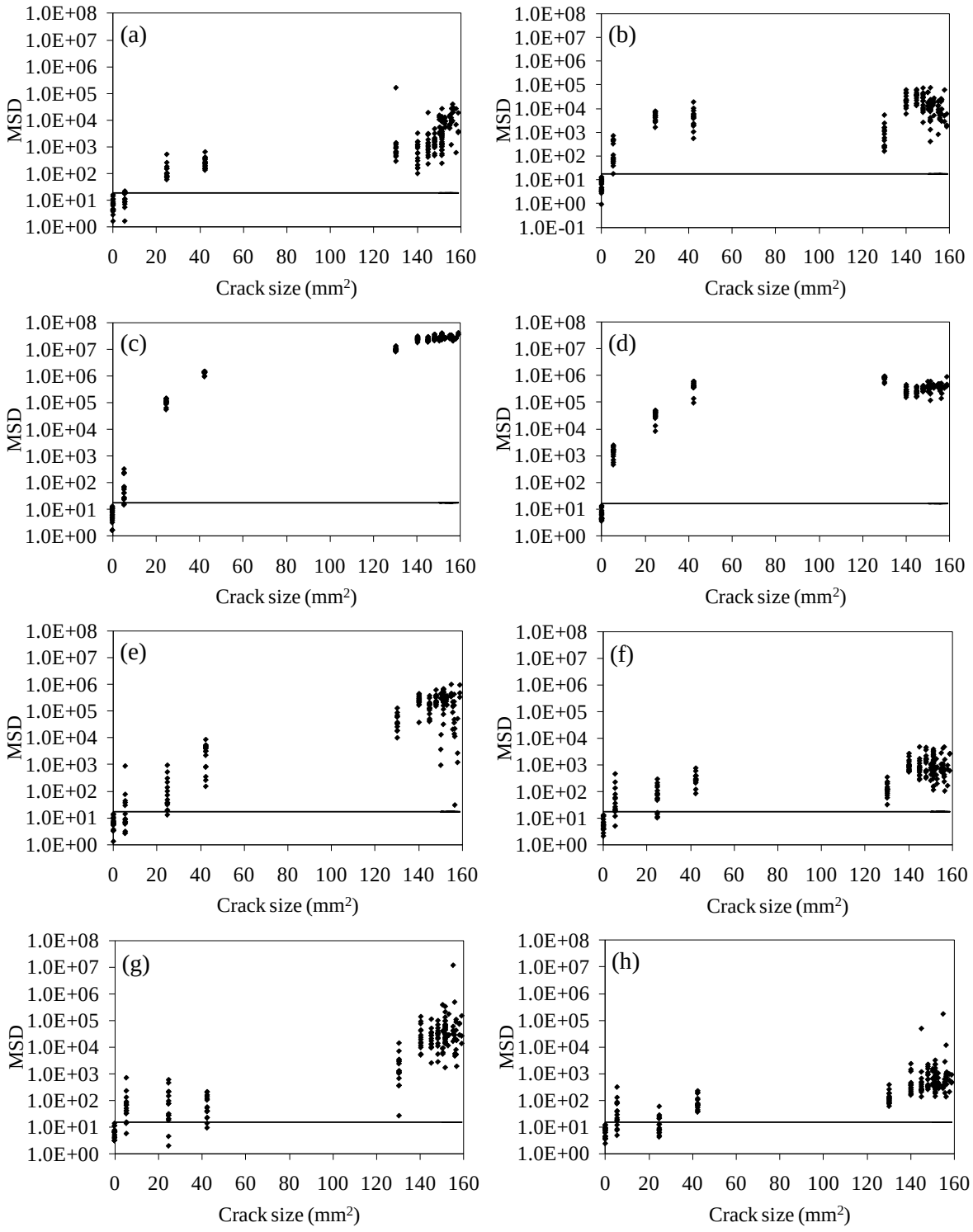

Figure 4.2- Multivariate analysis. Mahalanobis squared distances as a function of the crack size for theactuator-sensor pairs considering all 7 features: (a) S5=>S0/S5=>S4; (b) S9=>S6/S9=>S8; (c) S5=>S8/S5=>S4; (d) S5=>S6/S5=>S4; (e) S5=>S1/S5=>S4; (f) S0=>S4/S0=>S2; (g) S0=>S5/S0=>S1; (h) S0=>S4/S0=>S1.

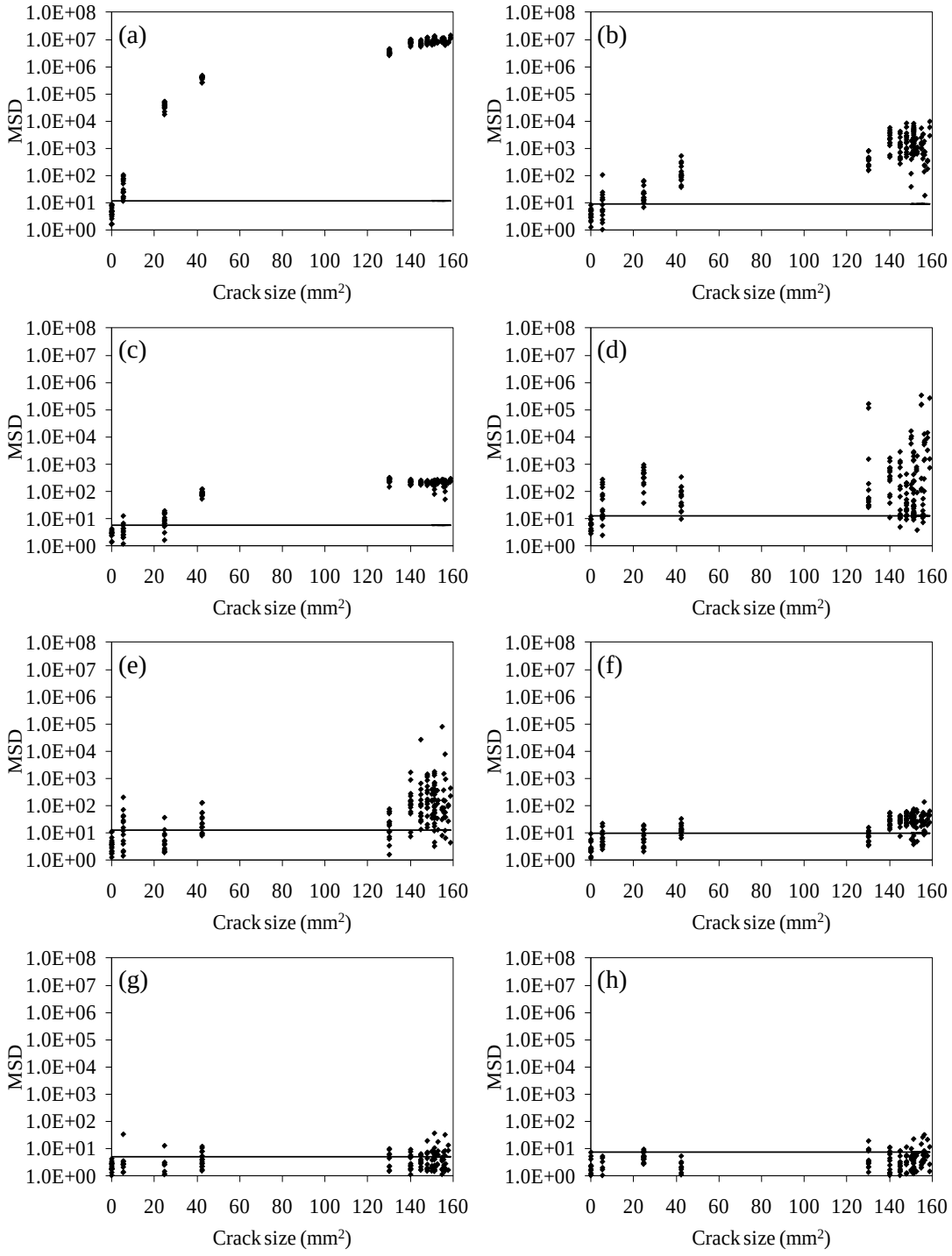

Figure 4.3 - Multivariate analysis. Mahalanobis squared distances as a function of the crack size for the actuator-sensor pairs: (a) S5=>S8/S5=>S4 with krt, cf, kf ppk and max; (b) S5=>S2/S5=>S4 with krt, var, cf, kf, max and ppk; (c) S5=>S6/S5=>S4 with kf and max; (d) S5=>S7/S5=>S4 with krt, var, cf, kf, max and ppk; (e) S0=>S4/S0=>S1 with rms, var, kf and max; (f) S0=>S4/S0=>S2 with rms, cf and ppk; (g) S5=>S2/S5=>S4 with max and ppk; (h) S0=>S8/S0=>S1 with max and ppk; krt, rms, var, cf, kf, max and ppk

4.1.3 Multiple frequencies analysis

In order to investigate the effect of the propagating frequency on the damage detection performance of the UGW approach, a portion of the study was devoted to the generation and detection of toneburst center at frequencies ranging from 100 kHz to 275 kHz at 25 kHz step. The results of such investigation to detect the presence of damage in Test 1 are presented in this section.

An example of time waveforms detected at various frequencies when the transducer pair S5=>S0 were activated are presented in Fig. 4.4. Because the generation and detection of 100 kHz toneburst lead to poor signal to noise ratio, its further analysis was excluded. By observing Figs. 4.4 (a) – (h) it is possible to observe that the frequency range 150 – 200 kHz provides the highest signal to noise ratio.

The vertical dotted lines identify the time window analysis considered for the subsequent structural health monitoring algorithm. For consistency with the analysis described in the previous section the same features and the same outlier analysis was applied to each and every frequency examined in this study.

The quantitative results of detection rate of the discordancy tests (multivariate analysis) applied to the damage index associated with all seven features and the selected windowed time waveforms are shown in Fig. 4.5. In Fig. 4.5, the histograms are shown as a function of frequency for all 7 features and selected wave paths considered in this study. In particular, the damage indexes $D.I._{50/54}$, $D.I._{96/98}$, $D.I._{58/54}$, $D.I._{04/01}$, $D.I._{65/67}$, and $D.I._{05/01}$ associated with the krt, var, RMS, max, ppk, crest and kf are presented. By comparing all six wave paths and seven features the krt-based, var-based and RMS-based damage indexes extracted from the selected windowed time waveforms provided the highest detection rate and 150 kHz, 175 kHz and 200 kHz are the optimal frequencies.

Moreover, by comparing the performance of the detection rates for specified frequency and certain feature, the histograms demonstrate that the proper selection of wave path are pivotal to enhancing the damage sensitivity of the hardware system. As mentioned earlier, paths S5=>S4, S0=>S1 and S6=>S7 should not be affected by the presence of damage at or around the joints. Thus, these paths were used to normalize ultrasonic data in order to mitigate any effect due to

changes in the environmental conditions, electronic noise/power, and PZT-structure interaction. The sensing path S5=>S8 is strongly affected by the presence of the first crack as observed in Fig. 4.5 (c). Considering the symmetrical case of S5=>S0/ S5=>S4 (Fig. 4.5 (a)) and S0=>S5/ S0=>S1 (Fig. 4.5(f)), the different performances suggests that the algorithm could be indirectly used to identify the position of the crack. Fig. 4.6 shows instead the results of the multivariate analysis when all seven features were considered for eight different paths.

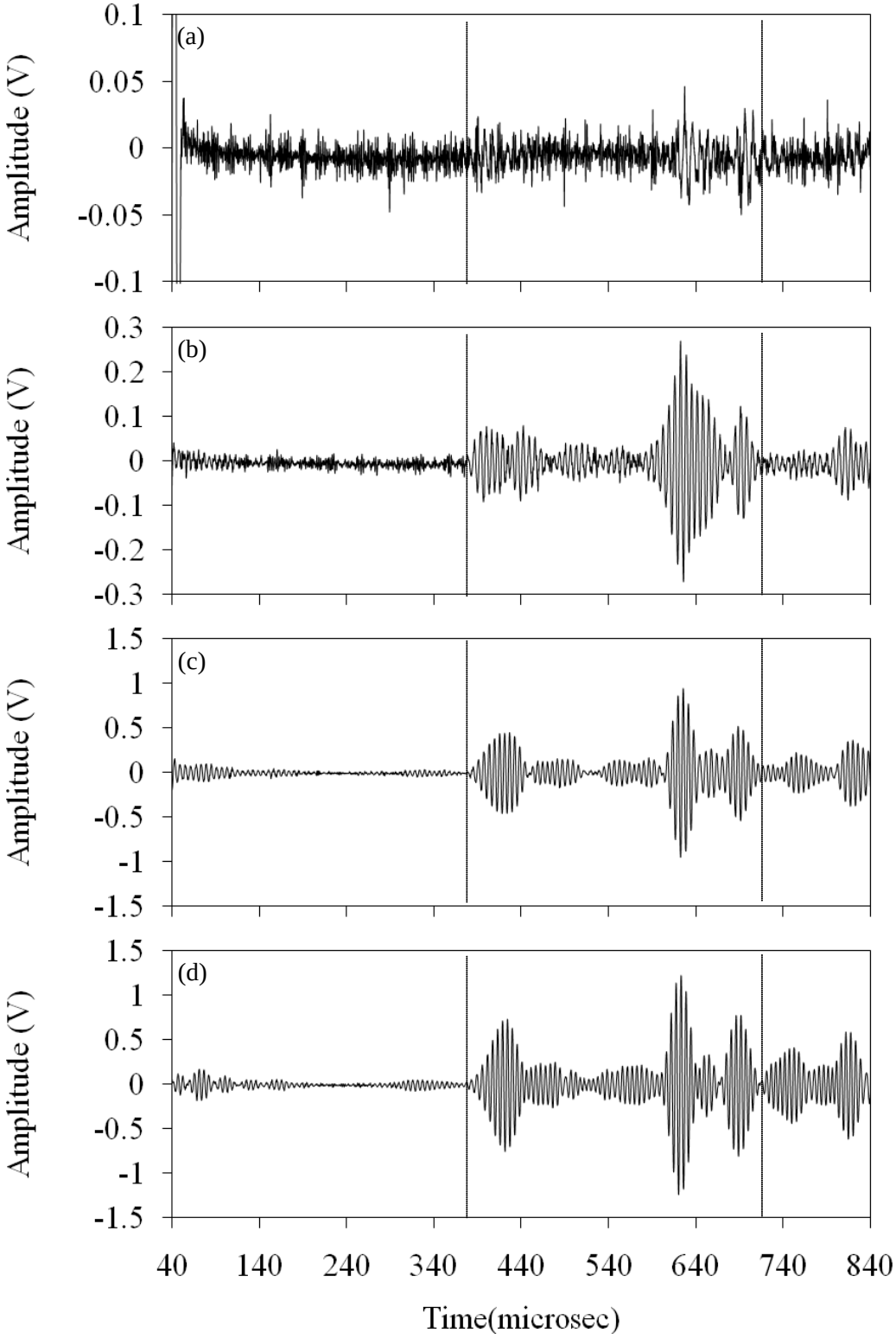
(a)
(b)
(c)
(d)
Amplitude (V)
Amplitude (V)
Amplitude (V)
Amplitude (V)
0.1
0.05
0
-0.05
-0.1
0.3
0.2
0.1
0
-0.1
-0.2
-0.3
1.5
1
0.5
0
-0.5
-1
-1.5
40
140
240
340
440
540
640
740
840
Time(microsec)

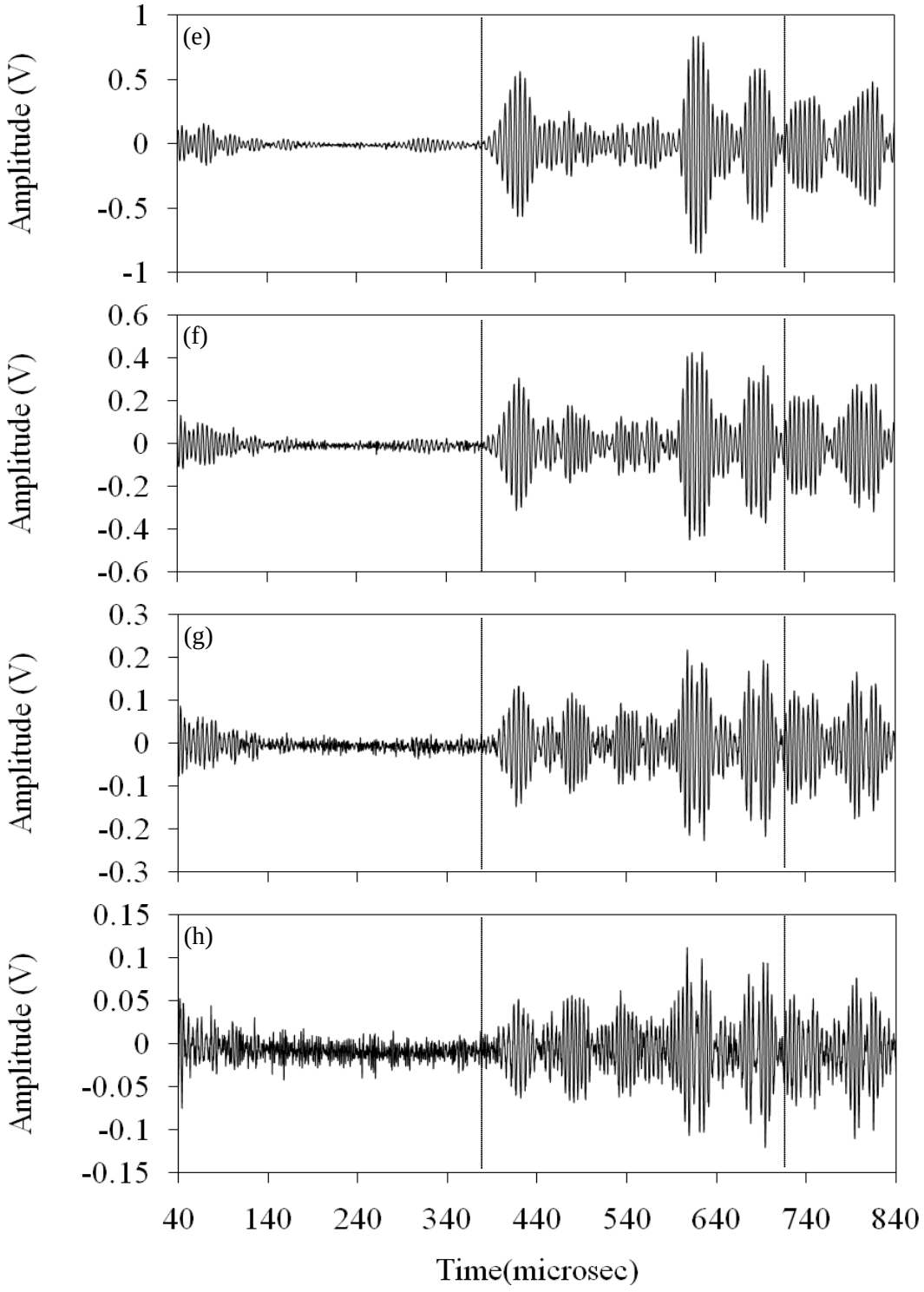

Figure 4.4 - Time waveforms of S5=>S0 in different frequencies: (a) 100 KHz; (b) 125 KHz; (c) 150 KHz; (d) 175 KHz; (e) 200 KHz; (f) 225 KHz; (g) 250 KHz; (h) 275 KHz.

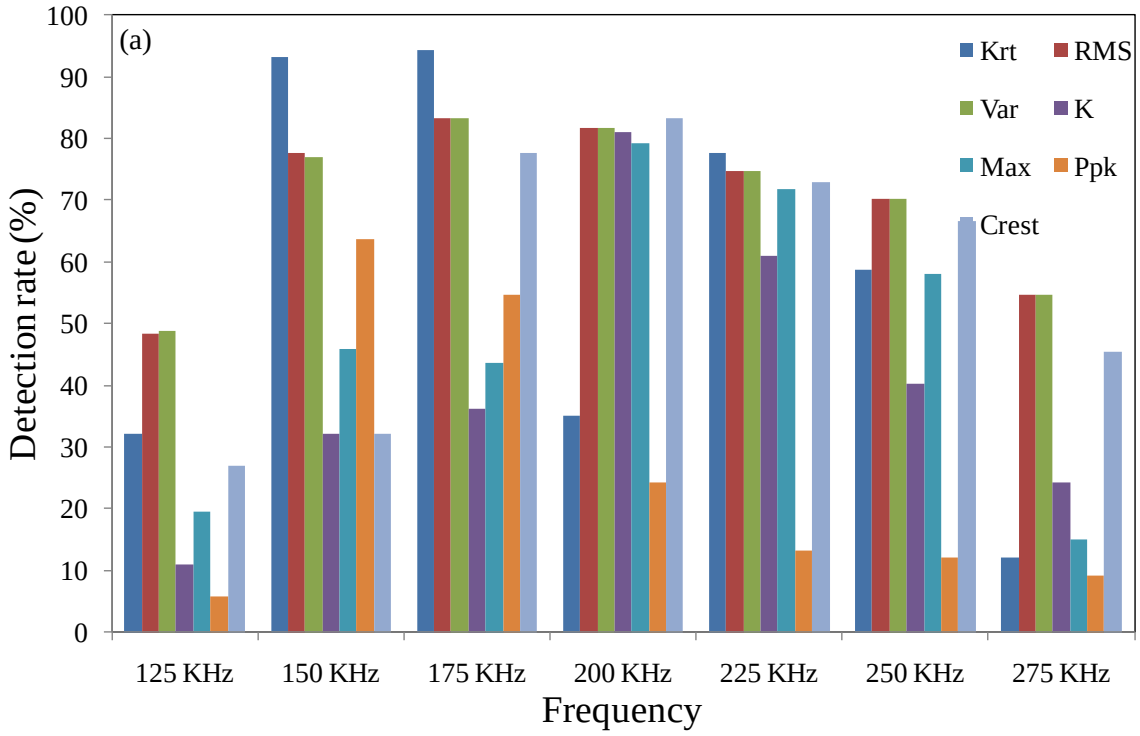
(a)
Krt
RMS
Var
K
Max
Ppk
Crest
Detection rate (%)
100
90
80
70
60
50
40
30
20
10
0
125 KHz
150 KHz
175 KHz
200 KHz
225 KHz
250 KHz
275 KHz
Frequency

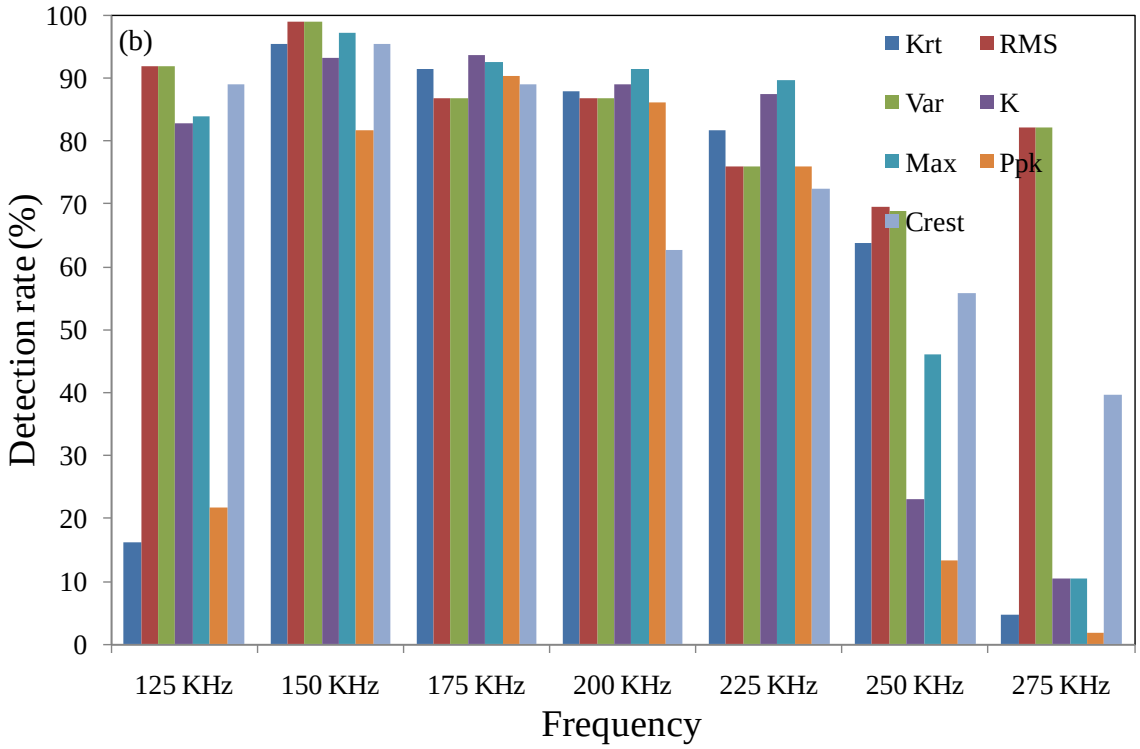
(b)
Krt
RMS
Var
K
Max
Ppk
Crest
Detection rate (%)
100
90
80
70
60
50
40
30
20
10
0
125 KHz
150 KHz
175 KHz
200 KHz
225 KHz
250 KHz
275 KHz
Frequency

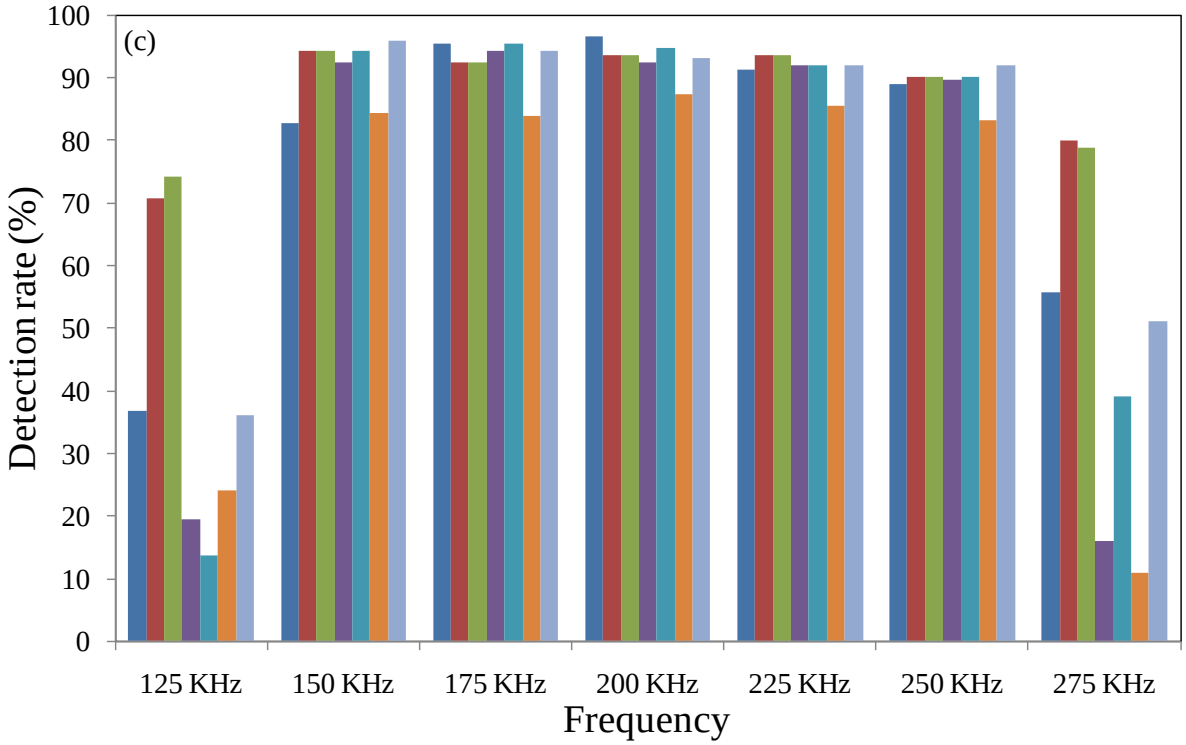
(c)
Detection rate (%)
100
90
80
70
60
50
40
30
20
10
0
125 KHz
150 KHz
175 KHz
200 KHz
225 KHz
250 KHz
275 KHz
Frequency

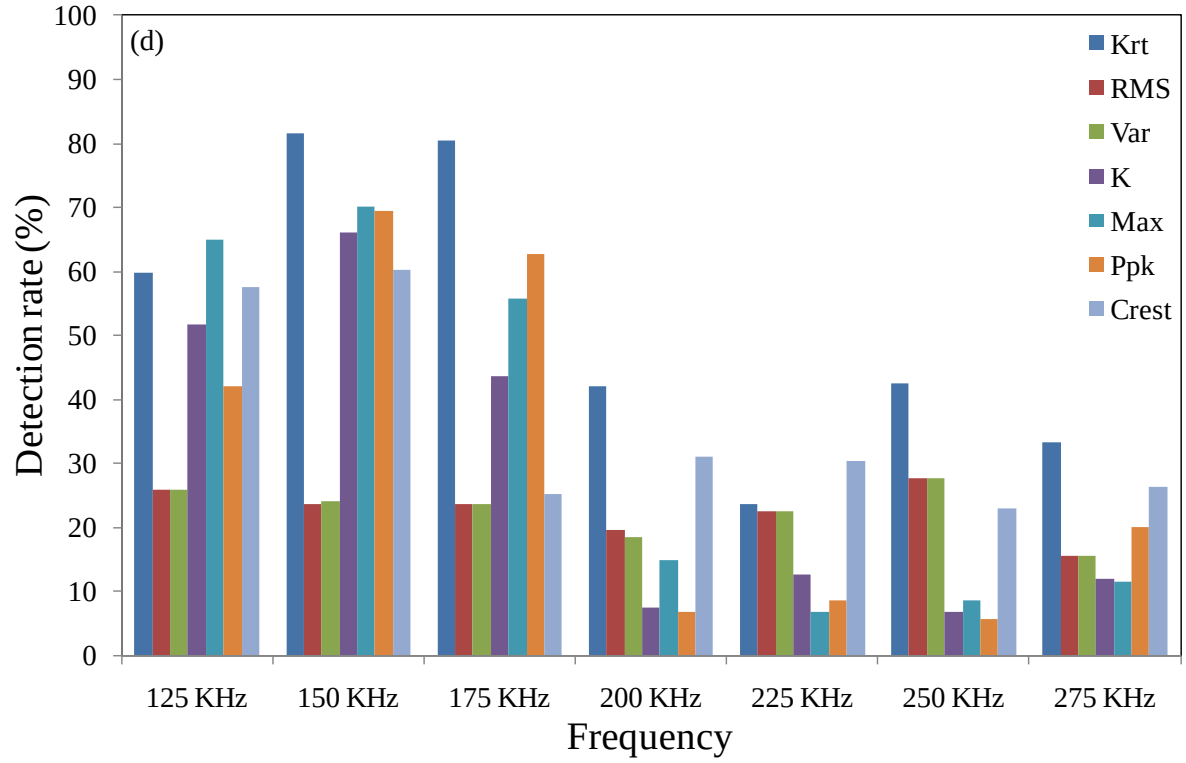
(d)
Krt
RMS
Var
K
Max
Ppk
Crest
Detection rate (%)
100
90
80
70
60
50
40
30
20
10
0
125 KHz
150 KHz
175 KHz
200 KHz
225 KHz
250 KHz
275 KHz
Frequency

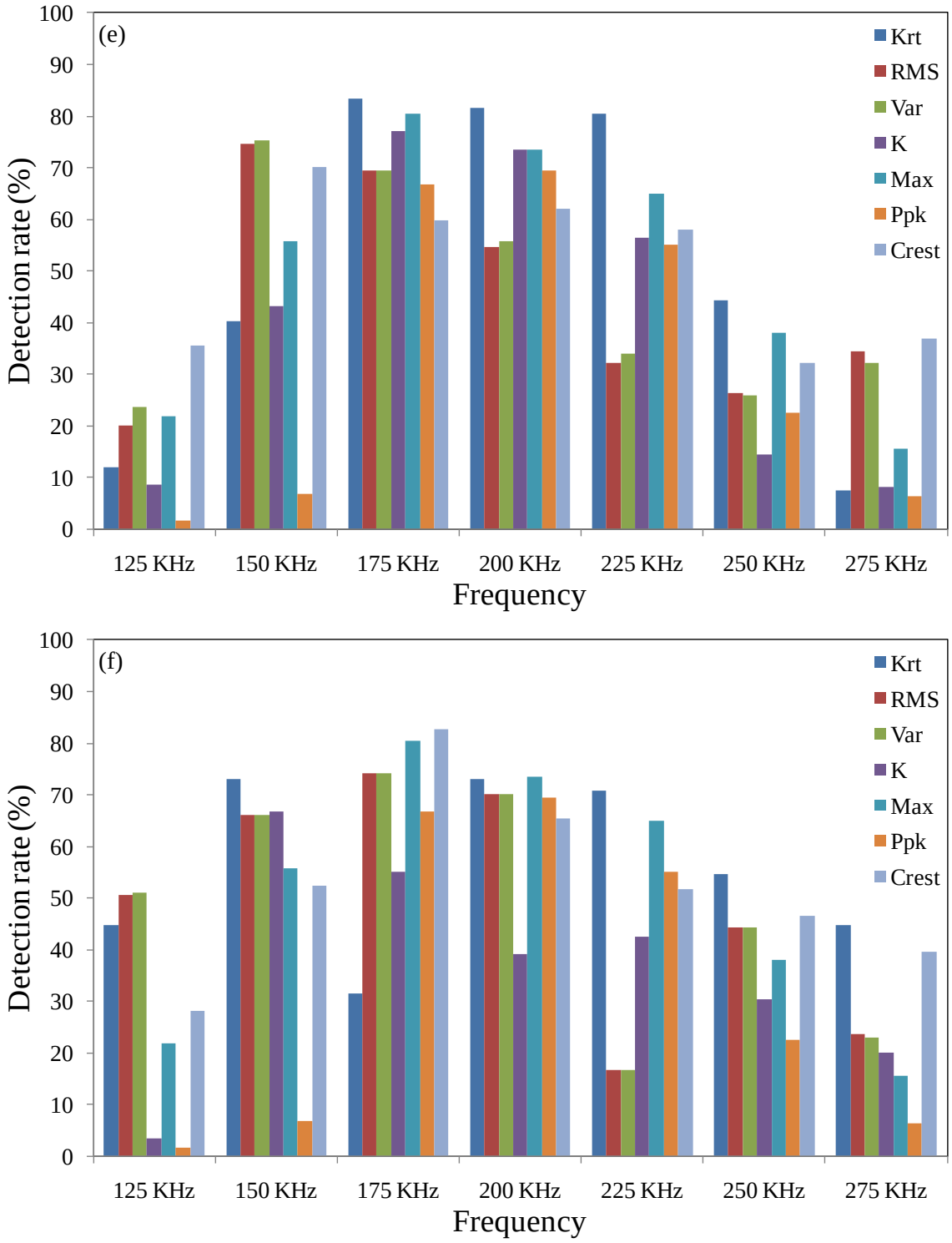

Figure 4.5 - Univariate analysis. Detection rate as a function of frequency for the following features: (a) S5=>S0/S5=>S4 (b) S5=>S6/S5=>S4; (c) S5=>S8/S5=>S4 (d) S0=>S4/S0=>S1 (e) S6=>S5/S6=>S7 (f) S0=>S5/S0=>S1.

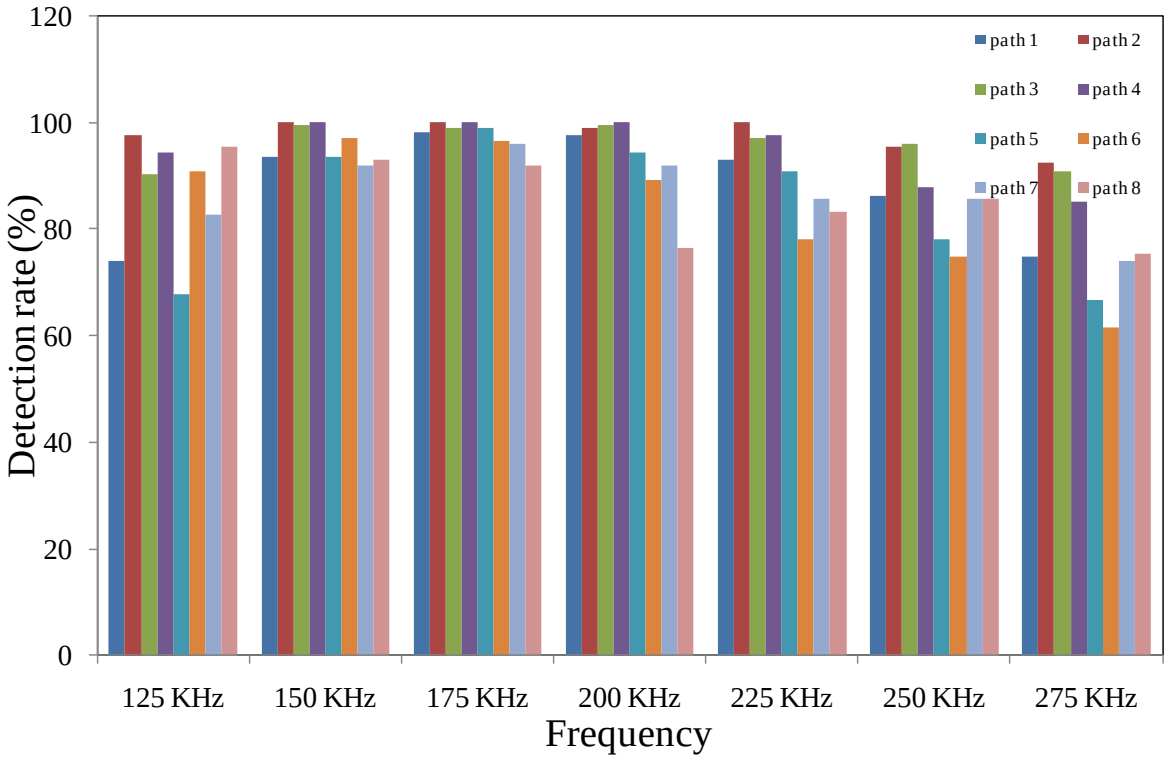

Figure 4.6 - MSD considering all 7 features: path (1) S5=>S0/S5=>S4; (2) S9=>S6/S9=>S8; (3) S5=>S8/S5=>S4; (4) S5=>S6/S5=>S4; (5) S5=>S1/S5=>S4; (6) S0=>S4/S0=>S2; (7) S0=>S5/S0=>S1; (8) S0=>S4/S0=>S1;

4.2 TEST 2

In Test 1, the multivariate analysis was proved to be more effective in terms of crack growth detection in comparison with univariate analysis. Thus, only the multivariate analysis was performed to analyze the data from Test 2. The features considered in the previous section were used simultaneously to construct a multi-dimensional D.I. vector for the outlier analysis. The "exclusive" MSD for each of the 124 measurements was calculated using Eq. 3.2. As done for the data associated with Test 1, all of the seven feature types discussed in the previous section were considered, ranging from all combinations of two-dimensional D.I. vectors to the single combination of the 7-dimensional vector. A total of 3,120 cases were analyzed. The total is the

result of the application of all 120 possible features' combinations to each of the 26 D.I.s considered in this study.

Fig. 4.7 shows the results of the single combination of the 7-dimensional vector formed by the statistical features applied to the following features' ratios: S9=>S6/S9=>S8, S9=>S1/S9=>S8, S5=>S6/S5=>S4, S5=>S1/S5=>S4, S0=>S4/S0=>S2, S0=>S5/S0=>S1, S0=>S4/S0=>S1, and S5=>S0/S5=>S4 against cycle number respectively. As the abscissas range from 0 to 480,000, the plots present the results associated with both Test 1 (0 – 180,000) and Test 2 (180,001 - 485,000). By comparing the MSD presented in Fig. 4.7, it is once more evident that certain waveform paths outperform other paths in terms of crack growth detection. For Fig. 4.7 (a), (b), (c) and (d), the MSD values increased during the first 180,000 cycles and stay relatively constant from 180,000 to 485,000. For instance, the wave path S5=>S6/S5=>S4 increased dramatically at the first 25,000 cycles in which crack 1 was artificially increased, and stayed constant in Test 2 for the reason that the crack 2 was 'shadowed' by the welding joints. For Fig. 4.7 (e), (f) and (g), increasing tendency could be observed from 180,000 to 330,000 cycles, which suggests the crack growth along this period. Thus, different behaviors of one PZT wave path in different tests and of different PZT wave path in same test suggest the possibility of crack growth detection and crack localization.

It must be remarked that the cluster of data observed in Fig. 4.7 (a), (b), and (c) and located between 295,000 and 340,000 cycles are related to lost connections occurred at sensors 6, 7, and 8. After the connection was re-established a small shift of MSD values is observed.

To find empirically the best feature combination and the best wave propagation path able to detect the second crack, a quantitative study was performed using the values of the MSD associated with each of the 3,120 cases. The ranking was first executed in terms of percentage of outliers detected. Among the wave paths and feature combinations that were able to detect all damaged states, the combination ranked '1^{st}' provided the largest ratio of MSD values between values after 330,000 cycles and values between 40,000 and 180,000 cycles.

For comparative purposes, Fig. 4.8 shows the best and worst cases. Fig. 4.8 (a) shows the MSD as a function of the cycle number from the time waveforms associated with path of S1=>S4/S1=>S2 and statistical features rms and var. Different patterns comparing MSD values of Test 1 which is the first 180,000 cycles and Test 2 suggests that the path of S1=>S4/S1=>S2

with features of rms and var was sensitive to the 2nd crack (stepwise behavior at Test 2) and 'deaf' to the first crack (constant behavior with variance at Test 1). Fig. 4.8 (h) presents the result of the multivariate analysis associated with D.I. of S5=>S6/S5=>S4 with features of krt, rms, var, cf, kf, and max, which suggests that this path with this set of features was sensitive for the first crack (stepwise behavior at first 25,000 cycles) and not affected by the second crack (stay constant until the connection lost).

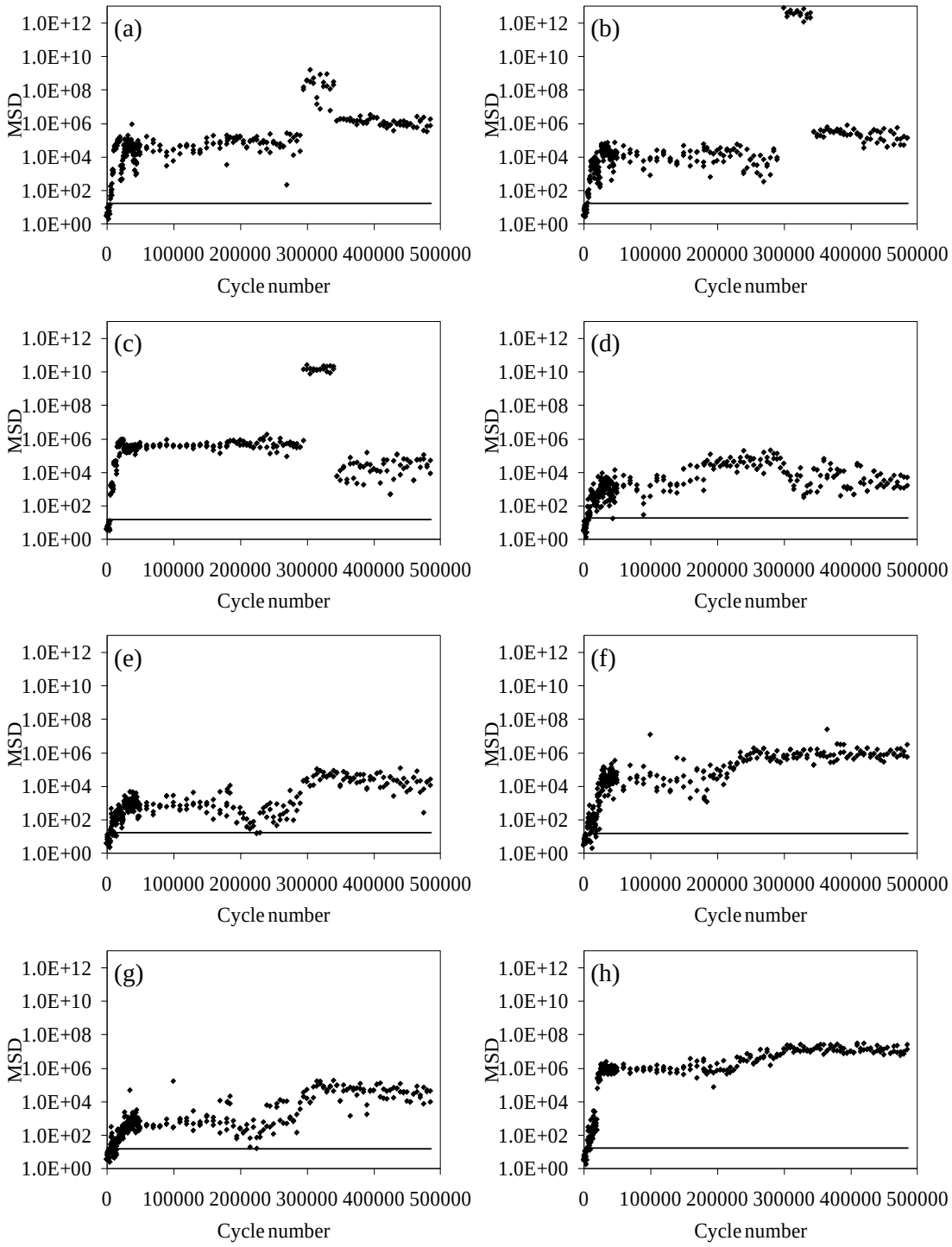

Figure 4.7 - Multivariate analysis. Mahalanobis squared distances as a function of the crack size for the actuator-sensor pairs considering all 7 features: (a) S9=>S6/S9=>S8; (b) S9=>S1/S9=>S8; (c) S5=>S6/S5=>S4; (d) S5=>S1/S5=>S4; (e) S0=>S4/S0=>S2; (f) S0=>S5/S0=>S1; (g) S0=>S4/S0=>S1; (h) S5=>S0/S5=>S4

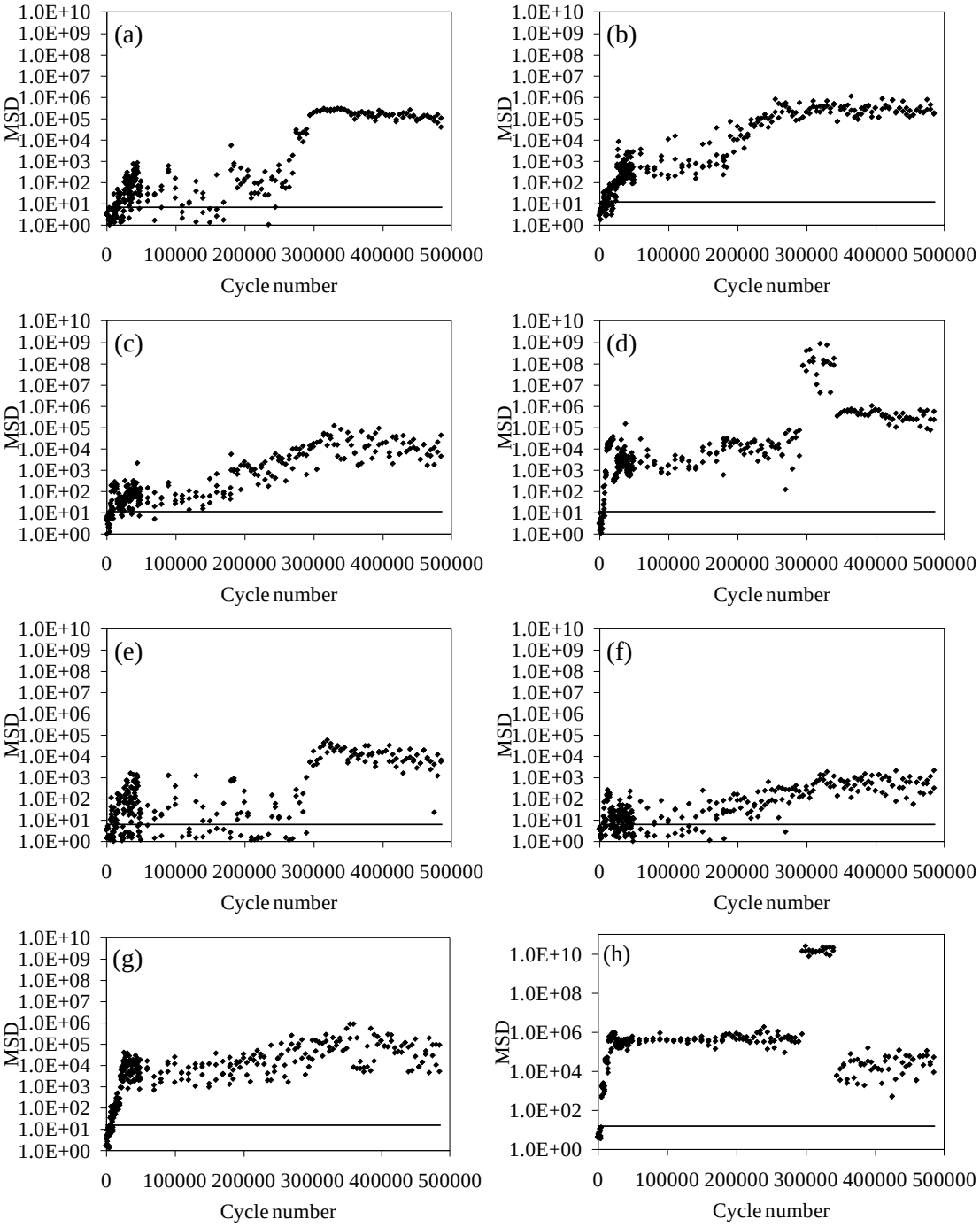

Figure 4.8 - Multivariate analysis. Mahalanobis squared distances as a function of the crack size for the actuator-sensor pairs: (a) S1=>S4/S1=>S2 with rms and var (b) S0=>S5/S0=>S1 with krt, var, cf, kf, and ppk (c) S1=>S5/S1=>S2 with krt, var, cf, and kf (d) S9=>S6/S9=>S8 with rms, var, cf, and ppk; (e) S0=>S4/S0=>S2 with rms and var; (f) S1=>S4/S1=>S2 with krt and max;(g) S5=>S0/S5=>S4 with krt, rms, kf, max and ppk; (h) S5=>S6/S5=>S4 with krt, rms, var, cf, kf, and max.

4.3 TEST 3

Following the outcomes from tests 1 and 2, few wave paths were considered for the analysis of the data associated with Test 3. The procedure used for the analysis of the time waveforms was the same adopted for Test 1 and 2, i.e. the first three or four wave energy packets were included considered for the extraction of the seven statistical features discussed in Chapter 3.3.1.

For convenience Table 4.1 is summarized in Table 4.2, which clusters several measurements under a certain combination of temperature, condition, and damage level.

Table 4.2 - Test 3. Summary of boundary condition, steel temperature, and joint condition.

Measurement #	Temp C	Boundary	Inside/outside	Damage
1 - 10	**17.7**	Dry	i	pristine
11 - 20	**6.7**	melting snow	i	pristine
21 - 22	**8.2**	Dry	i	pristine
23 - 27	**2**	Dry	o	pristine
28 - 32	**2.7**	Dry	o	pristine
33 - 42	**0.2**	Snow	o	pristine
43 -47	**-2**	Snow	o	pristine
48 -49	**6.5**	Dry	i	pristine
50 - 51	**22**	Dry	i	pristine
52 - 53	**17.2**	Dry	i	damage 1
54 - 55	**22**	Dry	i	damage 1
56 - 60	**3**	melting snow	i	damage 1
61 - 65	**3**	Dry	i	damage 1
66 - 70	**3**	Dry	i	damage 2
71 - 75	**0.3**	melting snow	i	damage 2
76 - 80	**10**	Dry	i	damage 2
81 - 85	**22**	Dry	i	damage 2

Fig. 4.9 shows the values of the RMS as a function of the measurement points for the following wave paths: (a) S3=>S4/S3=>S2; (b) S3=>S0/S3=>S2; (c) S0=>S3/S0=>S1; (d) S0=>S4/S0=>S1. Paths S3=>S2 and S0=>S1 were chosen since the relative position of the

sensors were such that the direct propagation of the wave from S0 to S1 or from S3 to S2 should not be affected by the presence of damage.

Therefore evaluating the ratio of features using S3=>S2 or S0=>S1 is expected to normalize any effect associated with temperature or boundary conditions.

Given the positions of the transducers with respect to the location of the flaw, the damage index ratio S3=>S4/S3=>S2 plotted in Fig. 4.9 (a) is expected to be affected by the presence of the damage, while the S0=>S4/S0=>S1 damage index plotted in Fig. 4.9 (d) is likely to be immune by the notch.

Although damage index ratios are considered, it is evident from Fig. 4.9 that the values of the RMS are affected by the environmental conditions. By looking at Fig. 4.9 (a) it is visible a drop in the RMS values in the measurement number range 11-49 when the structure was in pristine condition but the temperatures were several degrees Celsius below the baseline (17.7 C = 63.9 F). When the temperature of the steel was raised up to 22 C (71.6 F) by means of a heat gun and the structure was still pristine, the value of the RMS ratio was about 12% higher than the baseline, i.e. data taken during the first ten measurements. It should be noted that the heat gun was used with the objective of heating the chord along the span between sensors S0 and S3 uniformly. However, owing to the nature of the approach, it should not be excluded that a temperature differential between sensors was possible. When the small notch was present and the structure was cooled a decrease on the value of the RMS is visible. A step wise behavior is visible in Fig. 4.9 (a) between range 61-65 and 66-70. Both ranges were under the same temperature and boundary conditions. The latter range was measured with larger crack. This means that the step clearly visible in Fig. 4.9 (a) is associated with the increase of the size of damage. This hypothesis is corroborated by comparing the values of the RMS along the same range for Fig. 4.9 (b), (c), and (d). These three figures also confirm that the wave paths used for the analysis were not affected by the presence of damage, due to the relative position of the PZTs with respect to the notch. The presence of melting snow on portions of the chord along the wave paths (measurements 11 – 20) caused large scattering of the RMS values. The scattering is probably due to non-uniform melting that created various boundary conditions across different measurements. When compared to the baseline RMS values at 21 and 22 were taken under lower temperatures.

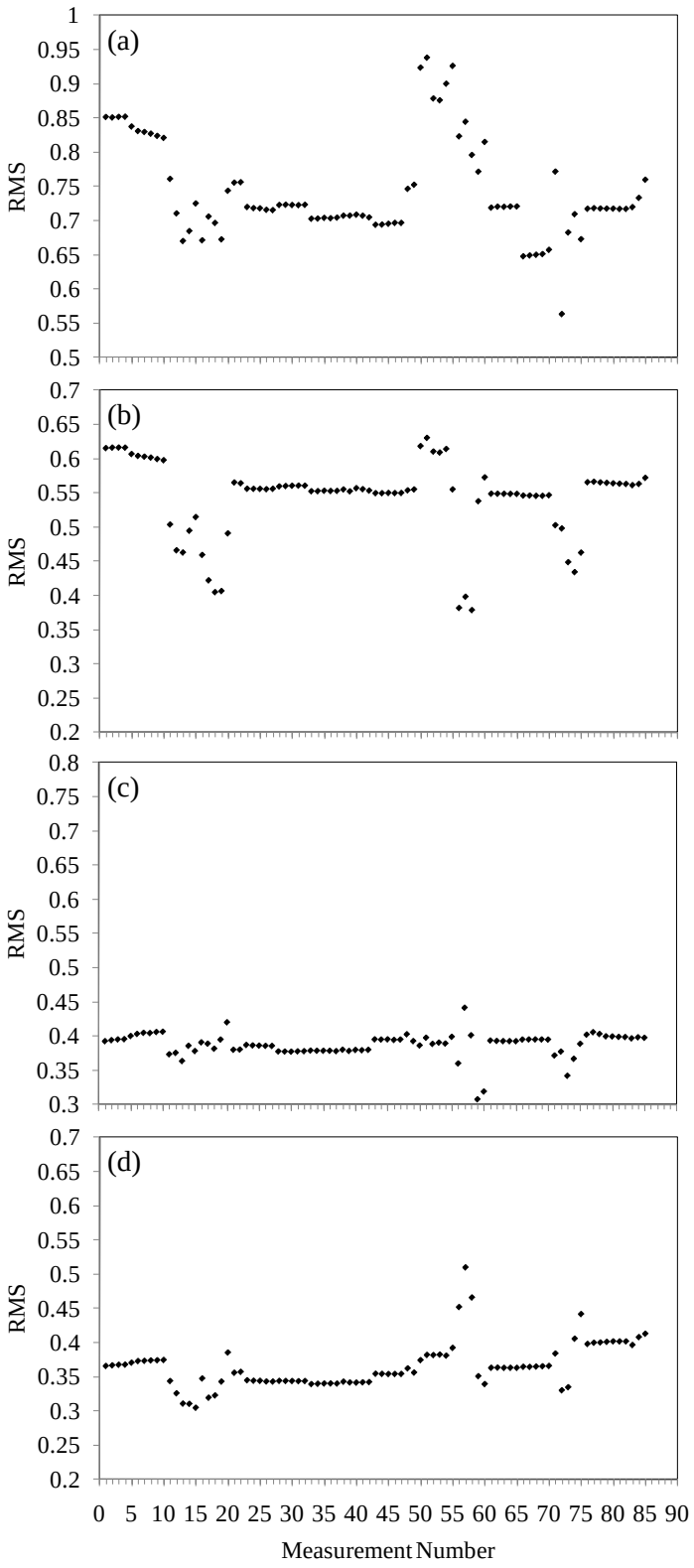

Figure 4.9– Root Mean Square values as a function of the measurement number for: (a) S3=>S4/S3=>S2; (b) S3=>S0/S3=>S2; (c) S0=>S3/S0=>S1; (d) S0=>S4/S0=>S1.

An 11.76% decrease in Damage Index values suggests a positive correlation between the selected D.I. and temperature. For the measurement from 23 to 47, the natural snow and temperature drop were involved in the experiment, and which evident the conclusion about the positive correlation between D.I. and temperature. The decrease of the ratio values across measurement 52 to 60 confirms the hypothesis that a decrease in temperature induces a decrease in RMS ratio observes looking across the measurement range 1-20.

The size of the artificial defect was augmented after measurement 65. Across measurements 61 to 70, the temperature and boundary conditions were purposely left the same. Therefore the step visible in Fig. 4.9 (a) should be associated to the increase of damage size. During the last twenty measurements (66 - 85) stepwise increases were observed as a consequence most likely of temperature increase.

Overall, by comparing the values plotted in Fig. 4.9 (a), the range of the RMS values with respect to the baseline spans from +11.7% (measurement 51) to -35.2% (measurement 72).

Similar considerations can be made by observing Fig. 4.9 (b)-(d). For these three figures it should be noted that the scattering from the baseline data is lower when compared to Fig. 4.9 (a). The effect of the temperature over the values of the RMS ratio seems higher than the effects associated with the boundary conditions and the boundary condition. To isolate the effect of the temperature and boundary conditions from the effect of damage the statistical features associated with the time waveforms along paths S3=>S2 and S0=>S1 were investigated. Owing to the position of PZTs S0, …, S3, these two path must have been immune from defect, as long as the portion of the time series considered did not interfered with any reflections from the notch. The values of the RMS as a function of the measurement number associated with these two paths are presented in Fig. 4.10 (a) and (b). The normalized values of the RMS are overlapped in Fig. 4.10 (c). Fig. 4.10 shows that although some quantitative differences on the values of the RMS the overall changes associated with varying conditions are quite similar.

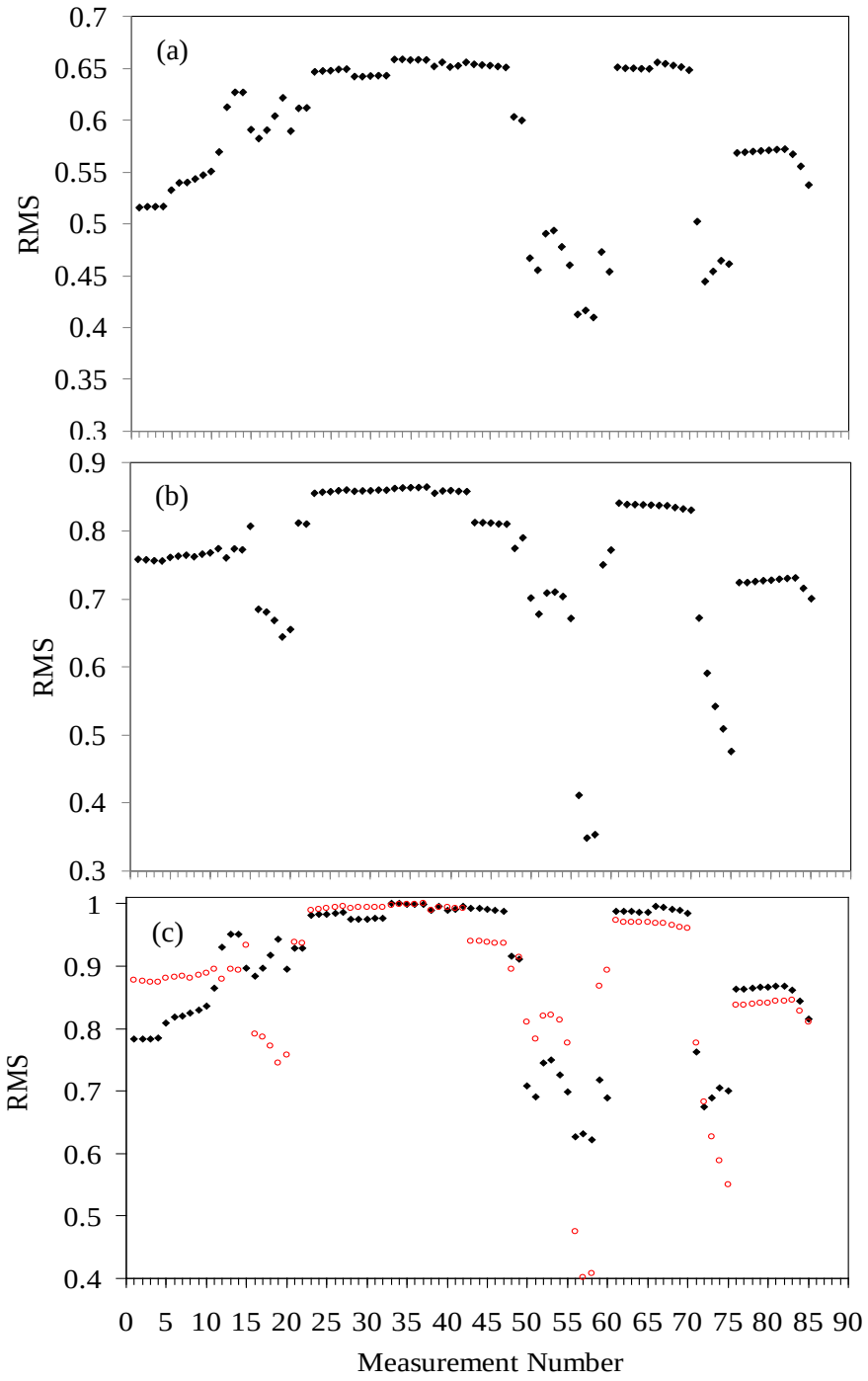

Figure 4.10 – Test 3. RMS for path: (a) S3=>S2; (b) S0=>S1; (c) Normalized RMS for S0=>S1 (red circles) and S3=>S2 (black dots)

Interestingly the effect of the temperature seems to be opposite to that observed in Fig. 4.9. In fact, the temperature decrease determined an increase on the value of the RMS. Across the range 61 – 70 there was not visible variation of the RMS. Along this range the damage state of the notch changed but all other conditions were the same. Across the range 23 – 42 a constant response of the time waveform statistical feature is observed. This range covers absolute temperatures about 2 C (3.6 F) and pristine structure. Surprisingly it seems that the presence of snow does not affect the measurements.

To quantify the effect of the temperature and boundary conditions on the other features considered in this study, Fig. 4.11 is presented. It contains the values normalized with respect to the first measurement of the baseline, which therefore assume a value of 100%. The percentage scale was used to provide a quantitative estimate of the data scattering from the baseline. Figure 4.12 illustrates the results associated with paths S3=>S2 and S0=>S1, for the effect of damage was purposely ignored.

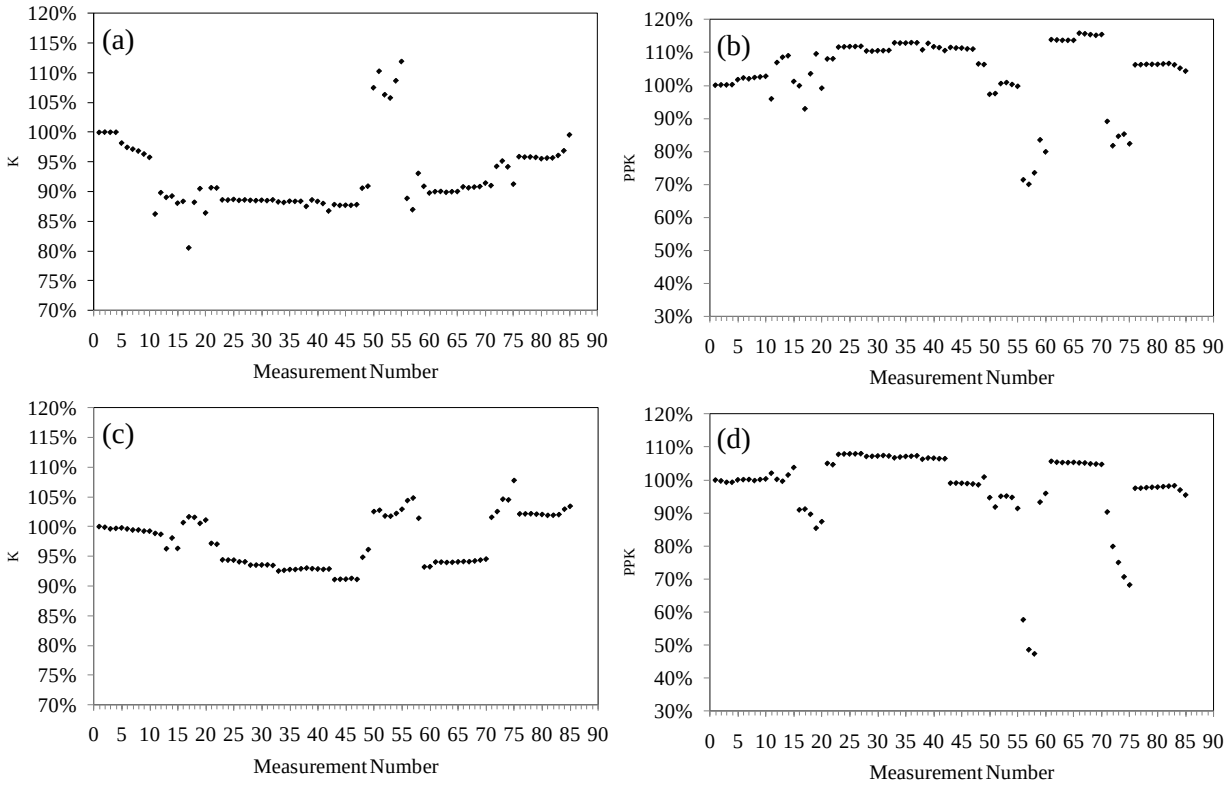

Figure 4.11 – Test 3. Path S3=>S2 (a) K–factor, (b) peak-to-peak. Path S0=>S1 (c) K–factor, (d) peak-to-peak.

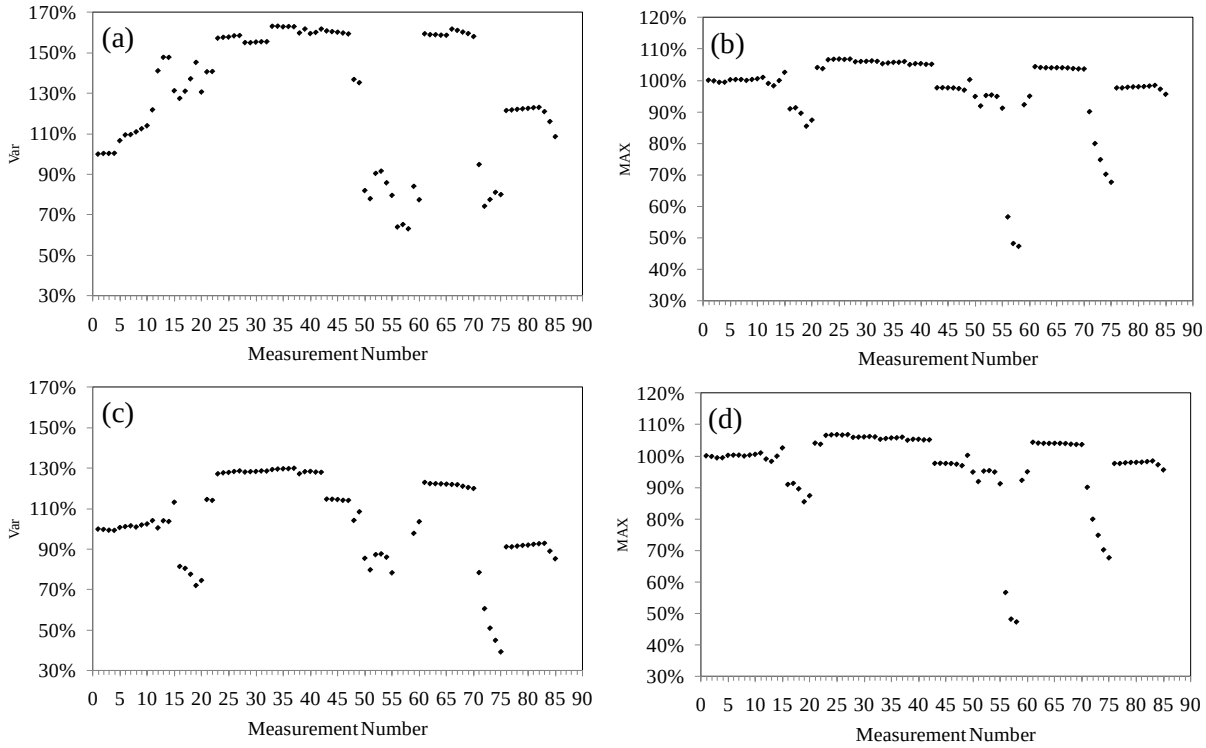

Figure 4.12– Test 3. Path S3=>S2 (a) variance, (b) maximum. Path S0=>S1 (c) variance, (d) maximum.

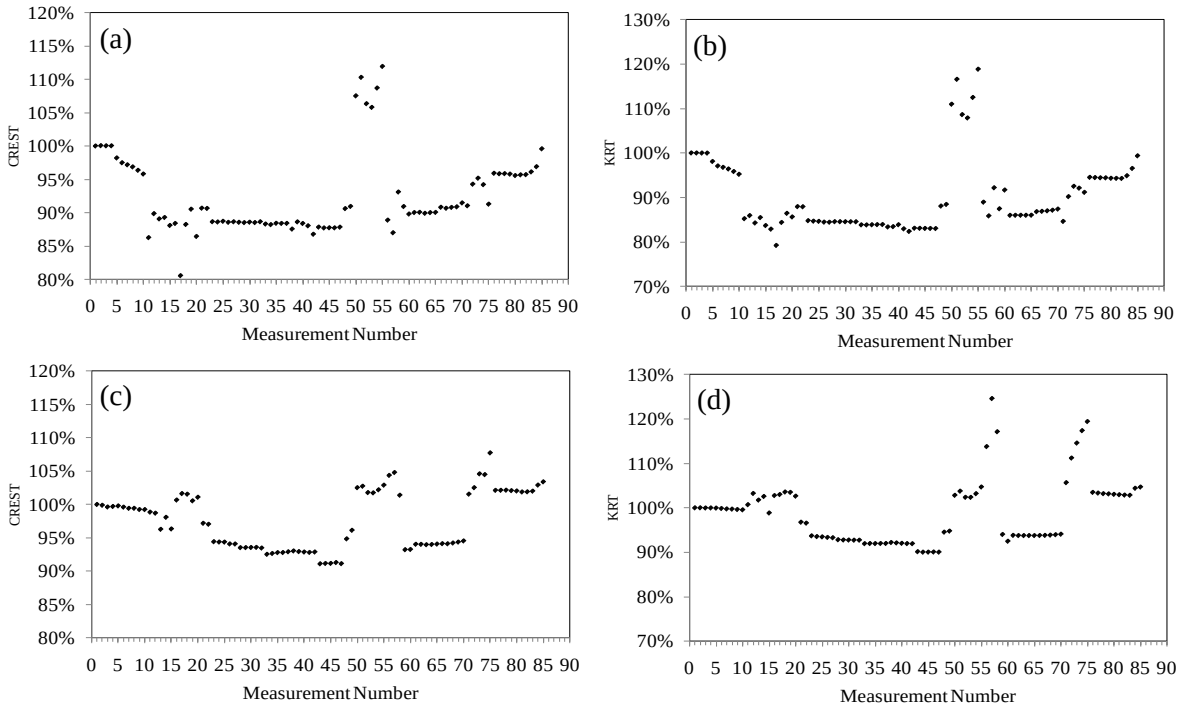

Figure 4.13 – Test 3. Path S3=>S2 (a) crest factor, (b) kurtosis. Path S0=>S1 (c) crest factor, (d) kurtosis.

Overall the trend is similar although by comparing the values on the y-axis, some feature is less sensitive to the temperature variation.

The damage index ratios S3=>S4 /S3=>S2 and S0=>S4 / S0=>S1 associated with six statistical features are presented in Fig. 4.14 (a) and (b), respectively.

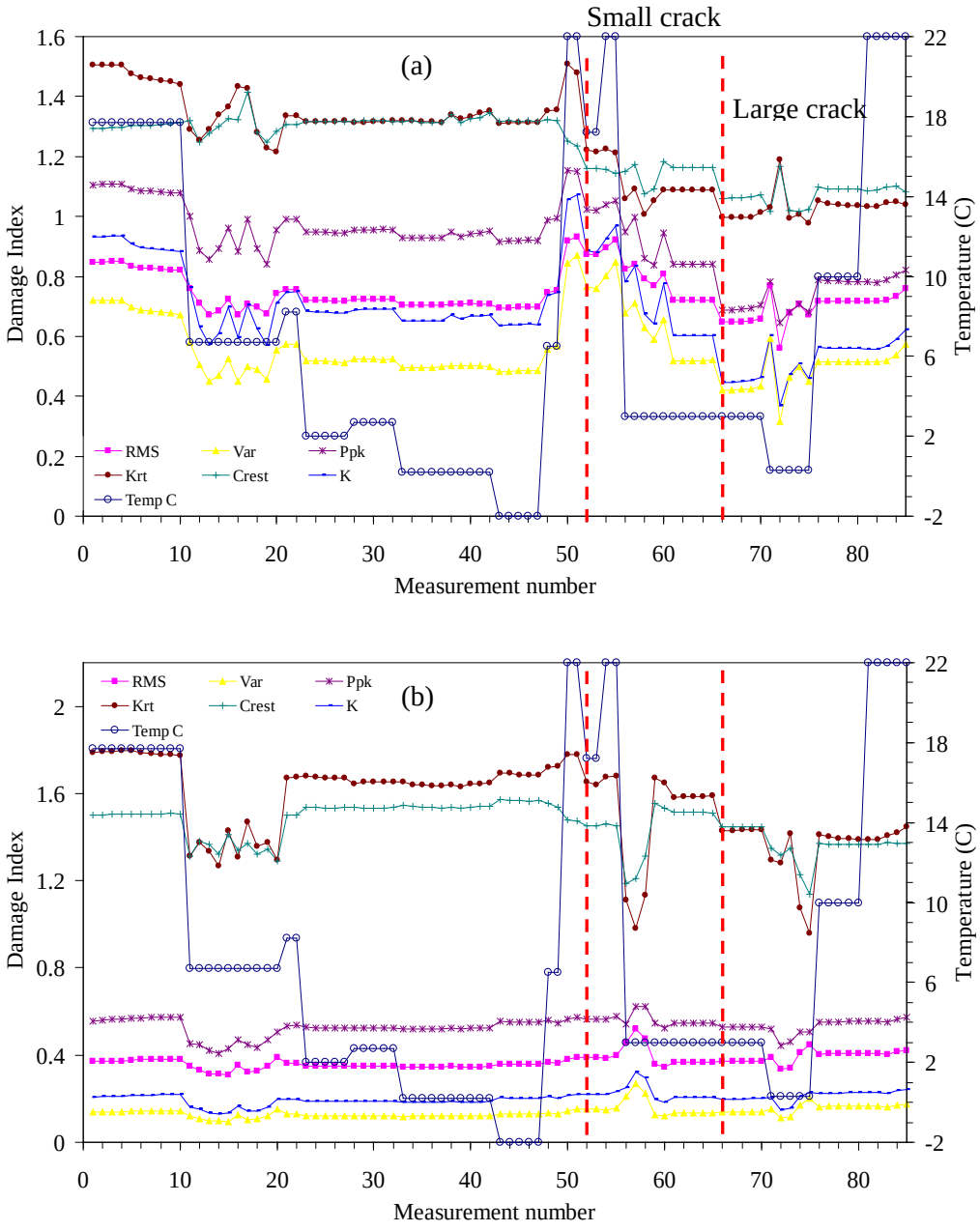

Figure 4.14 – Damage Index as a function of the measurement number associated with six features. (a) Ratio S3=>S4 /S3=>S2. (b) Ratio S0=>S4 / S0=>S1. The value of the temperature at each measurement number is scaled on the y-axis on the right.

The graph of the chord's temperature is overlapped and its values are plotted against the right ordinate axis. The two vertical lines indentify the measurement at which the small crack was devised and when the small crack was enlarged.

In both Fig. 4.14 (a) and (b) there is no clear stepwise behavior associated to the formation of the small crack after measurement 51. However after measurement 65, when the small crack was expanded a step is visible in all six features associated with the damage index ratio S3=>S4 /S3=>S2 which was expected to be affected by the presence of damage.

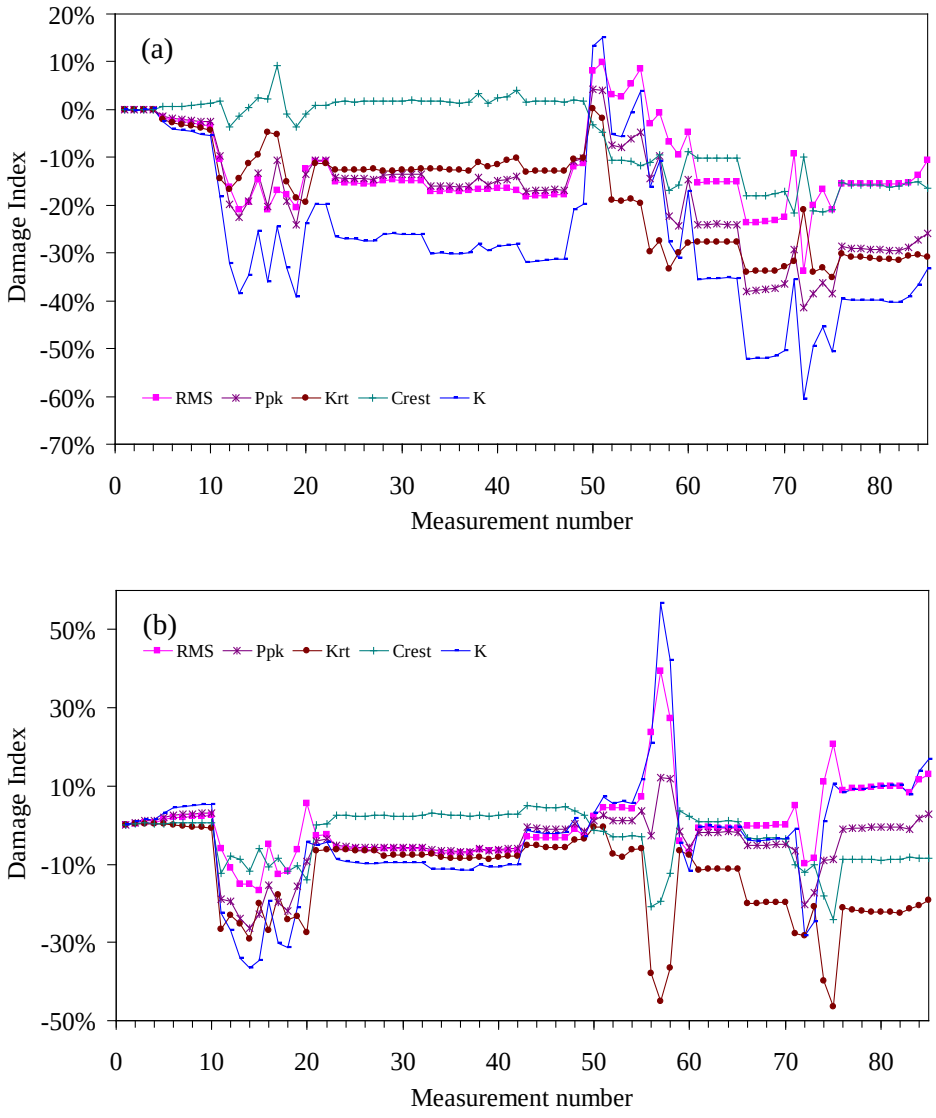

Figure 4.15 – Percentage variation of the damage index as a function of the measurement number associated with six features with respect to the value calculated during the first measurement. (a) Ratio S3=>S4 /S3=>S2. (b) Ratio S0=>S4 / S0=>S1. The value of the temperature at each measurement number is scaled on the y-axis on the right.

A step between measurement 65 and 66 is also visible in the plot of the crest and kurtosis associated with the ratio S0=>S4 / S0=>S1. Such behavior was not expected and could be used to ignore such statistical features from further use.

To quantify the variation in percentage of the damage index with respect to the first measurement Fig. 4.15 are presented. The figures show that the K-factor and the RMS had the largest variation.

The temperature dependency of the results observed in the previous Figures is mainly due to the characteristics of the PZT. A recent work by Lanza di Scalea and Salamone [28] has investigated the effect of temperature on the guided Lamb wave propagation. The temperature-dependent properties of the PZTs are the following: Young's moduli, Poisson's ratios, piezoelectric coefficients; dielectric permittivity; and length and thickness.

Other factors that affected the results are: 1) non-uniform distribution of the temperature when the heat gun was used; 2) variation in size and thickness of the adhesive; 3) variation of the adhesive mechanical properties.

To shed some light on the cause of such a discrepancy associated with the various measurements the time waveforms associated with propagation paths S3=>S2 and S3=>S4 are presented in Fig. 4.16 and 4.17, respectively. The plots refer to measurement number 1, 25, 61, and 68. All these measurements had in common dry conditions.

From Fig. 4.16 it is possible to observe that except for the first arrival at about 110 microseconds, the shape of all the ultrasonic packets is overall similar. As said earlier wave path S3=>S2 was not influenced by the presence of damage. Although wave path S3=>S4 should be affected by the presence of damage, Fig. 4.17 does not show any evident shape/amplitude difference among the four cases presented.

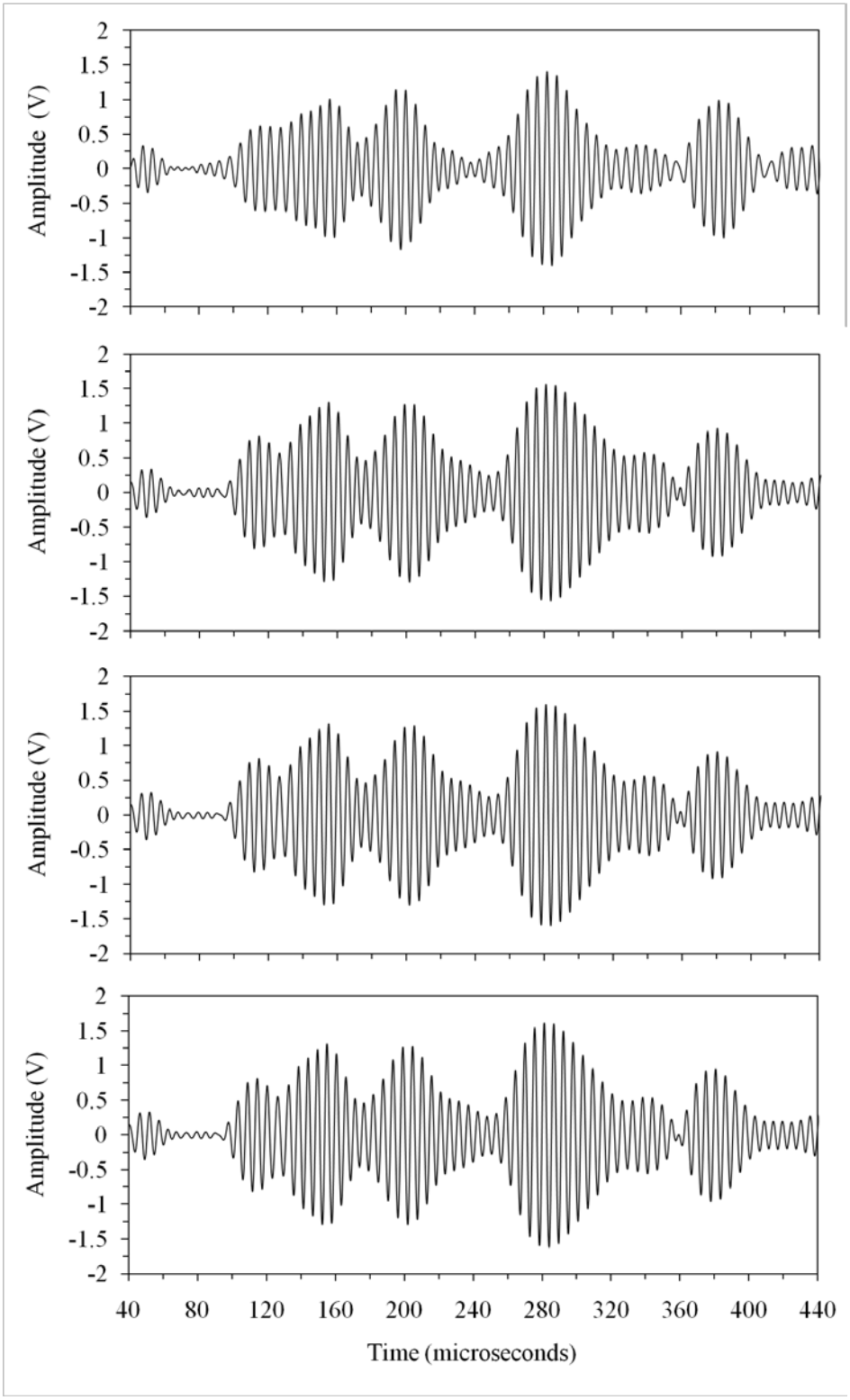

Figure 4.16 – Time waveforms generated by actuator S3 and sensor S2. From top to bottom: measurement number 1. 25. 61, 68.

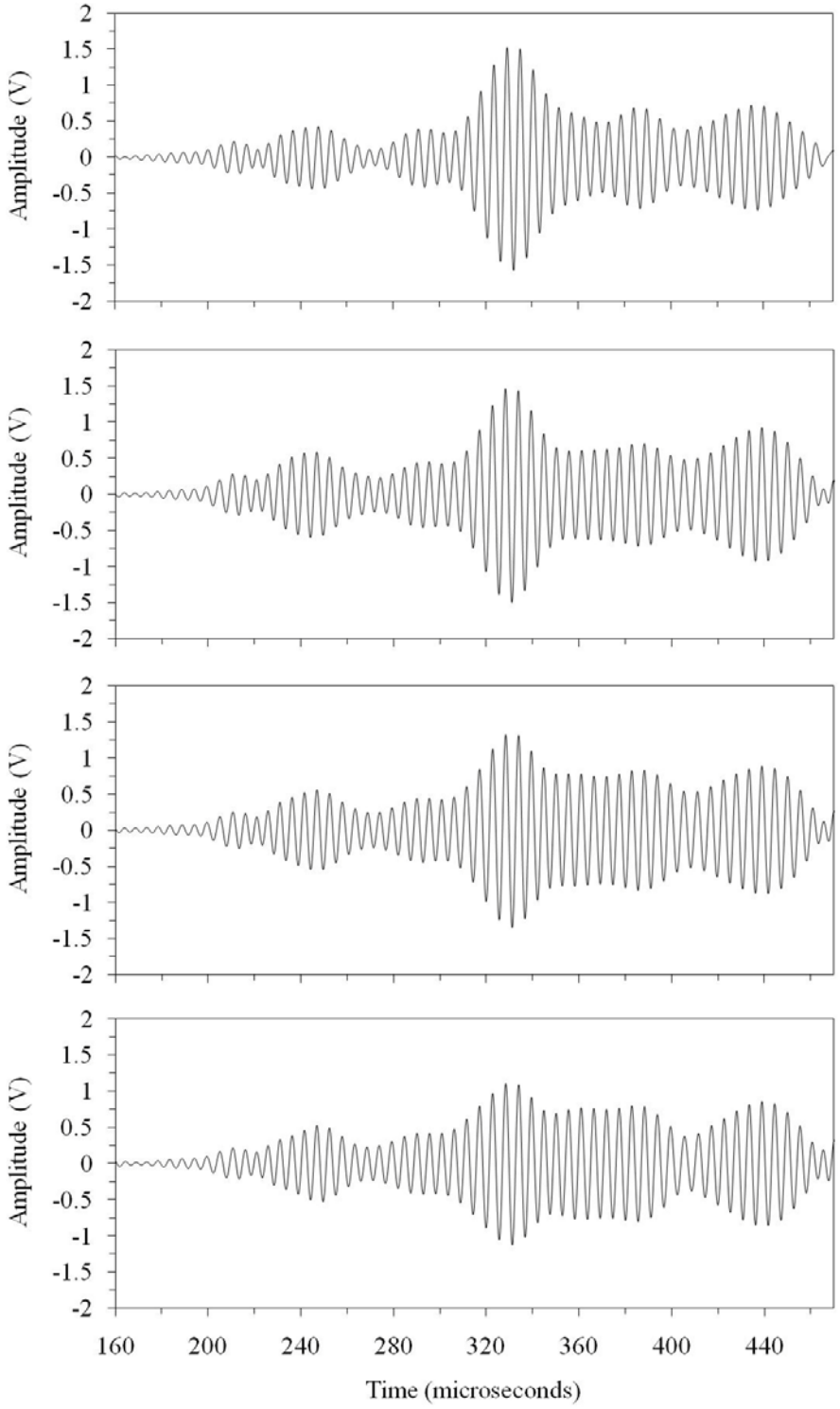

Figure 4.17 – Time waveforms generated by actuator S3 and sensor S4. From top to bottom: measurement number 1. 25. 61, 68.

To complete the analysis of Test 3 the outlier analysis was conducted. The MSD associated with the seven features calculated for four damage index ratios is presented in Fig. 4.18. For this analysis the first ten measurements only were considered for the baseline, and therefore for the computation of the threshold level. Clearly, all data were classified as outliers and there is no evidence that data from damaged state could be discriminated.

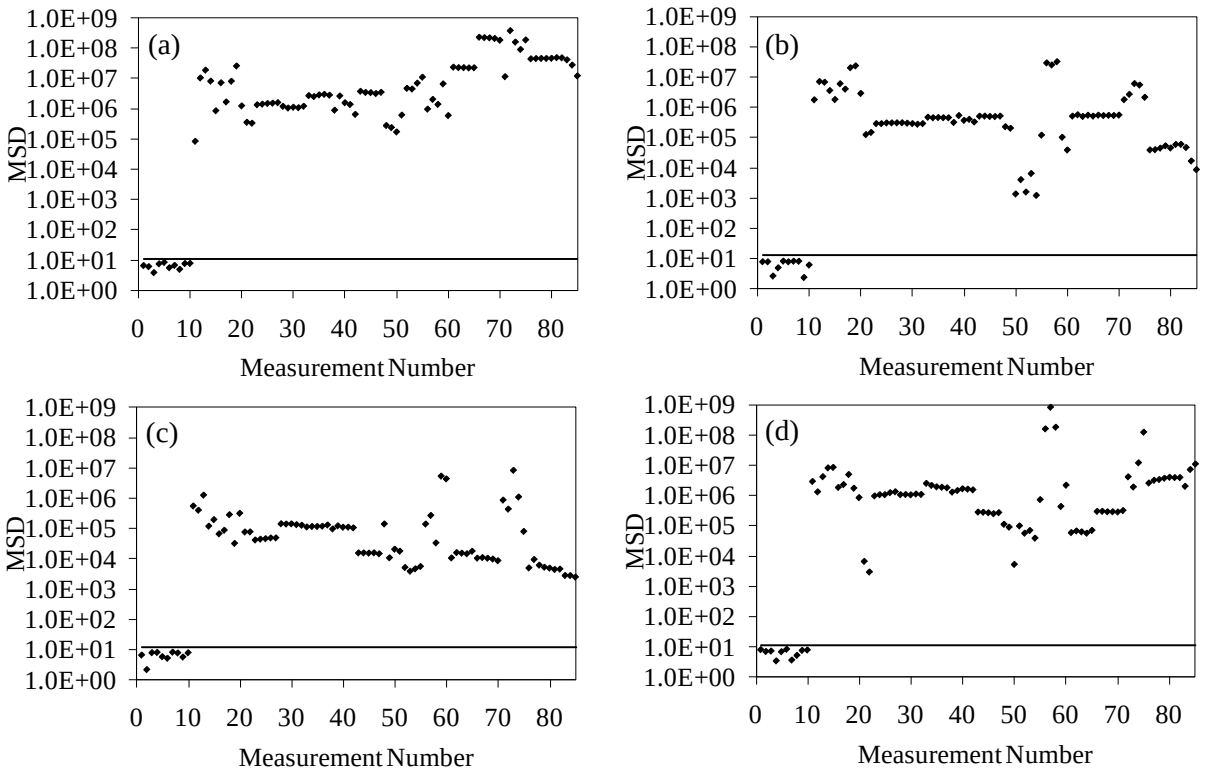

Figure 4.18 - Multivariate analysis. Mahalanobis squared distances as a function of the measurement number considering all 7 features for: (a) S3=>S4/S3=>S2; (b) S3=>S0/S3=>S2; (c) S0=>S3/S0=>S1; (d) S0=>S4/S0=>S1.

As the scope of any outlier analysis applied to ultrasonic-based damage detection strategy is to find structural anomalies, the number baseline data were increase to include the first 51 measurements. The results of this multivariate analysis are presented in Fig. 4.19. Clearly an improvement in the success rate is visible. In fact Fig. 4.19 (a) shows the largest number of outliers. This is expected as the data refers to C3=>C4/C3=>C2, which is affected by the presence of damage. On the contrary, the plot in Fig. 4.19 (d), which is related to the damage index ratio C0=>C4/C0=>C1, shows few outliers.

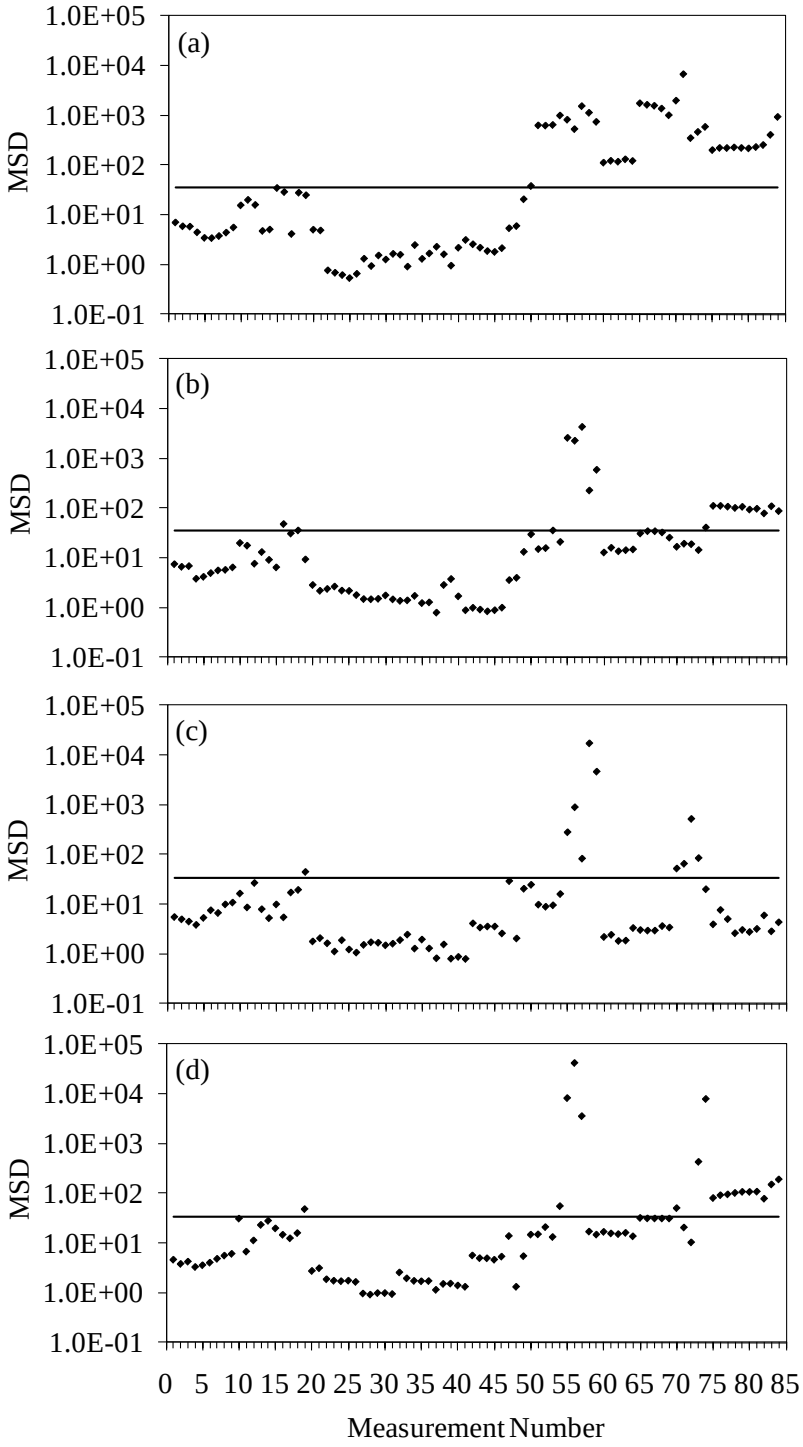

Figure 4.19 – MSD as a function of measurement number for paths (a) C3=>C4/C3=>C2, (b) C3=>C0/C3=>C2, (c) C0=>C3/C0=>C1, and (d) C0=>C4/C0=>C1. The first 51 measurements were considered as baseline.

5.0 EXPERIMENTAL RESULTS FROM EMI

5.1 LOW-COST CIRCUITRY

To conduct the EMI measurements by means of the portable NI-PXI, a low cost electric circuit was designed. The aim was to develop a low-cost system that would not require the use of a conventional impedance analyzer or LCR meter.

According to the scheme illustrated in Fig. 5.1 the output of the function generator was connected to the circuit consisting of a PZT and a resistor. The nodes of the circuit were also connected to the PXI digitizer. The LabView program illustrated in Fig. 3.6 (b) and (c) controlled the generation of an 1-Volt amplitude, 50-cycles sinusoidal wave. The sine wave frequency was driven from 100 KHz to 500 KHz with 0.5 KHz step.

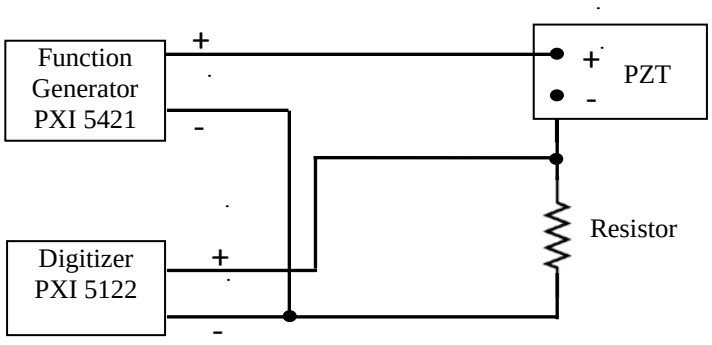

Figure 5.1 – Design of the circuit and its connection to the PXI for EMI measurement

Once the digitizer collected the output waveform V_o from the resistor, the calculation of the PZT admittance Y(j) was executed by applying the following equations:

$$Y(j\omega)=\frac{1}{R_s}\cdot\frac{u_o(j\omega)}{u_i(j\omega)-u_o(j\omega)}=\frac{1}{R_s}\cdot\frac{V_o e^{j(\omega t+\beta)}}{V_i e^{j\omega t}-V_o e^{j(\omega t+\beta)}}$$

$$=\frac{1}{R_s}\cdot\frac{V_o\angle\beta}{V_i\angle 0-V_o\angle\beta}=\frac{V_o}{R_s}\cdot\frac{\cos\beta+j\sin\beta}{V_i-V_o\cos\beta-jV_o\sin\beta}$$

$$=\frac{V_o}{R_s\cdot\sqrt{(V_i-V_o\cos\beta)^2+(V_o\sin\beta)^2}}\cdot\frac{\angle\beta}{\angle arc\tan(-\frac{V_o\sin\beta}{V_i-V_o\cos\beta})}$$

$$=\frac{V_o}{R_s\cdot\sqrt{(V_i-V_o\cos\beta)^2+(V_o\sin\beta)^2}}\cdot\angle(\beta-arc\tan(-\frac{V_o\sin\beta}{V_i-V_o\cos\beta}))$$

$$=M\cdot\cos\alpha-jM\cdot\sin\alpha \qquad (5.1)$$

, where is the admittance, u_i and u_o are the input and output signals, respectively, V_i and V_o are the amplitude of the input and output signals, R_s is the value of resistance and β is the phase shift between the input signal and output signal, $j^2=-1$, ω is the angular frequency.

In Eq. 5.1, M and α are defined as:

$$\alpha=\beta-arc\tan(-\frac{V_o\sin\beta}{V_i-V_o\cos\beta}),M=\frac{V_o}{R_s\cdot\sqrt{(V_i-V_o\cos\beta)^2+(V_o\sin\beta)^2}} \qquad (5.2)$$

To assess the performance of this circuit, a comparative study between the Labview program combined with the designed circuit and a commercial LCR meter was conducted. The EMI signatures of a PZT were measured by both methods and the results are shown in Fig. 5.2. Fig. 5.2 (a) and (b) present the conductance and the susceptance, respectively, as a function of frequency associated with the PZT. The results from different measurements of the designed circuit are presented in Fig. 5.2 (c) and (d). By observing these figures it is evident that the PXI system is capable to identify the main peaks for both conductance and susceptance and it agrees very well with the results obtained with the LCR meter. And the repeatability is sufficient for the deviation analysis. The differences could be resulted from the impedance introduced by NI PXI and the switch module. In the mean while, the conductance became coarse and 'noisy' at higher frequency.

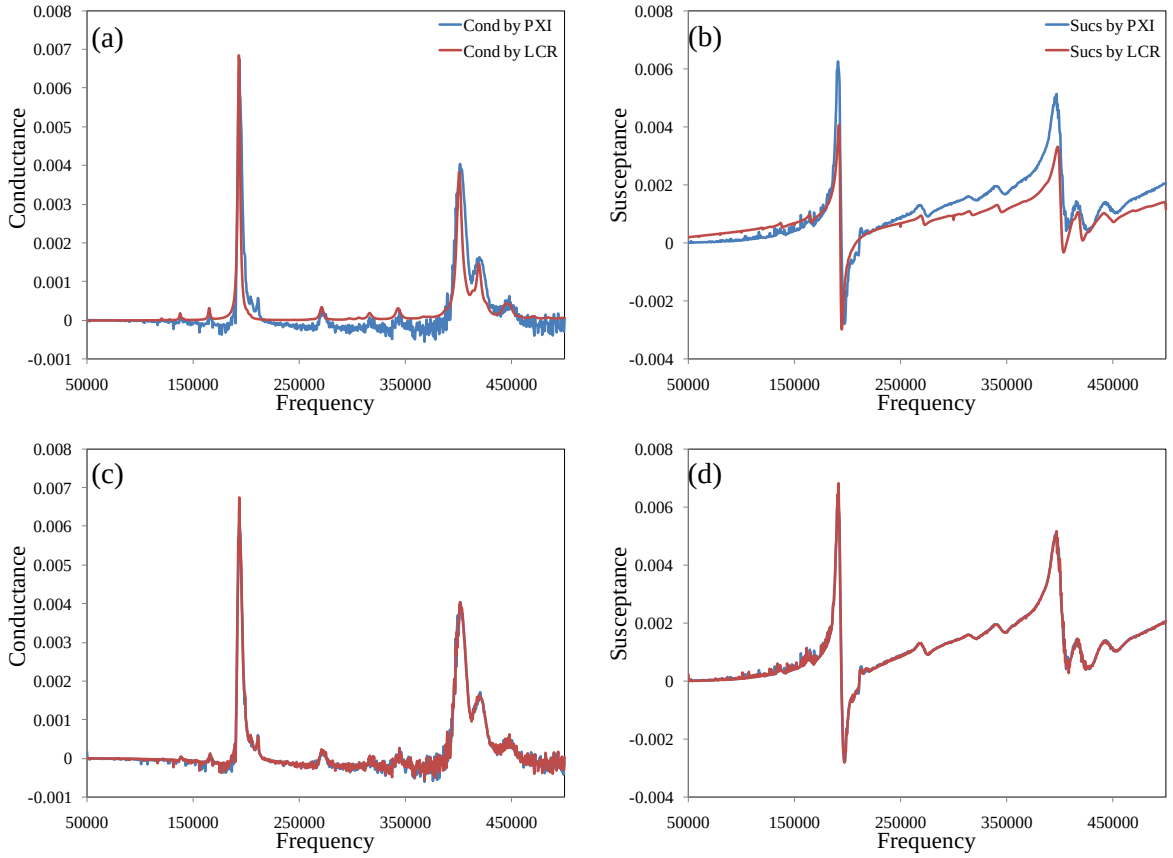

Figure 5.2 – Comparative study between LCR and low-cost circuit conducted on PZT. Results from PXI and LCR meter for (a) Conductance and (b) Susceptance as a function of frequency; Results from PXI of different measurements for (c) Conductance and (d) Susceptance as a function of frequency.

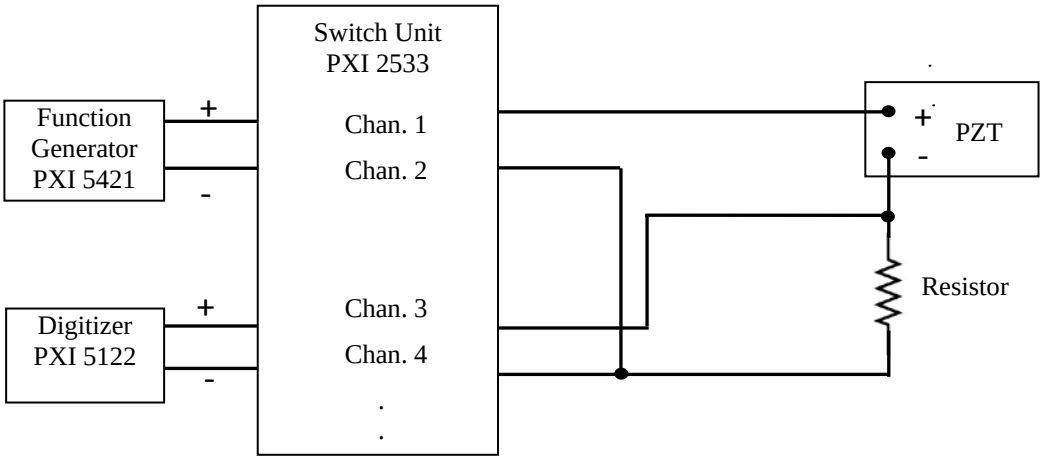

Figure 5.3 - Design of the circuit and its connection to the PXI and the switch for multiple EMI measurement

As for the structure many PZT were potentially used, the low cost circuit had to be integrated with the PXI switch unit. The function generator output was connected to the switch unit according to the scheme illustrated in Fig. 5.3.

A photo of the hardware system is presented in Fig. 5.4.

Fig. 5.5 illustrates the connection setup for the EMI measurement coupled with PXI: in Fig. 5.3 (a), high-density matrix switch module PXI-2532 is directly connected with the front-mounting terminal block TB-2643, and the SCB-264X terminal block provides screw terminal access to the row and column connections of the PXI-2532 switch via an NI TB-264x terminal; the physically connection scheme in the screw terminal for the situation in Fig. 5.2 is shown in Fig. 5.3 (b). The PZTs and the circuit interact with the screw terminals and the channel switching is controlled by the LabView program and the topology for specified switch module.

The program was designed to control as many as 16 different PZTs by using the connection topology illustrated in Fig. 5.4. In this topology r0 and r1 are the positive and negative output of the PXI digitizer, respectively, and r2 and r3 are the positive and negative output of the PXI function generator, respectively. In the topology c0, …, c63 denominates the terminals of the PXI switch unit. In this particular experiment, for instance, c0…, c3 serve to connect EM1 to the PXI following the scheme illustrated in Fig. 5.2. The LabView program designed for the EMI measurement, and illustrated in Fig. 3.6 (d) and (e), relayed the driving signal from the function generator to the proper EMI sensor.

To further validate the proposed measurement system, the admittance signatures from one of the PZTs bonded to the truss structure, namely EM1, was measured by both methods. The results are shown in Fig. 5.6. Overall the agreement is satisfactorily.

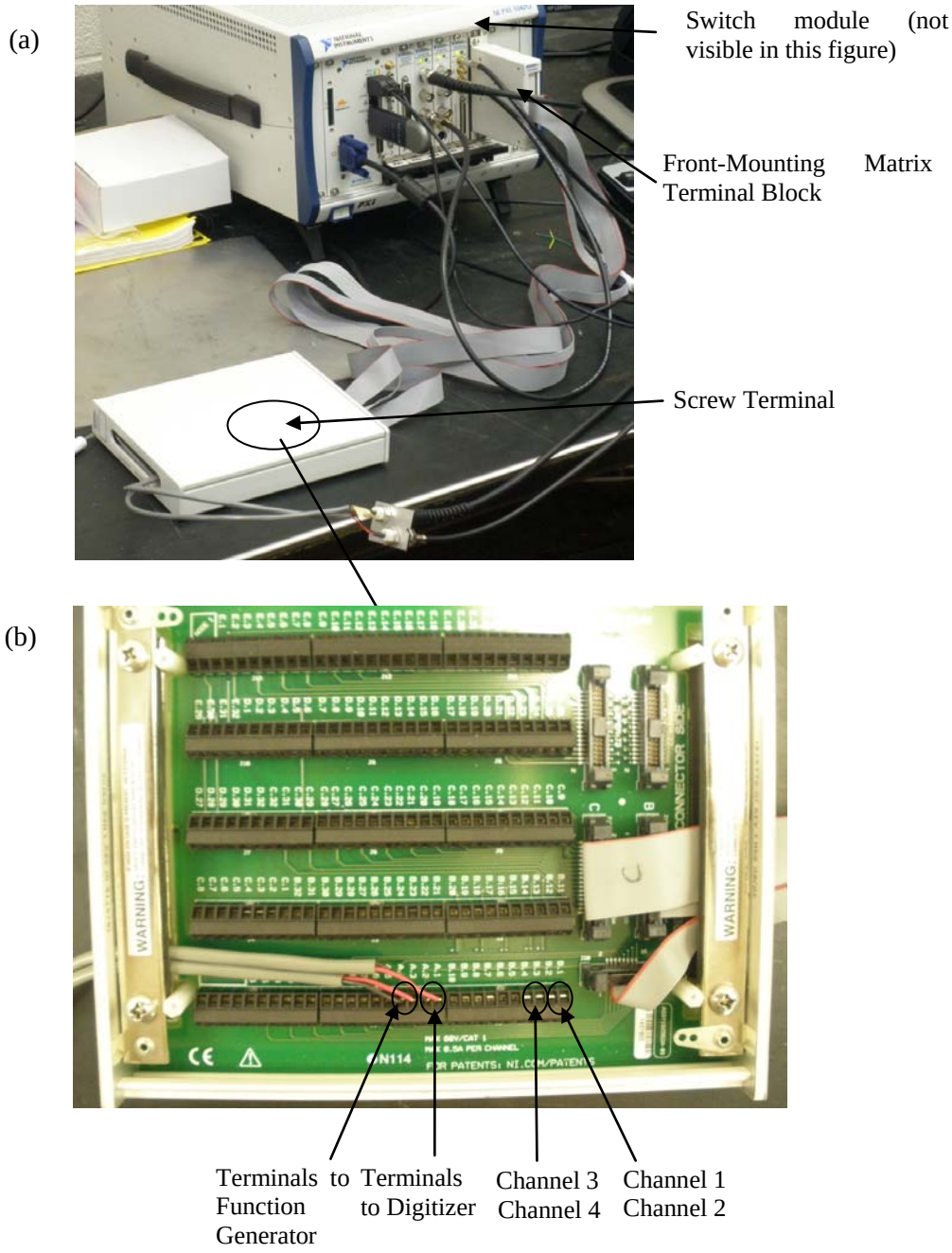

Figure 5.4 – Hardware for the EMI measurement. (a) PXI, switch module, terminal block and screw terminal. (b) Inside view of the screw terminal.

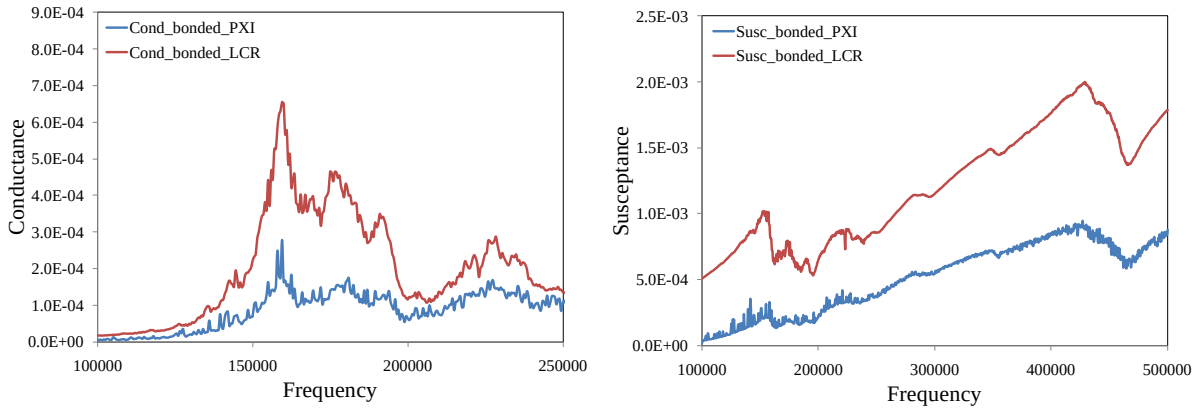

Figure 5.5 - (a) Conductance resulted from PXI and LCR meter for EM1 bonded with the truss structure; (b) Susceptance resulted from PXI and LCR meter for EM1 bonded with the truss structure.

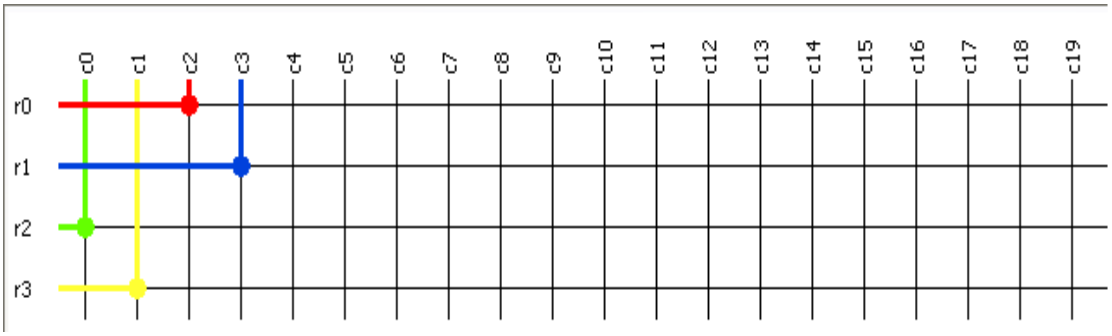

Figure 5.6- Connection topology adopted for the NI Switch front panel and first PZT.

5.2 EMI-RELATED SIGNAL PROCESSING ALGORITHM

The overall SHM algorithm implemented in this study for the EMI study is illustrated in the flowchart in Fig. 5.7.

The first step consisted on the measurement of the conductance signatures. Examples of signatures acquired from EM1 and EM2 at different cycle number and focused in the frequency

range 100 – 250 kHz are shown in Fig. 5.8. The figures show that as the crack increased, there was a shift of the conductance peak.

From each conductance signature (conductance as a function of frequency) the features of the variance, RMS, max amplitude, kurtosis, and skewness were calculated. Moreover, the area under the signature and the RMS deviation (RMSD) were computed as well. The RMSD is defined as:

$$\mathrm{RMSD}(\%) = \sqrt{\frac{\sum_{i=1}^{N}(y_i^k - y_i^1)^2}{\sum_{i=1}^{N}(y_i^1)^2}} \times 100 \qquad (5.3)$$

, where y_i^k , y_i^1 are respectively k-th and baseline state admittance at a frequency i, N represents the upper limit (i.e. in a range comprising of N frequencies) and $\overline{y^k}$ is the mean of the admittances obtained at k-th state for N frequencies. This feature compares the quantitative deviation of the k-th measurement with the baseline signature. The RMSD as a function of the cycle number associated to the measurements conducted with EM1 and EM2 in the frequency range 100 - 500 KHz are shown in Fig. 5.9.

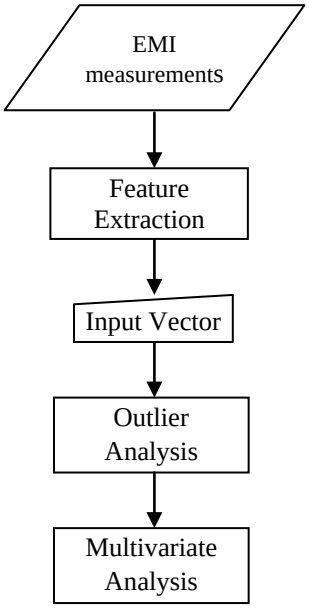

Figure 5.7 - Flowchart of the defect detection procedure

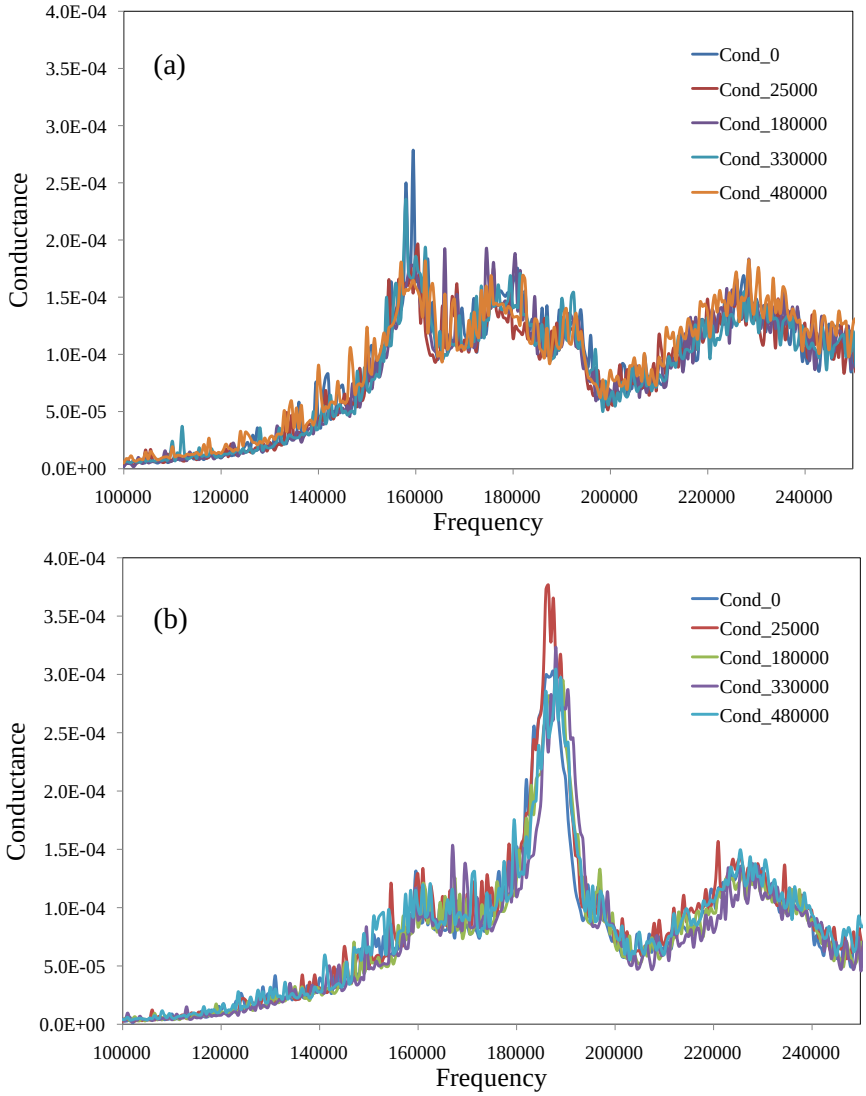

Figure 5.8 - (a) Conductance signature for EM1 resulted from PXI at 5 different periods; (b) Conductance signature for EM2 resulted from PXI at 5 different periods.

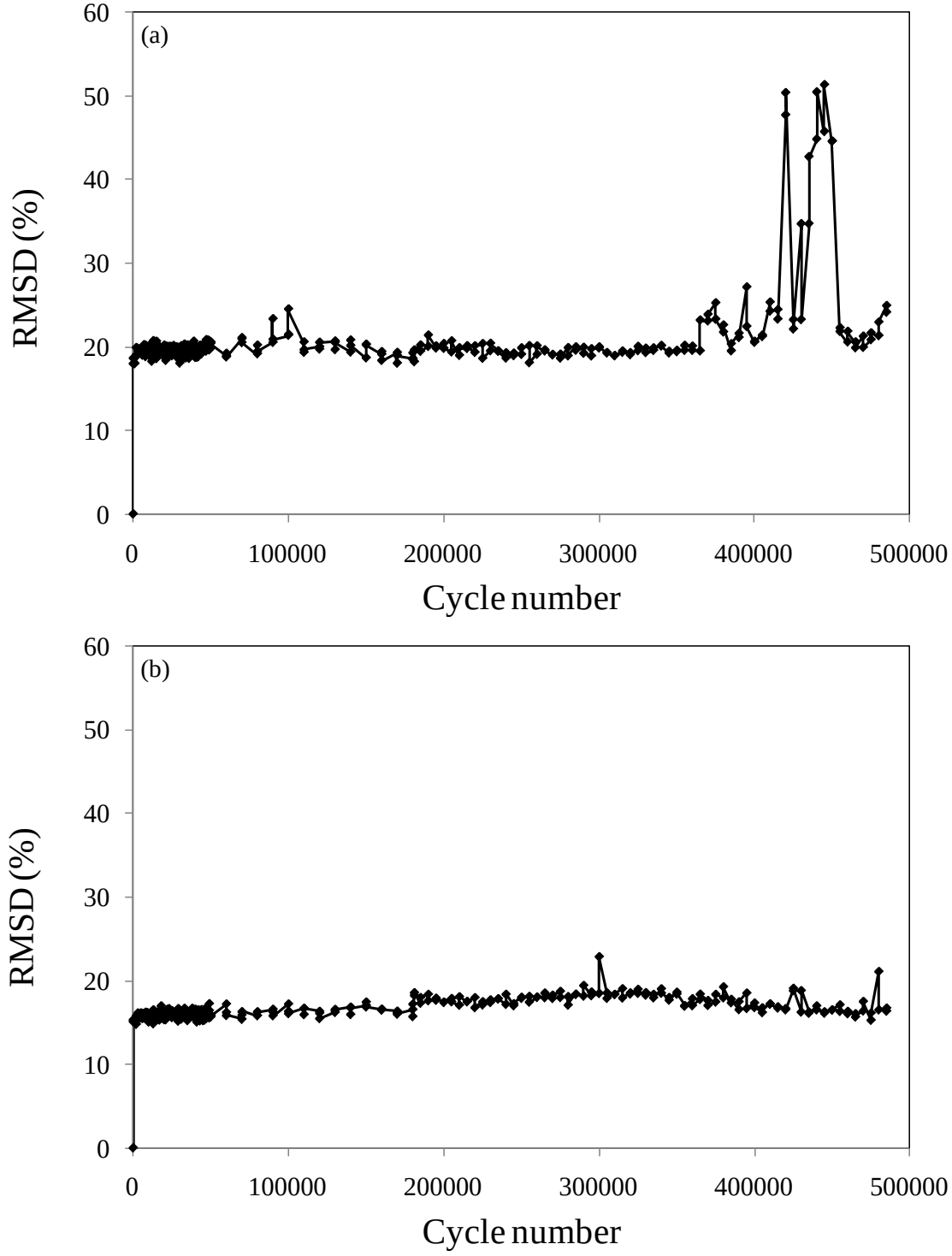

Figure 5.9 - RMSD values from 100 KHz to 500 KHz of (a) EM1; (b) EM2

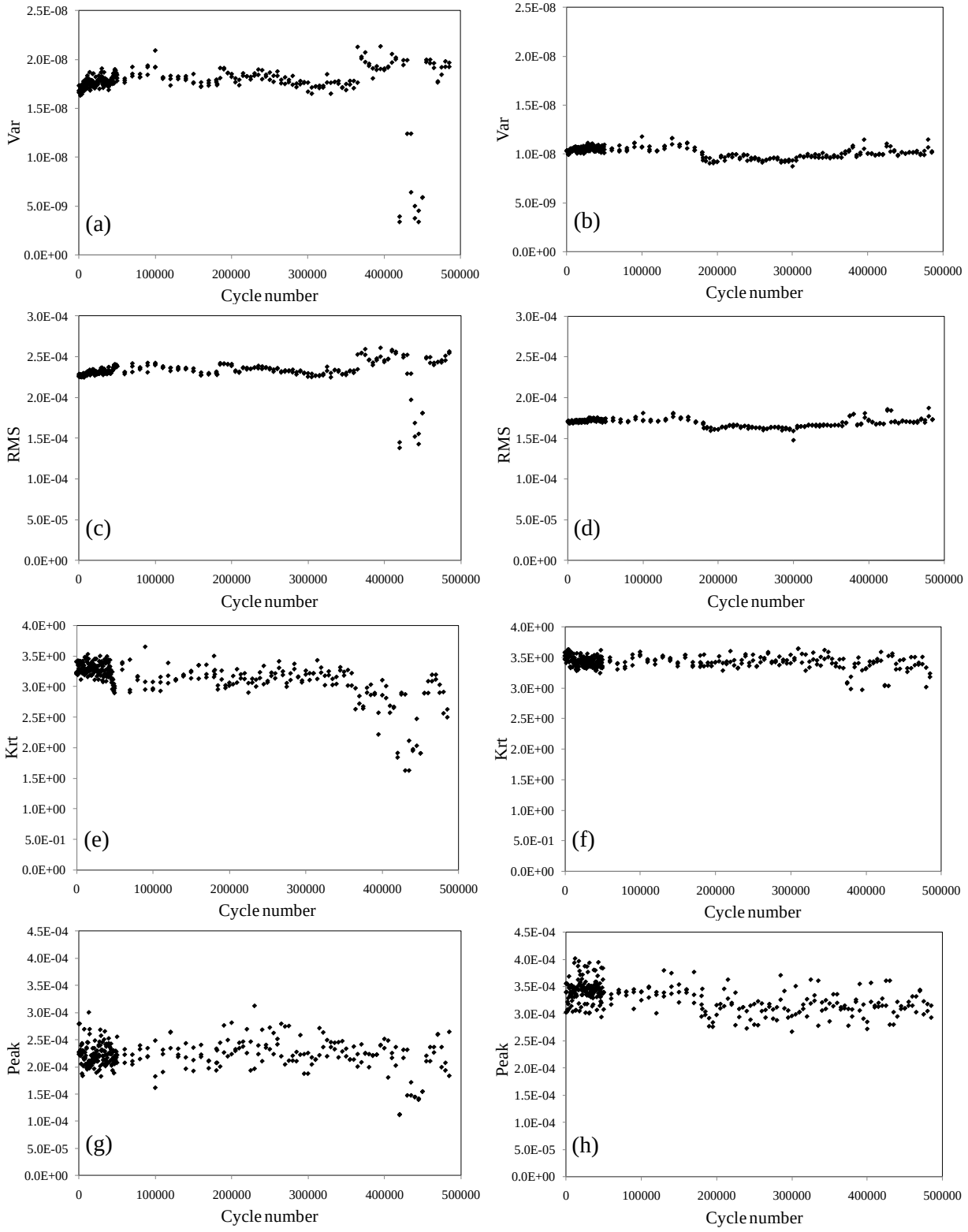
Var
Cycle number
(a)
(b)
RMS
(c)
(d)
Krt
(e)
(f)
Peak
(g)
(h)

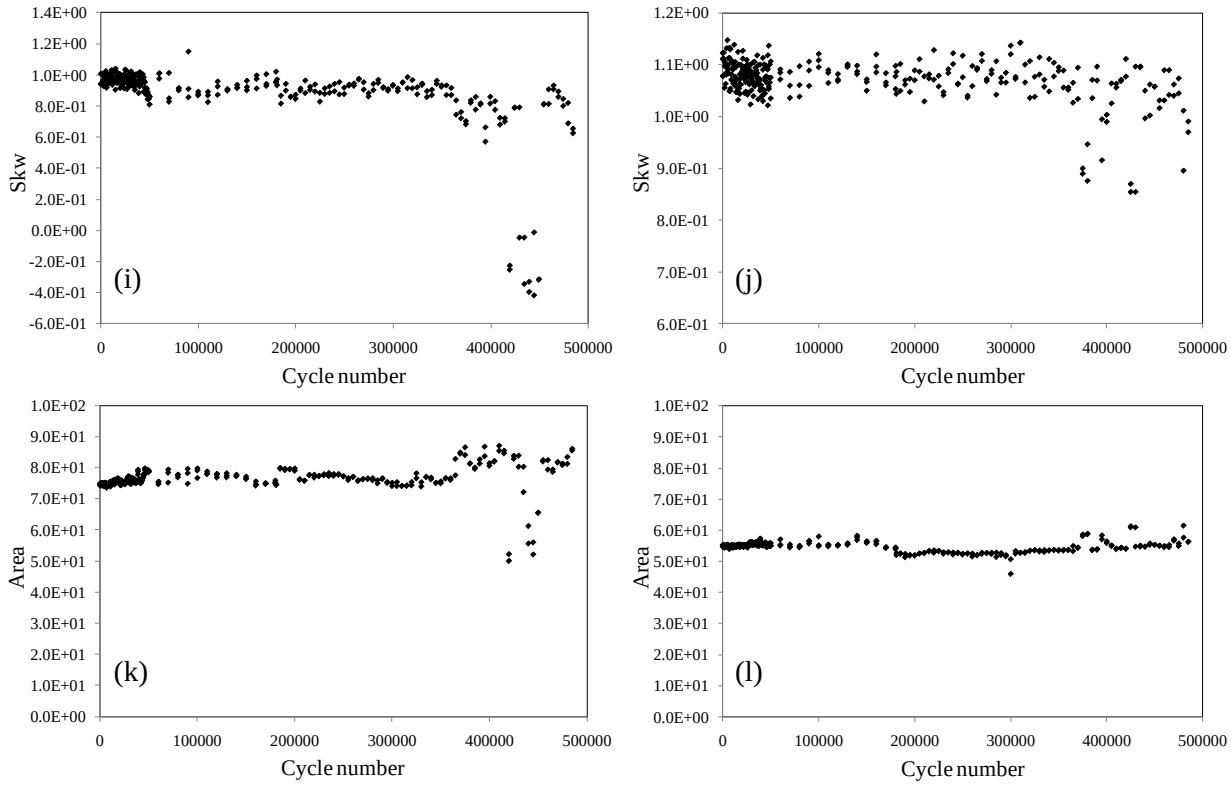

Figure 5.10 - Statistical features as a function of the loading number of cycles. (a) Var EM1; (b) Var EM2; (c) RMS EM1; (d) RMS EM2; (e) Krt EM1; (f) Krt EM2; (g) Peak EM1; (h) Peak EM2; (i) Skw EM2; (j) Skw EM1; (k) Area EM2; (l) Area EM1.

Fig. 5.10 shows the values of the remaining features as a function of the cycle number. The plots on the left column are associated with EM1 while the plots on the right column are associated with transducer EM2. When compared with the performance of the ultrasonic measurement, both Fig. 5.9 and 5.10 do not reveal significant patterns that relate the features to the presence of damage.

In Fig. 5.10 there are some scattered values of the features associated with PZT EM1 around 420,000 cycles. This is due to a sudden decrease in value of the conductance at its peak frequency at about 190 kHz (see Fig. 5.8). It should be noted, when observing Figs. 5.6 and 5.7 that overall no significant difference exists between data obtained from static loading and dynamic loading. This demonstrates that the dynamic loading applied to the truss structure does not affect the EMI measurement

The last step of the signal processing algorithm consisted on applying the multivariate outlier analysis, by combining the seven features discussed above. The “exclusive” MSD for each of the 316 measurements was calculated using Eq. 3.3.

5.3 EXPERIMENTAL RESULTS: LABORATORY TEST

In the multivariate analysis all of the features discussed in the previous section were considered. All combinations of two-dimensional vectors (i.e. vectors containing two out of seven features) up to the single combination of the 7-dimensional vector. Thus, 120 features’ combinations were examined. Data from EM1 and EM2 were considered.

To determine the threshold, the data from the first 18 measurements (0 – 5,000 cycles) were considered.

Fig. 5.11 (a) and (b) show the MSD associated with the 7-dimensional vector as a function of the cycle number PZTs EM1 and EM2, respectively. The improvement of the sensitivity is visible as a very large number of outliers were detected. However, it should be noted that the MSD does not show a step-wise trend as the size of the crack increased with the increase of the number of cycles.

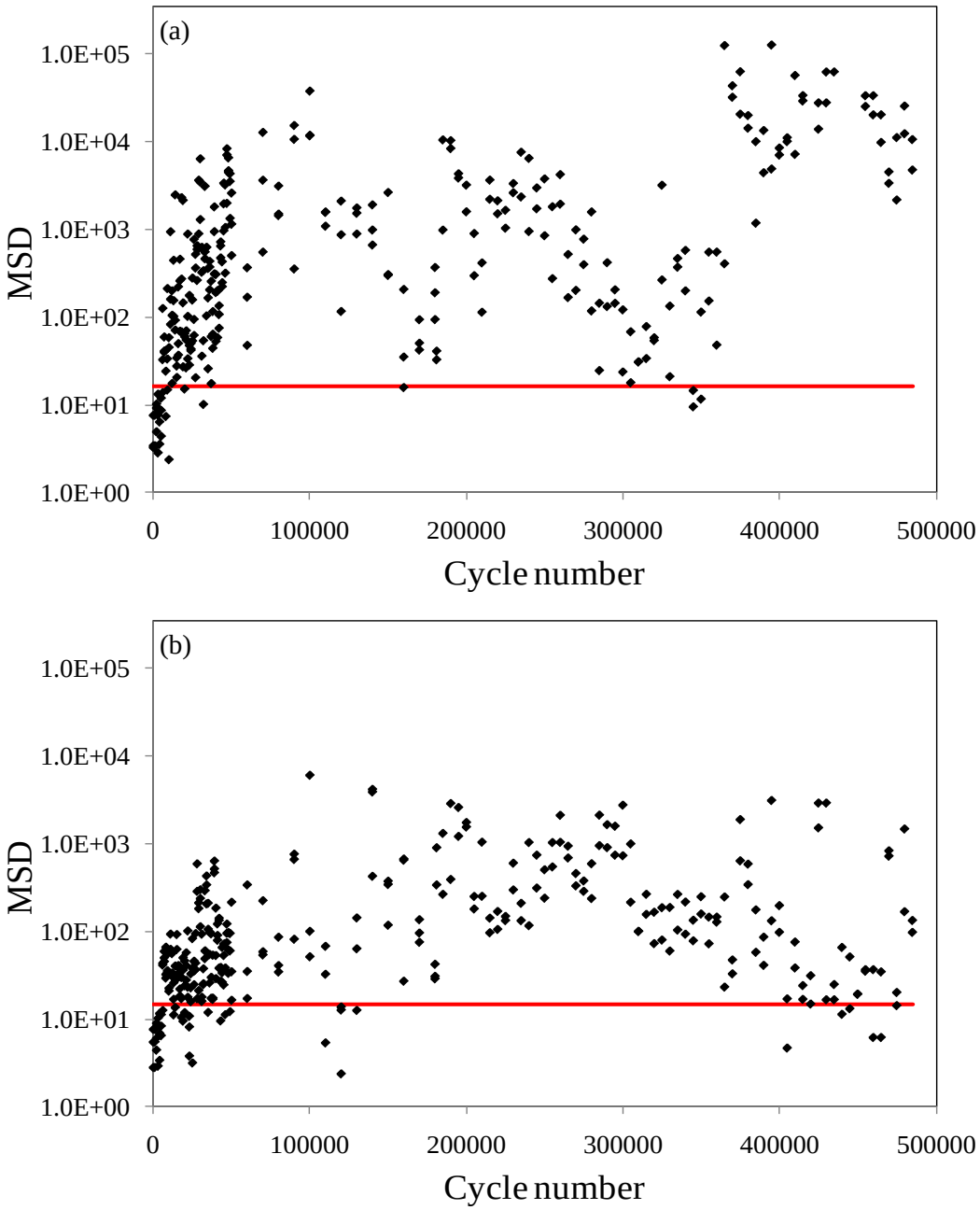

Figure 5.11 - Multivariate analysis. Mahalanobis squared distances as a function of the cycle number considering all seven features for: (a) EM1; (b) EM2.

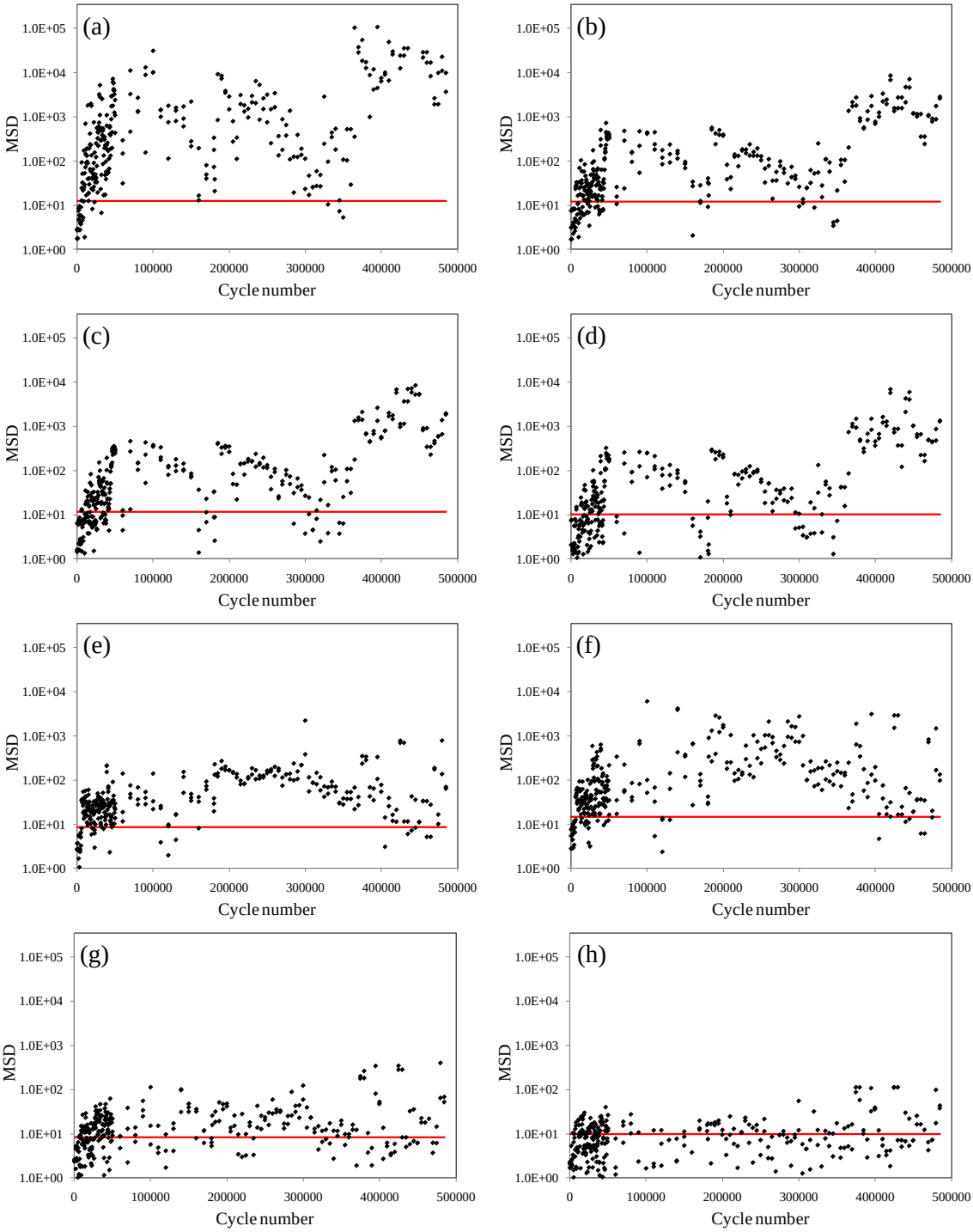

Figure 5.12 - Multivariate analysis. Mahalanobis squared distances as a function of the cycle number for: (a) EM1 with krt, rms, peak, area, skw, var and rmsd (b) EM1 with krt, peak, area, var and rmsd (c) EM1 with krt, rms, peak and skw (d) EM1 with peak, area and rmsd; (e) EM2 with rms, peak, area and skw; (f) EM2 with krt, rms, peak, area, skw, var and rmsd;(g) EM2 with peak, skw and var ; (h) EM2 with peak, area and rmsd.

As conducted for the ultrasonic measurement a parametric analysis was carried out to investigate the feature combination that better performed in terms of damage detection sensitivity. To find empirically the best feature combination in terms of crack detection, a quantitative study was performed using the values of the MSD associated with the 240 cases. The combinations were ranked according to the percentage of outliers properly detected. Fig. 5.12 shows the results associated with the Mahalanobis squared distances as a function of the cycle number for: (a) EM1 with krt, RMS, peak, area, skw, var and RMSD (96.6%) (b) EM1 with krt, peak, area, var and RMSD (86.5%) (c) EM1 with krt, RMS, peak and skw (78.1%) (d) EM1 with peak, area and RMSd; (68.4%) (e) EM2 with RMS, peak, area and skw (93.2%) (f) EM2 with krt, RMS, peak, area, skw, var and RMSD (85.9%) (g) EM2 with peak, skw and var (66.4%) (h) EM2 with peak, area and RMSD (41.6%) from the best to the worst combination cases. Therefore the combination ranked '1st' provided the largest number (96.6%) of outliers and it is shown in Fig 5.12 (a). It is the result of combining all seven features obtained from EM1. At the opposite, the worst combination provided only 33.21% of the outliers properly identified.

6.0 FIELD TEST

6.1 TEST 1: SETUP

The first series of field test was performed on the sign support structure shown in Fig. 6.1 (a). The structure is located along the Mc Knight Road ramp of Interstate 279 (40.49153,-80.009442) few miles north of downtown Pittsburgh. The structure is denoted as L.R.1021 3-C and its information was specified in Appendix B. The main chords consist of tubular elements having HSS 6.625x0.432. Diagonal angular members (ST 2.0x3.850) were welded to the structure. A zoom in view of one of these welded connections is shown in Fig. 6.1 (b).

The sensing system was deployed along the bottom chord on the rear side with respect to the traffic direction (Fig.6.2 (a)). Eight PZTs were bonded to the structure along the part of the chord lying above the shoulder (Fig. 6.2 (b)). The choice of the sensors' location was such that during the installation the closure of traffic lanes was not necessary. Six PZTs in shear modes were used for the generation and detection of UGW.

(a)

(b)

Figure 6.1 – (a) Photo of the structure monitored in the field. (b) particular of the welded connections

(a)

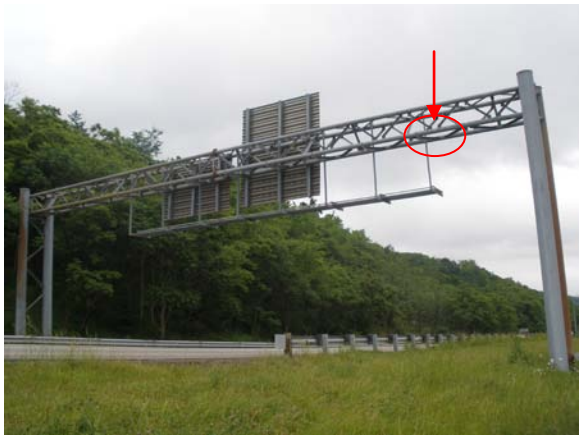

(b)

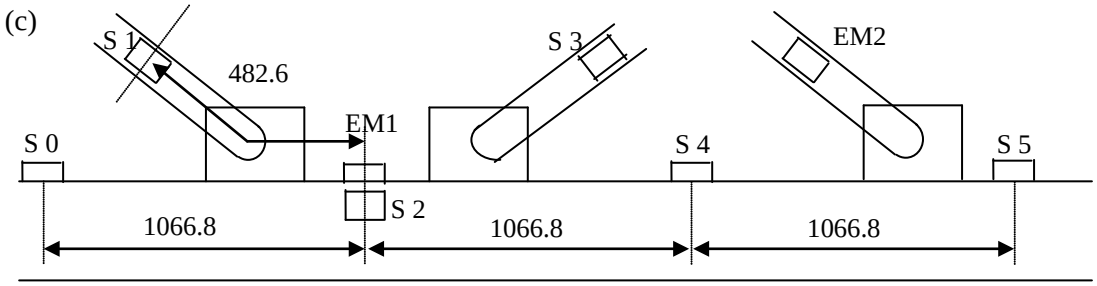

Figure 6.2 (a) Photo of the structure. (b) Close-up view of the part that was monitored. (c) Location of the sensing system. The red circles and arrow show the joints involved in the field test. Distances are expressed in mm.

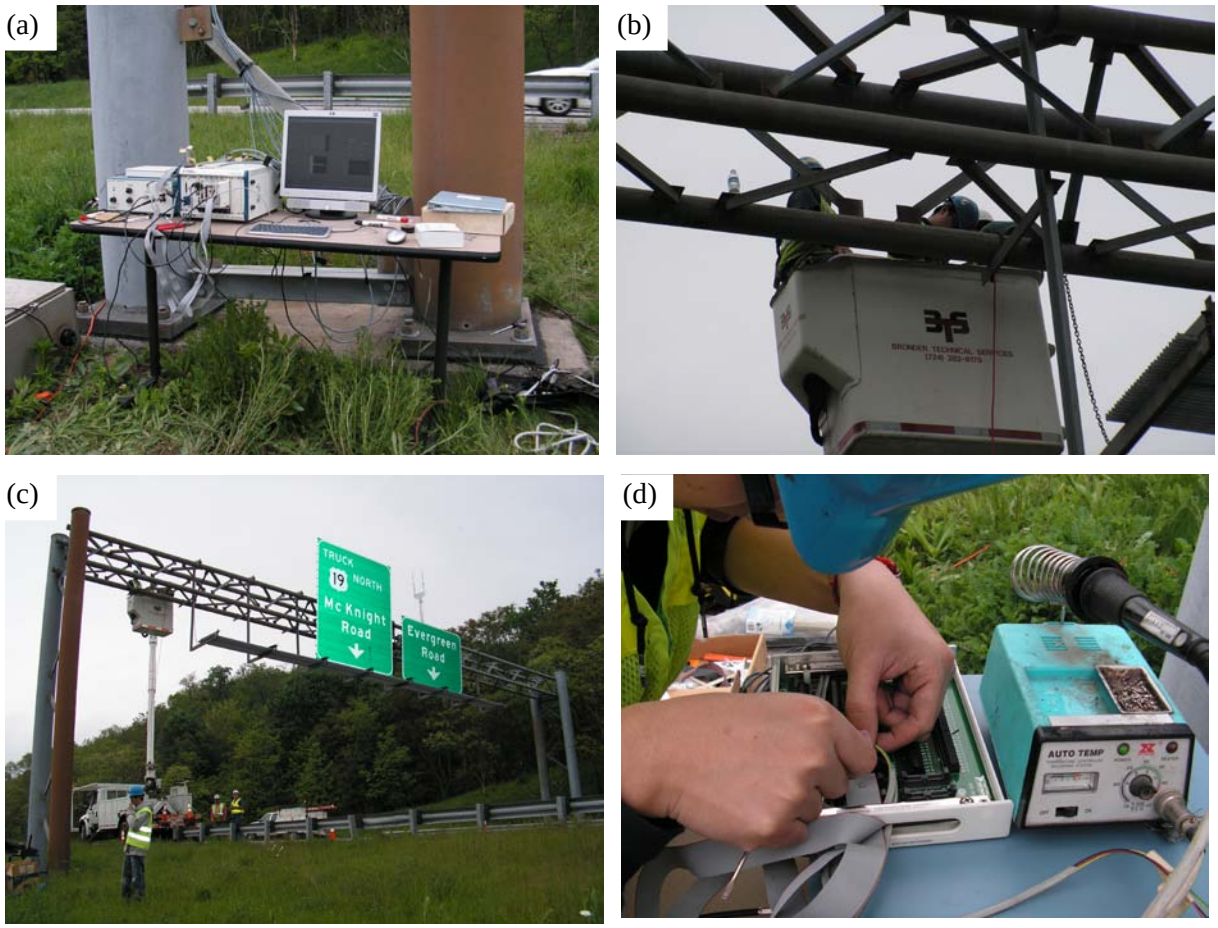

Figure 6.3 – Field testing. (a) Photo of the data acquisition system. (b-c) Bonding the PZTs to the structures. (d) Connecting the coaxial cables to the screw terminal.

The relative position of these transducers on the truss is shown in Fig. 6.2 (c). The transducers were named as S0, S1…S5. Two PZTs were used for the EMI method and are indicated as EM1 and EM2 in Fig. 6.2 (c). The sensors were connected to the data acquisition system by means of flexible multiconductor cable shielded 20/3 Awg cables. The same program software used for the indoor tests was used. The program was updated to allow acquisition at regular intervals without the intervention of the operator. For the field testing it was decided to monitor the structure every fifteen minutes. Phases of the installation, of assembling the wires to the data acquisition system are shown in Fig. 6.3.

6.2 TEST 1: RESULTS

6.2.1 May tests

The results presented here span over almost two months (May – June 2010) of measurements, which were taken on a weekly basis. In order to monitor the structure under different environmental conditions the days of tests were chosen based upon the weather forecast. During the month of May a total of 55 measurements recorded across four different days of tests were taken.

Table 6.1 summarizes the temperature of the air and of the steel pole. It should be noted that the air temperature was retrieved from the following link http://weather.org/weatherorg_records_and_averages.htm while the temperature of the material was recorded by attaching a thermocouple. The thermocouple was not used during the first two days. The rain during the first day of test was lighter than on May 17th. Tests on May 20th and 26th there were performed under clear sky conditions. Therefore the direct exposure to the sun of the poles and of the chord with the PZTs caused a significant difference between air and steel temperature.

Typical time waveforms recorded on May 17th specifically measurement 13, during heavy rain, are shown in Fig. 6.4. The signals refer to 175 kHz excitation frequency. The plots are relative to wave path (a) S0=>S2, (c) S0=>S5; (e) original S0=>S3; (g) original S1=>S3; (i) original S5=>S0. As done for the laboratory testing the first transducer indicated the PZT that acted as actuator and the second transducer indicated the PZT that acted as a sensor. The figures shown on the left column denote the presence of a very low frequency component. The origin of such low frequency was investigated. By examining a large number of time waveforms it was noted that: 1) during dry days only the wave paths where at least S1 or S3 was active presented time waveforms with low frequency component; 2) such a component was present irrespective of the excitation frequency (125 kHz, 150 kHz, etc…); 3) during the rainy days almost all wave paths presented such trend. Based upon this observation the role of the global structural vibration associated with wind (which was calm most of the day) or traffic (no induced truck gusts were experiences) can be excluded. The fact that S1 and S3 were attached to the diagonal members can be indicative of some small vibration on those members. Finally, the circumstance that under rain most many of the time waveforms were corrupted with a low frequency component suggests that raindrops hit the transducers causing some vibration.

In order to eliminate any bias on the features' calculation from the low frequency components, a digital filter was used. The Butterworth band pass filter was used. The magnitude and phase responses are shown in Fig. 6.5. The normalized frequency is Nyquist frequency, in this case 5 MHz. The bandwidth selected for the filtering was 100 – 270 KHz. The time signals after filtering are, for the sake of clarity, shown on the right column of Fig. 6.4. The extraction of the statistical features and the outlier analyses were performed on the filtered signals.

Fig. 6.6, 6.7 and 6.8 present the RMS, K factor and variance respectively associated with the measurement executed during the month of May. The plots refer to four different paths, namely, C0=>C2/C0=>C5, C0=>C3/C0=>C5, C1=>C3/C0=>C5, and C5=>C0/C0=>C5. The guided waves propagating at 175 kHz were considered for the analysis. It can be seen that the measurements obtained under heavy rain conditions produced a large scatter in the data.

Table 6.1 The record of measurement environmental effect

Meas. #	Date	Time	Air Temperature (C)	Time	Steel Temperature (C)	Dry / rain
1	12-May	8:53 AM	14.39		no measurement	dry
2	12-May	9:53 AM	14.39		no measurement	dry
3	12-May	10:02 AM	14.00		no measurement	dry
4	12-May	10:53 AM	13.89		no measurement	dry
5	12-May	11:45 AM	14.00		no measurement	dry
6	12-May	11:53 AM	14.39		no measurement	dry
7	12-May	12:53 PM	13.89		no measurement	dry
8	12-May	1:05 PM	13.00		no measurement	rain
9	12-May	1:28 PM	14.00		no measurement	rain
10	12-May	1:53 PM	14.39		no measurement	rain
11	12-May	2:53 PM	13.89		no measurement	rain
12	12-May	3:53 PM	13.89		no measurement	rain
13	17-May	9:49 AM	12.00		no measurement	rain
14	17-May	11:15 AM	12.00		no measurement	rain
15	17-May	11:39 AM	13.00		no measurement	rain
16	17-May	11:53 AM	12.78		no measurement	rain
17	17-May	12:53 PM	12.22		no measurement	rain
18	17-May	1:06 PM	13.00		no measurement	rain
19	17-May	1:29 PM	12.00		no measurement	rain
20	17-May	1:53 PM	12.22		no measurement	rain
21	20-May	9:04 AM	11.00	8:50 AM	16.4	dry
22	20-May	9:23 AM	11.00	9:12 AM	19.1	dry
23	20-May	9:27 AM	11.00	9:26 AM	19.8	dry
24	20-May	9:53 AM	12.22	9:45 AM	23.4	dry
25	20-May	10:53 AM	16.11	10:01 AM	26.3	dry
26	20-May	11:53 AM	18.89	10:15 AM	29.3	dry
27	20-May	12:53 PM	21.11	10:27 AM	31.5	dry
28	20-May	1:53 PM	23.28	10:42 AM	32	dry
29	20-May		23.89	10:59 AM	35	dry
30	20-May			11:12 AM	34.5	dry
31	20-May			11:28 AM	35.6	dry
32	20-May			11:42 AM	37.8	dry
33	20-May			12:00 PM	38.9	dry
34	20-May			12:30 PM	40.3	dry
35	20-May			12:45 PM	41.1	dry
36	20-May			13:00	40.7	dry
37	26-May	8:53 AM	22.78	8:55 AM	23	dry
38	26-May	9:53 AM	24.39	9:15 AM	27.8	dry
39	26-May	10:53 AM	25.61	9:33 AM	28.6	dry
40	26-May	11:53 AM	27.78	9:45 AM	30	dry
41	26-May	12:53 PM	26.72	9:59 AM	35.2	dry
42	26-May	1:53 PM	27.78	10:17 AM	43.7	dry
43	26-May			10:44 AM	41.1	dry
44	26-May			11:02 AM	44.6	dry
45	26-May			11:14 AM	46.5	dry
46	26-May			11:29 AM	46.7	dry
47	26-May			11:45 AM	46.8	dry
48	26-May			12:00 PM	40.8	dry
49	26-May			12:14 PM	48.5	dry
50	26-May			12:29 PM	49	dry
51	26-May			12:45 PM	42.3	dry
52	26-May			1:03 PM	39	dry
53	26-May			1:14 PM	36.9	dry
54	26-May			1:30 PM	36.6	dry
55	26-May			1:45 PM	36.6	dry

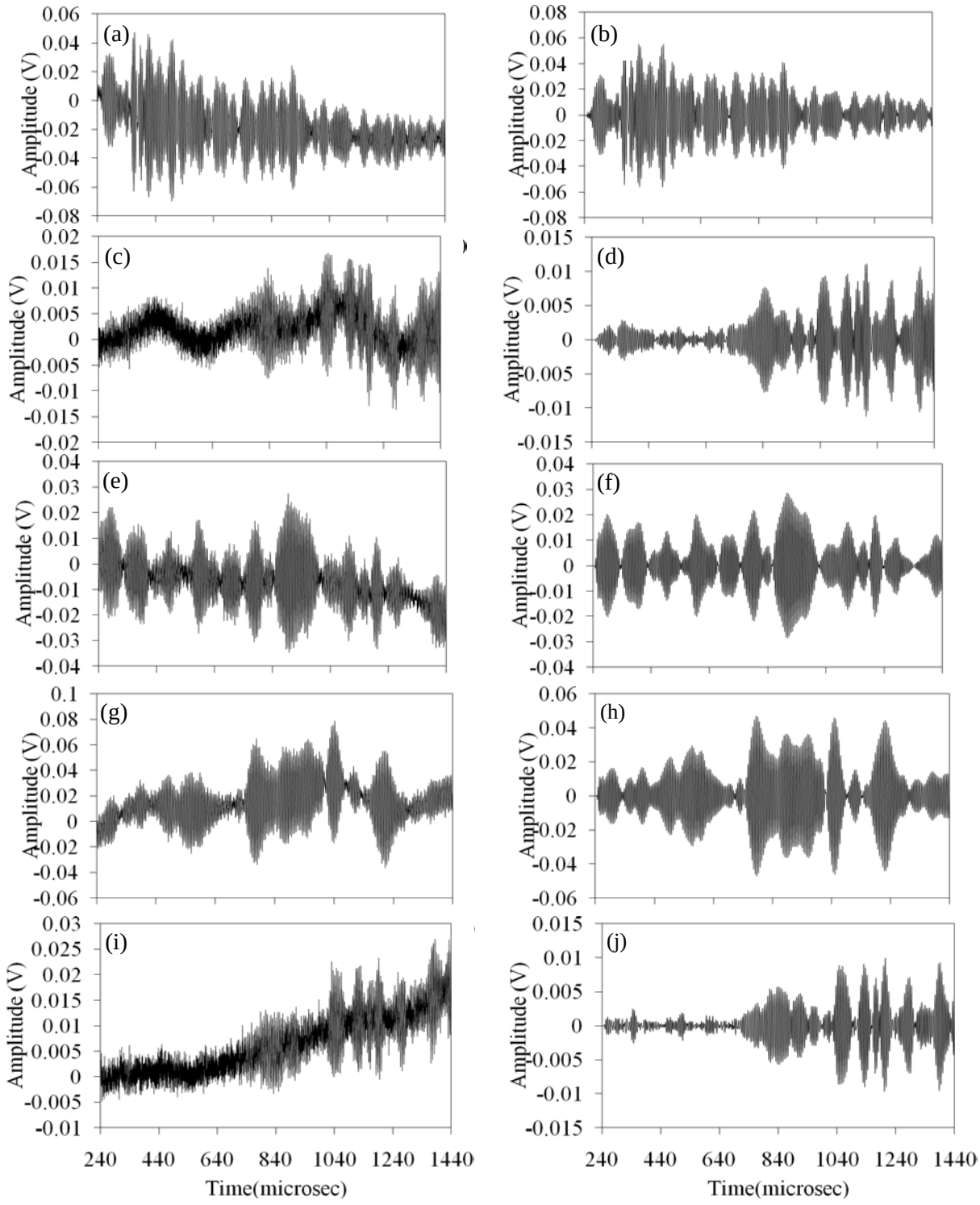

Figure 6.4 the original time waveforms of (a) S0=>S2; (c) S0=>S5; (e) S0=>S3; (g) S1=>S3; (i) S5=>S0; and the filtered time waveforms of (b) S0=>S2; (d) S0=>S5; (f) S0=>S3; (h) S1=>S3; (j) S5=>S0;

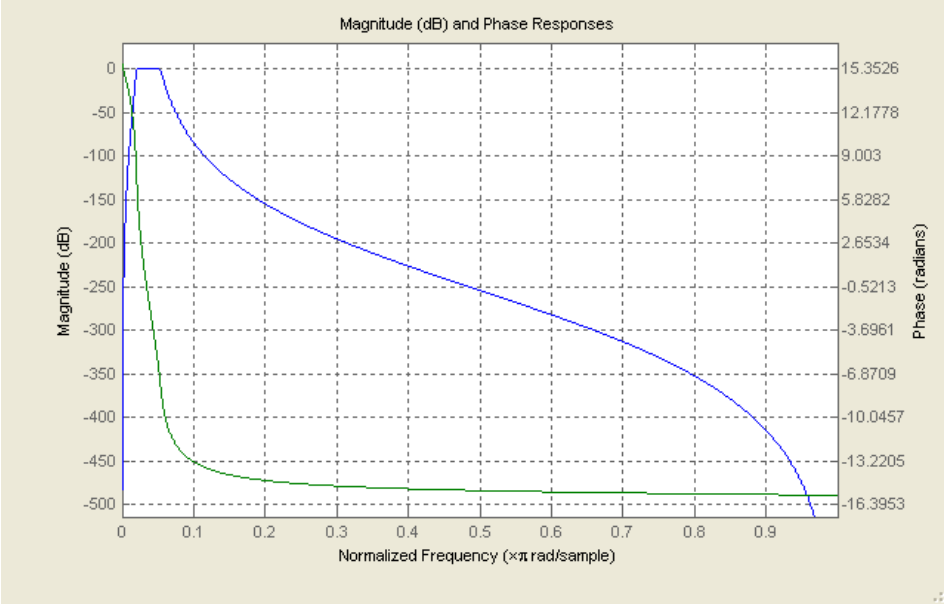

Figure 6.5 the magnitude and phase response of the simulated Butterworth band pass filter

The first 12 measurements were taken at the beginning as the transducers and connection equipment setup at the first day. A constant behavior was observed for S0=>S2/S0=>S5 (Fig. 6.6 (a), Fig. 6.7 (a) and Fig. 6.8 (a)) within the first day measurement and these measurements were used as training data in latter multivariate analysis. When it came to the rainy day corresponding to measurement 13-22, an unexpected dramatic variation and increase tendency was observed. When the rain stopped, the D.I. values came back to normal level as shown in measurement 21 and 22. More measurements in similar condition need to be taken and analyzed to address this problem. For measurement 23-37 and 38-55, slight variation resulted from the variation of temperature, and there was an increase tendency from 16.4°C to 25.3°C corresponding to measurement 23-27 and an increase tendency from 35°C to 41.1°C corresponding to measurement 30-37. Similar behavior was observed within measurement 38-55. Fig. 6.7 shows the results of the multivariate analysis associated with the damage index ratios introduced in Fig. 6.6.

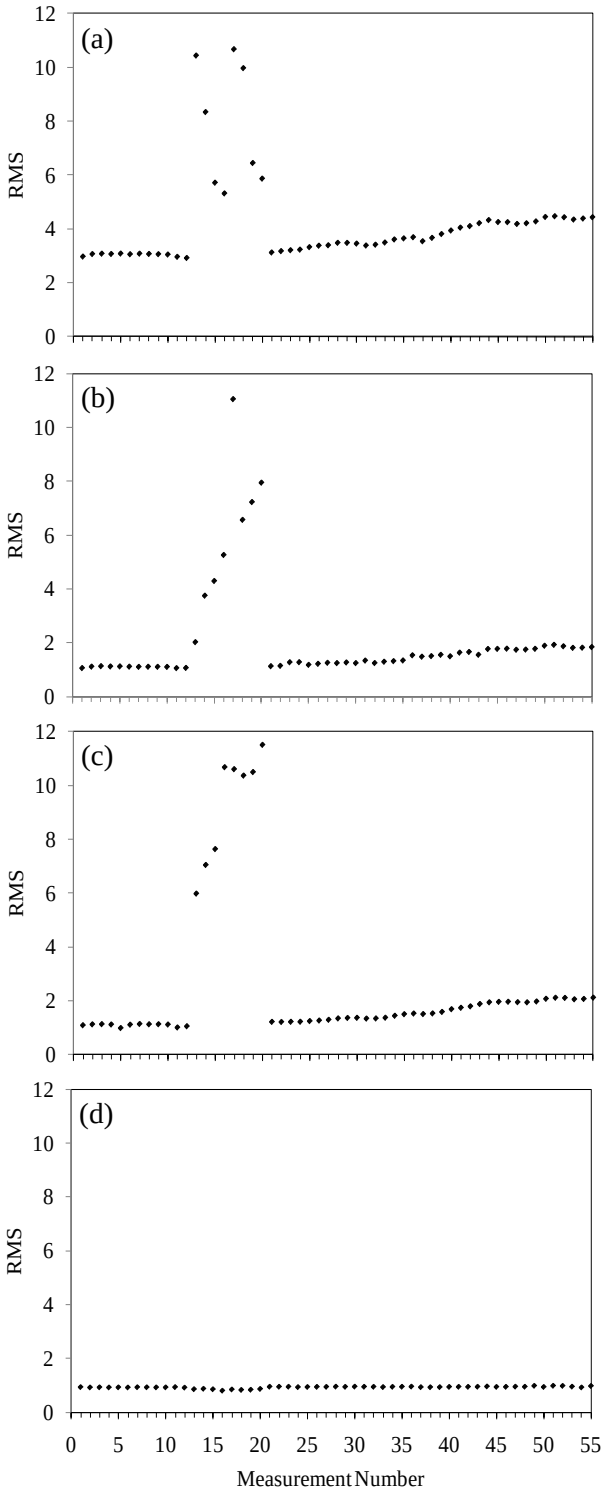

Figure 6.6 RMS Damage Index at May from path: (a) C0=>C2/C0=>C5; (b) C0=>C3/C0=>C5; (c) C1=>C3/C0=>C5 and (d) C5=>C0/C0=>C5

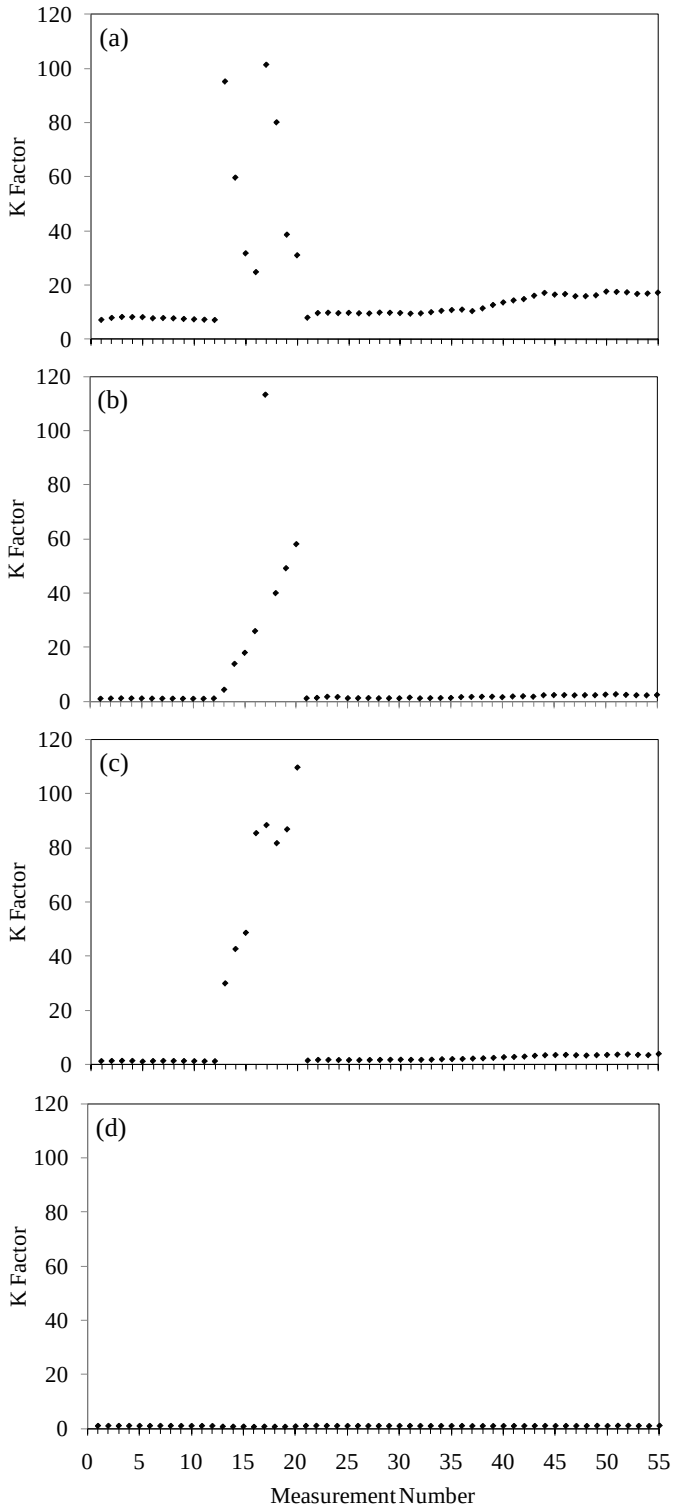

Figure 6.7 - K factor Damage Index at May from path: (a) C0=>C2/C0=>C5; (b) C0=>C3/C0=>C5; (c) C1=>C3/C0=>C5 and (d) C5=>C0/C0=>C5

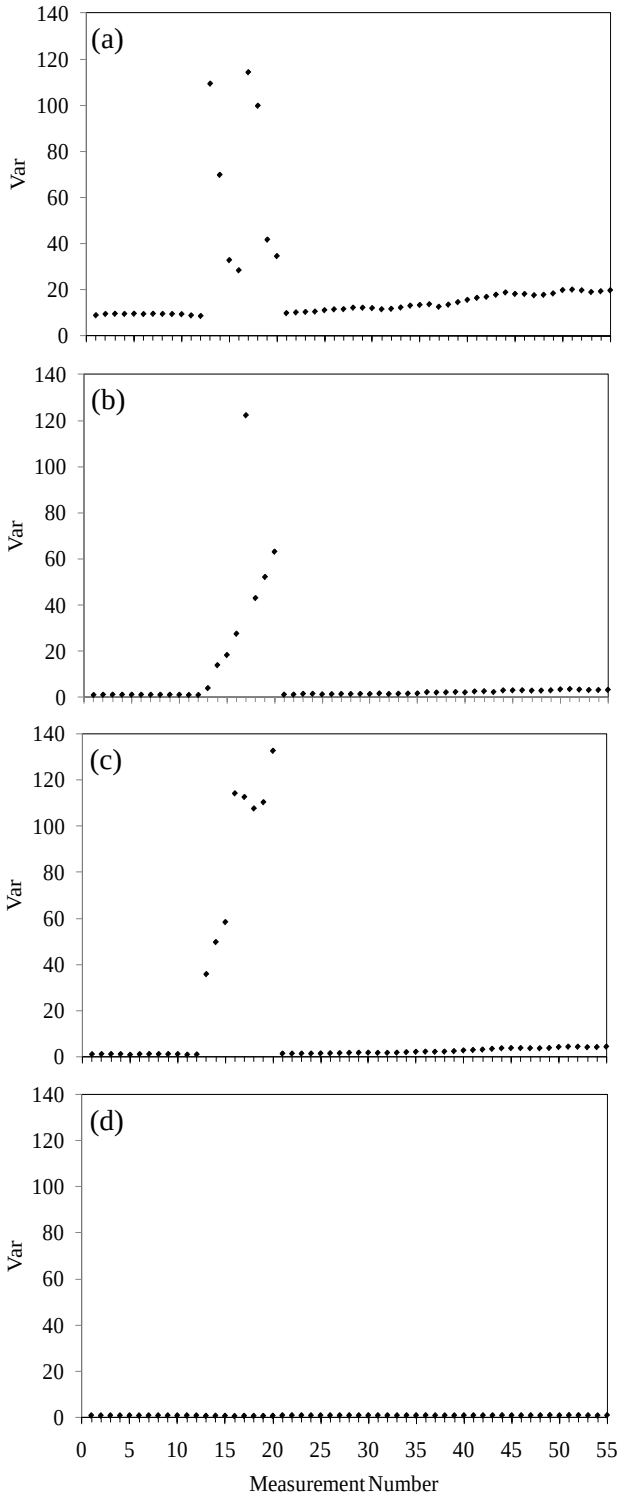

Figure 6.8 - Variance Damage Index at May from path: (a) C0=>C2/C0=>C5; (b) C0=>C3/C0=>C5; (c) C1=>C3/C0=>C5 and (d) C5=>C0/C0=>C5

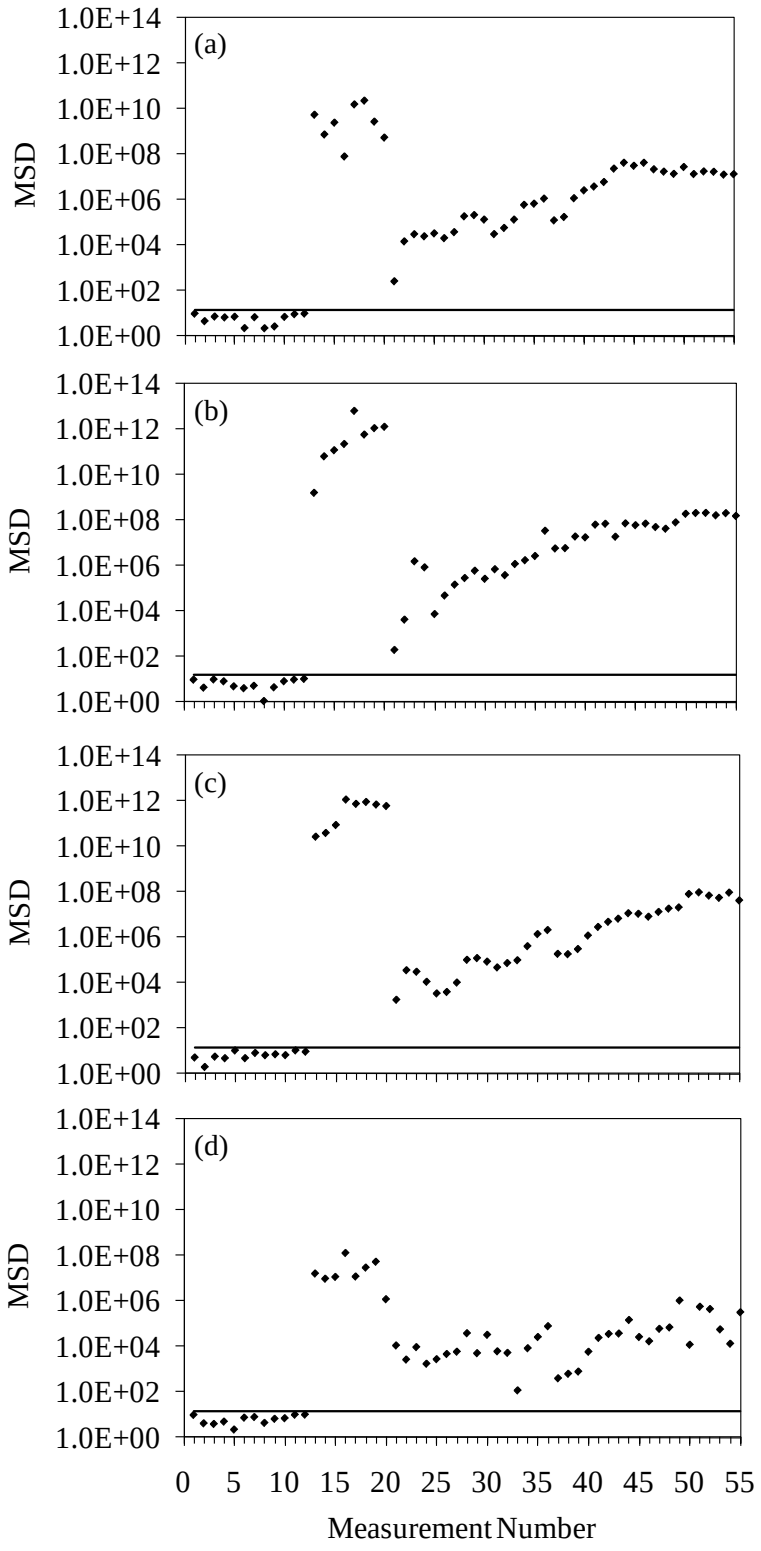

Figure 6.9 - Considering all 7 features MSD from path: (a) C0=>C2/C0=>C5; (b) C0=>C3/C0=>C5; (c) C1=>C3/C0=>C5 and (d) C5=>C0/C0=>C5

6.2.2 June tests

During the month of June a total of 40 measurements were taken recorded across three days of tests. Table 6.2 summarizes the temperature of the air and of the steel pole.

Table 6.2 – Weather condition during the field test during the month of June 2010.

Meas. #	Date	Time	Air Temperature (C)	Time	Steel Temperature (C)	Dry / rain
56	1-Jun	8:53 AM	20	8:44 AM	21.4	dry
57	1-Jun	9:26 AM	21	9:05 AM	21.6	dry
58	1-Jun	9:46 AM	21	9:21 AM	21.6	dry
59	1-Jun	9:53 AM	21.1	9:40 AM	22	dry
60	1-Jun	10:39 AM	22.0	9:55 AM	23.6	dry
61	1-Jun	10:53 AM	22.8	10:10 AM	26.5	dry
62	1-Jun	11:07 AM	22.0	10:25 AM	26.7	dry
63	1-Jun	11:44 AM	23.0	10:40 AM	26.6	dry
64	1-Jun			10:55 AM	25.8	dry
65	1-Jun			11:10 AM	27	dry
66	1-Jun			11:24 AM	29.6	dry
67	1-Jun			11:40 AM	25.3	dry
68	3-Jun	8:53 AM	18.9	9:13 AM	23.2	dry
69	3-Jun	9:53 AM	19.4	9:25 AM	23.1	dry
70	3-Jun	10:53 AM	19.4	9:40 AM	22.7	dry
71	3-Jun	11:53 AM	20.6	9:54 AM	23.2	dry
72	3-Jun	12:53 PM	22.2	10:17 AM	24.7	dry
73	3-Jun			10:31 AM	25.3	dry
74	3-Jun			10:45 AM	26.7	dry
75	3-Jun			11:06 AM	26.1	dry
76	3-Jun			11:21 AM	26.9	dry
77	3-Jun			11:37 AM	27.8	dry
78	3-Jun			11:52 AM	27.8	dry
79	3-Jun			12:06 PM	28.2	dry
80	3-Jun			12:21 PM	27.6	dry
81	3-Jun			12:35 PM	26.9	dry
82	3-Jun			12:50 PM	26.5	dry
83	3-Jun			1:11 PM	26.5	dry
84	9-Jun	9:08 AM	16.0	9:17 AM	17.9	rain
85	9-Jun	9:14 AM	16.0	9:37 AM	17.3	rain
86	9-Jun	9:44 AM	16.0	9:52 AM	17.7	rain
87	9-Jun	9:53 AM	16.1	10:08 AM	16.9	rain
88	9-Jun	10:07 AM	17.0	10:19 AM	16.9	rain
89	9-Jun	10:23 AM	17.0	10:36 AM	16.2	rain
90	9-Jun	10:53 AM	17.2	10:59 AM	17.7	rain
91	9-Jun	11:53 AM	17.8	11:08 AM	18.5	rain
92	9-Jun			11:22 AM	18.5	rain
93	9-Jun			11:37 AM	18.9	rain
94	9-Jun			11:54 AM	18.7	rain
95	9-Jun			12:07 PM	18.7	rain

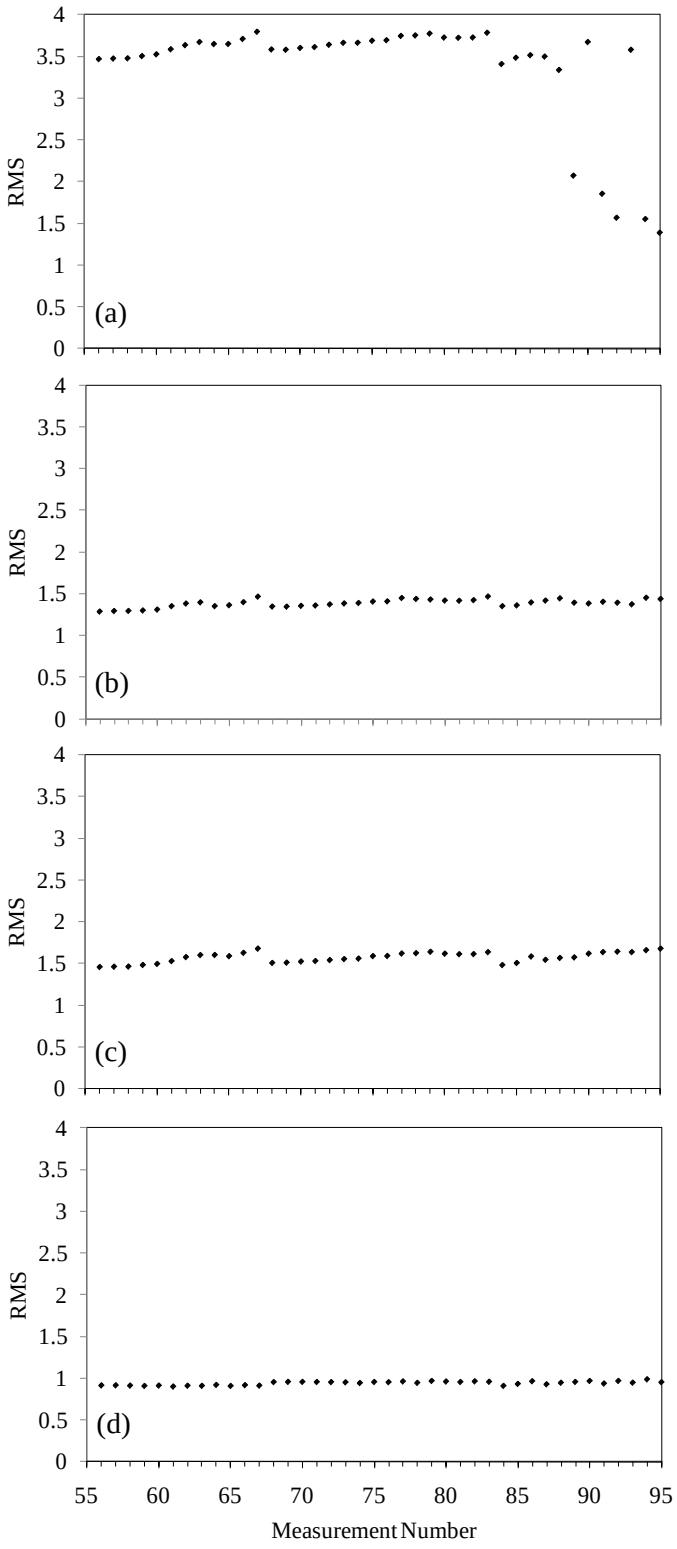

Figure 6.10 - RMS DI at June from path (a) C0=>C2/C0=>C5; (b) C0=>C3/C0=>C5; (c) C1=>C3/C0=>C5 and (d) C5=>C0/C0=>C5

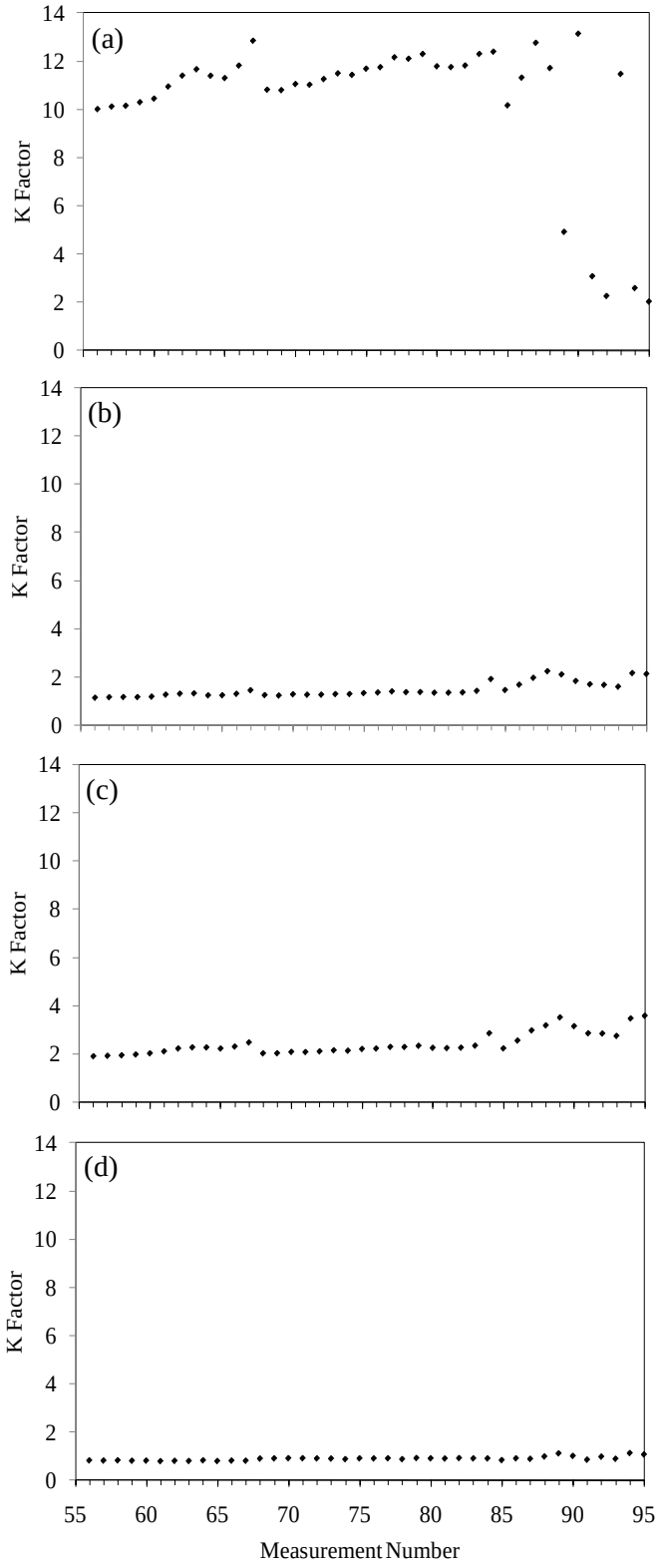

Figure 6.11 - K factor DI at June from path (a) C0=>C2/C0=>C5; (b) C0=>C3/C0=>C5; (c) C1=>C3/C0=>C5 and (d) C5=>C0/C0=>C5

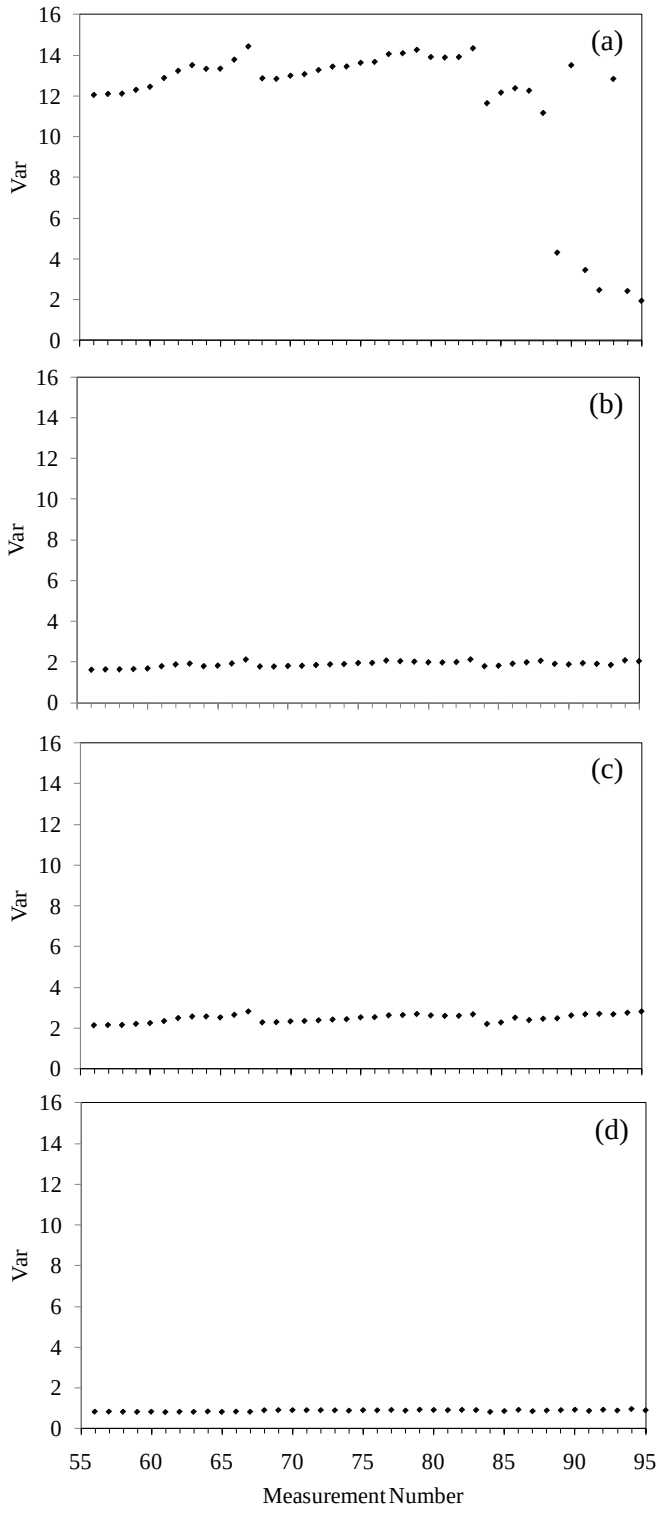

Figure 6.12 - Variance DI at June from path (a) C0=>C2/C0=>C5; (b) C0=>C3/C0=>C5; (c) C1=>C3/C0=>C5 and (d) C5=>C0/C0=>C5

Tests on June 1st and 3rd there were performed under clear sky conditions. Test on June 9th was taken under scattered shower condition. Fig. 6.10, 6.11, and 6.12 present the RMS, K factor as a function of the measurement number. The figures refer to the following wave path ratios: C0=>C2/C0=>C5, C0=>C3/C0=>C5, C1=>C3/C0=>C5, and C5=>C0/C0=>C5. The guided waves propagating at 175 kHz were considered for the analysis. By looking at the first 12 measurements (measurement 56 to 67) in Fig. 6.10 (b), (c), Fig. 6.11 (b), (c), Fig. 6.12 (b) and (c), the values of the statistical features are directly proportional to the truss temperature.

For measurements 68 to 83 associated with the test conducted on June 3rd, Fig. 6.10 (b), (c), 6.11 (b), (c), 6.12 (b), and (c), show a similar correlation between the statistical ratios and the temperature. For the last 12 measurements (84 - 95), however the data appear to be very scattered although a certain trend between values and temperature is still visible. When compared to the data number 13-20, the measurements within the range 84 – 95 may surprise as they were mainly acquired during wet conditions. However it should be remarked that the rain activity on May 17th was significantly higher than the one experienced on June 9th.

6.3 TEST 2: SETUP

The second field test was performed on the sign support structure shown in Fig. 6.13 (a). The structure is located along Interstate 279 at the same location of the structure described in the previous section. The truss information was specified in Appendix C. The truss consists of angular members. The diagonal members are bolted and welded to the main chord as shown in Fig. 6.13 (b).

Figure 6.13 – (a) Photo of the structure monitored in the field, the red circle and arrows show the joints involved in this experiment. (b) Particular of the welded connections

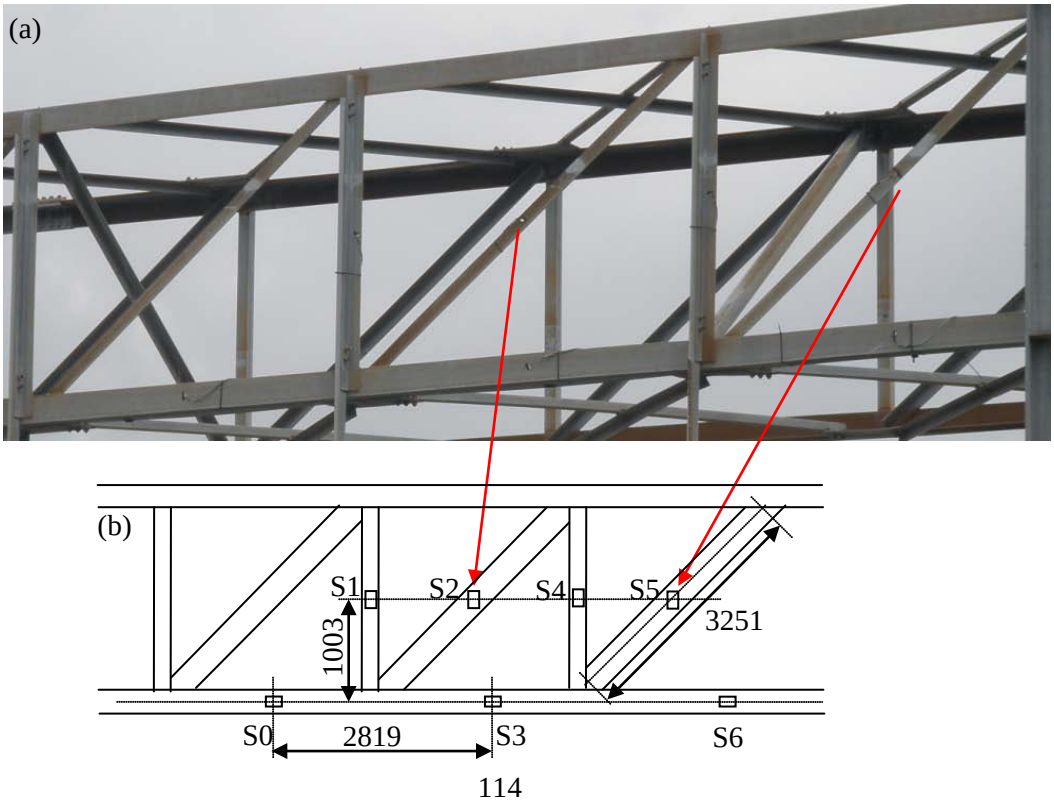

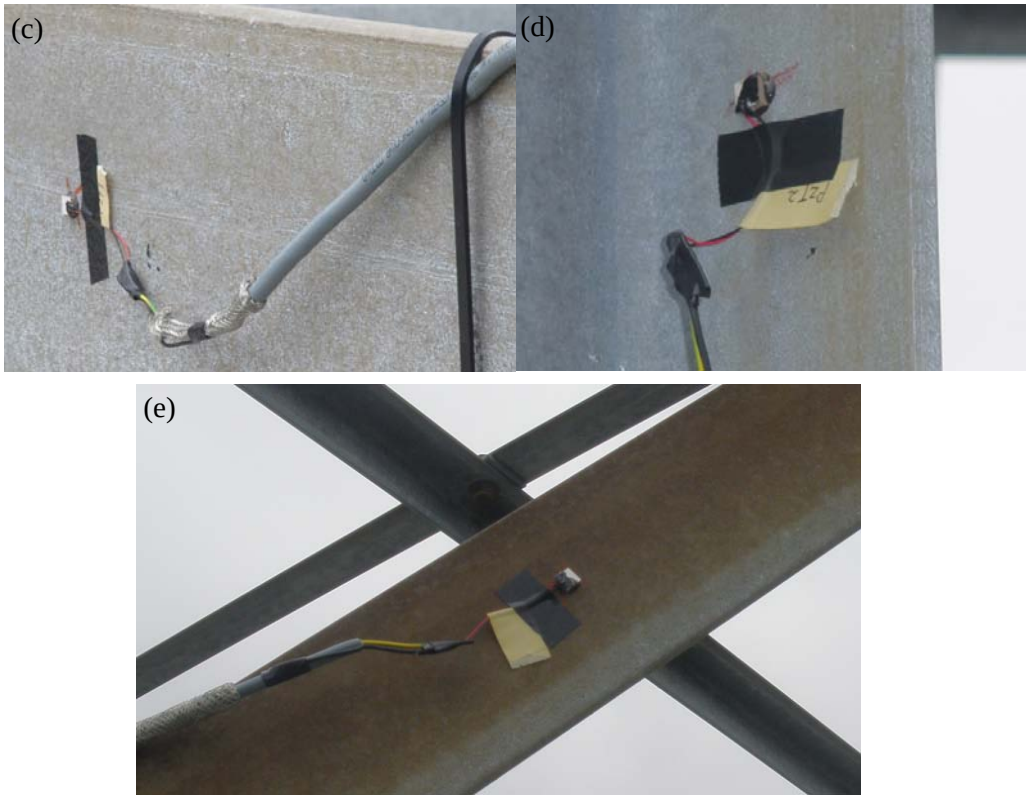

Figure 6.14 - (a) Close-up view of the part that was monitored. (b) Location of the sensing system. The red arrows shows the diagonal members involved in the field test. (c) Close-up view of S0. (d) Close-up view of S1. (e) Close-up view of S2. Distances are expressed in mm.

The sensing system was deployed on the bottom chord of the truss facing the northbound direction. Similar to what done for field test 1, seven PZTs in shear mode were bonded to the structure (Fig. 6.14 (a)). During the installation one traffic lane was closed for safety. All PZTs were used for the generation and detection of GUWs. The relative position of these transducers on the truss is shown in Fig. 6.14 (b). The transducers were named as S0, S1…S6. Typical transducers' orientations and setups are shown in Fig. 6.14 (c), (d) and (e). The sensors were connected to the data acquisition system by means of flexible multi-conductor cable shielded 20/3 AWG cables.

For this test it was decided to monitor the structure every fifteen minutes and to use the propagation of guided waves as a means for SHM. Phases of the installation are shown in Fig. 6.15.

(a) (b)

Figure 6.15 - Field testing: (a) Set up the safety rope. (b) Measuring the geometry of the trusses.

6.4 TEST 2: RESULTS

The results presented here refer to six days of measurements. In order to monitor the structure under different environmental conditions the days of tests were chosen based upon the weather forecast. During this test, a total of 74 measurements recorded across six different days of tests were taken. Table 6.3 summarizes the temperature of the air and of the steel pole. It should be noted that the air temperature was retrieved through the following link http://weather.org/weatherorg_records_and_averages.htm while the temperature of the material was recorded by attaching a thermocouple to one of the poles of the structure. On June 22nd, there was light rain during the first six measurements. On June 22nd, there was a mild rain at the first six measurements, and on July 20th, there was a rain during the first measurement.

In the field test, because the environmental factors are more complicated and uncontrollable, the data were processed using a Butterworth band pass filter to get rid of the background noise and low-frequency vibration of the structure. The normalized frequency is Nyquist frequency, in this case 5 MHz, and the corresponding passing bandwidth was settled from 100 KHz to 270 KHz based on the frequency domain information. Typical time waveforms recorded on June 17th are shown in Fig 6.16. The plots are relative to pairs : (a) original S0=>S2; (b) filtered S0=>S2;

(c) original S0=>S3; (d) filtered S0=>S3; (e) original S3=>S4; (f) filtered S3=>S4; (g) original S3=>S5; (g) filtered S3=>S5; (i) original S3=>S6 and (j) filtered S3=>S6; (k) original S1=>S0 and (l) filtered S1=>S0, where the first number identifies the PZT acting as actuator and the second number indicates the PZT acting as sensor. After signal filtering, time window were applied and statistical features were extracted from selected windowed information.

Fig. 6.17, 6.18 and 6.19 present the RMS, K factor and variance respectively associated with the measurements executed during the month of June. The plots refer to six different Damage Indexes, namely, S0=>S2/S3=>S0, S0=>S3/S3=>S0, S3=>S4/S3=>S0, S3=>S5/S3=>S0, S3=>S6/S3=>S0 and S1=>S0/S3=>S0, in which features extracted from S3=>S0 were used as normalization. The guided waves propagating at 175 kHz were considered for the analysis. It can be seen that the measurements obtained under mild rain conditions produced a large step-wise drop in the RMS values at measurement number 7, 8 and 9 (not shown in some plots in purpose to show the little variance with stable environmental conditions) as shown in Fig. 6.17. Generally speaking, as the increase of temperature, a slight increasing tendency could be observed in Fig. 6.17 (a), Fig. 6.18 (a) and Fig. 6.19 (a)) within the measurements from 24 to 75, which shows the same pattern as we found in the test for first structure. The scattering from measurement number 17 to 23in Fig. 6.17 (f) is unexpected for the environmental conditions were stable along that period.

Table 6.3 The record of temperature of the air and of the steel pole

Meas. #	Date	Time	Air Temp.(°C)	Time	Steel Temp. (°C)	Dry / rain
1	17-Jun	1:53 PM	19.39	1:47 AM	28.9	dry
2	17-Jun	2:53 PM	19.39	2:02 AM	28.3	dry
3	17-Jun	3:53 PM	20.61	2:26 AM	29.8	dry
4	17-Jun	4:53 PM	20.61	2:41 AM	29.3	dry
5	17-Jun			2:56 AM	29.5	dry
6	17-Jun			3:10 AM	29.8	dry
7	17-Jun			3:26 AM	34	dry
8	22-Jun	8:53 AM	20.61	8:52 AM	no measurements	rain
9	22-Jun	9:00 AM	21.00	9:07 AM	no measurements	rain
10	22-Jun	9:14 AM	21.00	9:22 AM	no measurements	rain
11	22-Jun	9:24 AM	21.00	9:41 AM	25.3	rain
12	22-Jun	9:32 AM	21.00	9:56 AM	27.2	rain
13	22-Jun	9:49 AM	21.00	10:09 AM	28.6	rain
14	22-Jun	9:53 AM	21.11	10:26 AM	31.4	dry

Table 6.3 (continued)

15	22-Jun	10:53 AM	22.78	10:45 AM	31.4	dry
16	22-Jun	11:53 AM	23.28	11:02 AM	32	dry
17	22-Jun	12:03 PM	24.00	11:17 AM	35.3	dry
18	22-Jun	12:18 PM	24.00	11:31 AM	34.5	dry
19	22-Jun			11:42 AM	33.3	dry
20	22-Jun			11:56 AM	33.5	dry
21	22-Jun			12:02 PM	33.4	dry
22	22-Jun			12:17 PM	33.3	dry
23	22-Jun			12:32 PM	33.3	dry
24	29-Jun	8:53 AM	20.61	8:45 AM	no measurements	dry
25	29-Jun	9:53 AM	20.00	9:00 AM	no measurements	dry
26	29-Jun	10:53 AM	19.39	9:15 AM	no measurements	dry
27	29-Jun	11:53 AM	19.39	9:30 AM	24.7	dry
28	29-Jun	12:12 PM	21.00	9:45 AM	24.4	dry
29	29-Jun	12:22 PM	20.00	10:00 AM	26.3	dry
30	29-Jun	12:35 PM	20.00	10:15 AM	28.1	dry
31	29-Jun	12:53 PM	19.39	10:30 AM	28.2	dry
32	29-Jun			10:45 AM	29.5	dry
33	29-Jun			11:00 AM	31.2	dry
34	29-Jun			11:15 AM	31.2	dry
35	29-Jun			11:30 AM	29.5	dry
36	29-Jun			11:45 AM	29.5	dry
37	29-Jun			12:00 PM	29.4	dry
38	29-Jun			12:15 PM	29.9	dry
39	29-Jun			12:30 PM	29.7	dry
40	8-Jul	8:53 AM	26.72	9:16 AM	27.8	dry
41	8-Jul	9:53 AM	28.28	9:30 AM	28.5	dry
42	8-Jul	10:53 AM	30.00	9:45 AM	32.6	dry
43	8-Jul	11:53 AM	30.00	10:00 AM	33.3	dry
44	8-Jul	12:53 PM	30.00	10:15 AM	33	dry
45	8-Jul			10:30 AM	35.3	dry
46	8-Jul			10:45 AM	38.7	dry
47	8-Jul			11:00 AM	42.4	dry
48	8-Jul			11:15 AM	44	dry
49	8-Jul			11:30 AM	46.2	dry
50	8-Jul			11:45 AM	46.6	dry
51	8-Jul			12:00 PM	47.7	dry
52	8-Jul			12:15 PM	45.4	dry
53	8-Jul			12:30 PM	45	dry
54	13-Jul	8:53 AM	23.28	9:45 AM	30.1	dry

Table 6.3 (continued)

55	13-Jul	9:53 AM	23.89	10:00 AM	30	dry
56	13-Jul	10:53 AM	25.00	10:15 AM	31.1	dry
57	13-Jul	11:53 AM	25.61	10:30 AM	33.3	dry
58	13-Jul	12:53 PM	26.11	10:45 AM	33.2	dry
59	13-Jul	1:53 PM	26.11	11:00 AM	31.5	dry
60	13-Jul			11:15 AM	33.2	dry
61	13-Jul			11:30 AM	33.2	dry
62	13-Jul			11:45 AM	36.9	dry
63	13-Jul			12:00 PM	37.4	dry
64	13-Jul			12:15 PM	36.2	dry
65	13-Jul			12:30 PM	36	dry
66	20-Jul	9:21 AM	22.00	9:15 AM	22.8	rain
67	20-Jul	9:53 AM	22.22	9:30 AM	23	wet
68	20-Jul	10:33 AM	22.00	9:45 AM	23.3	wet
69	20-Jul	10:53 AM	22.78	10:00 AM	23.4	wet
70	20-Jul	11:25 AM	23.00	10:15 AM	24	dry
71	20-Jul	11:27 AM	24.00	10:30 AM	24.8	dry
72	20-Jul	11:39 AM	24.00	10:45 AM	25.1	dry
73	20-Jul			11:00 AM	24.4	dry
74	20-Jul			11:15 AM	26	dry

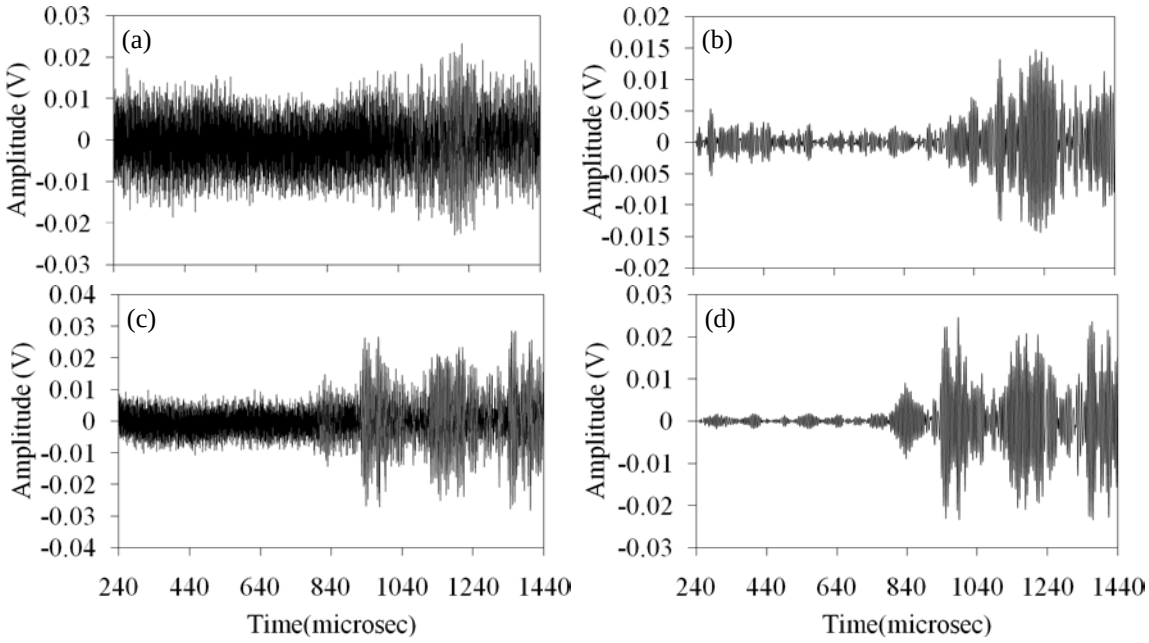

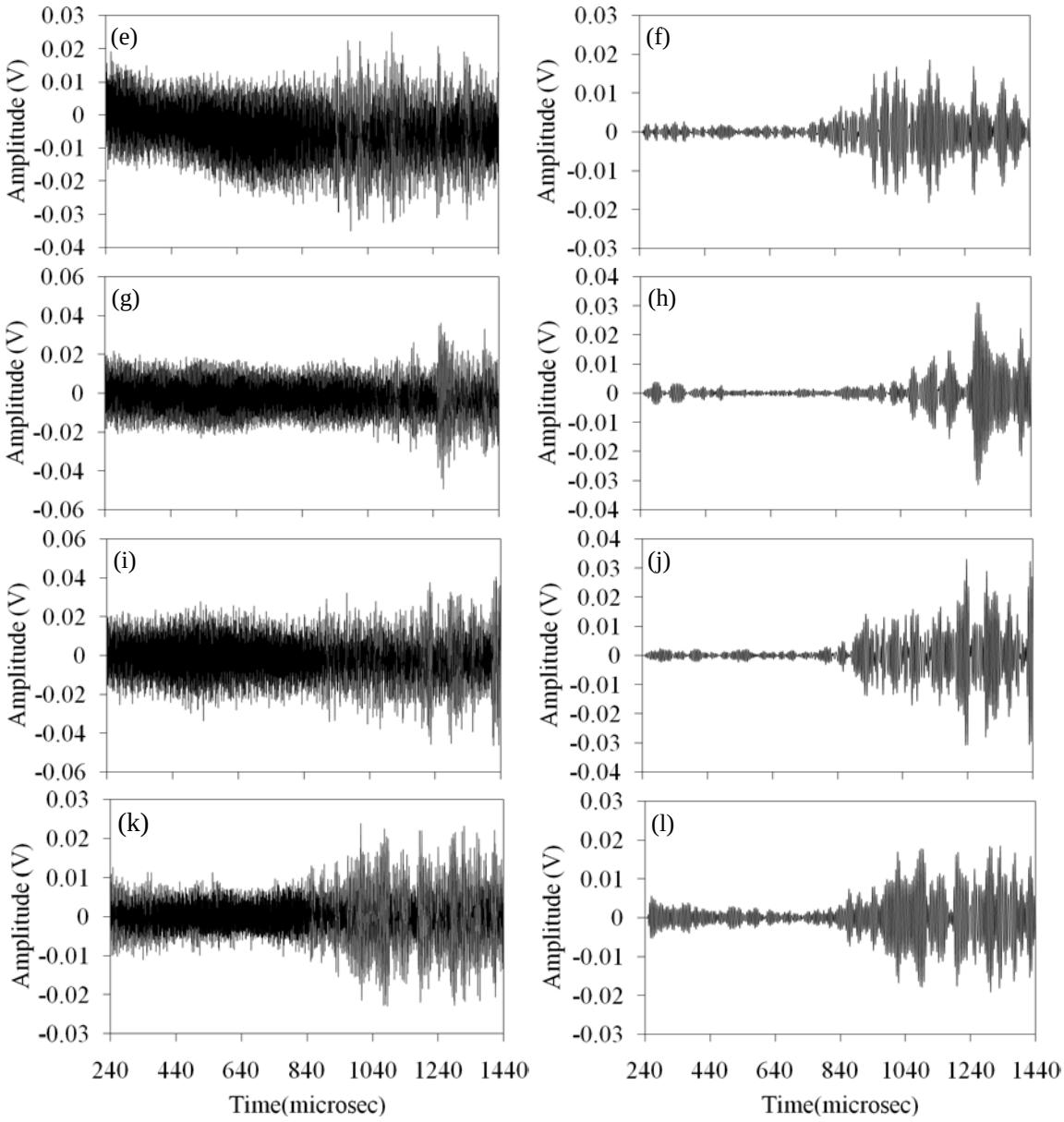

Figure 6.16 - The original time waveforms of 175 kHz for paths: (a) S0=>S2; (c) S0=>S3; (e) S3=>S4; (g) S3=>S5; (i) S3=>S6; (k) S1=>S0 and the filtered time waveforms of (b) S0=>S2; (d) S0=>S3; (f) S3=>S4; (h) S3=>S5; (j) S3=>S6; (l) S1=>S0 at the fourth measurement on June 17th.

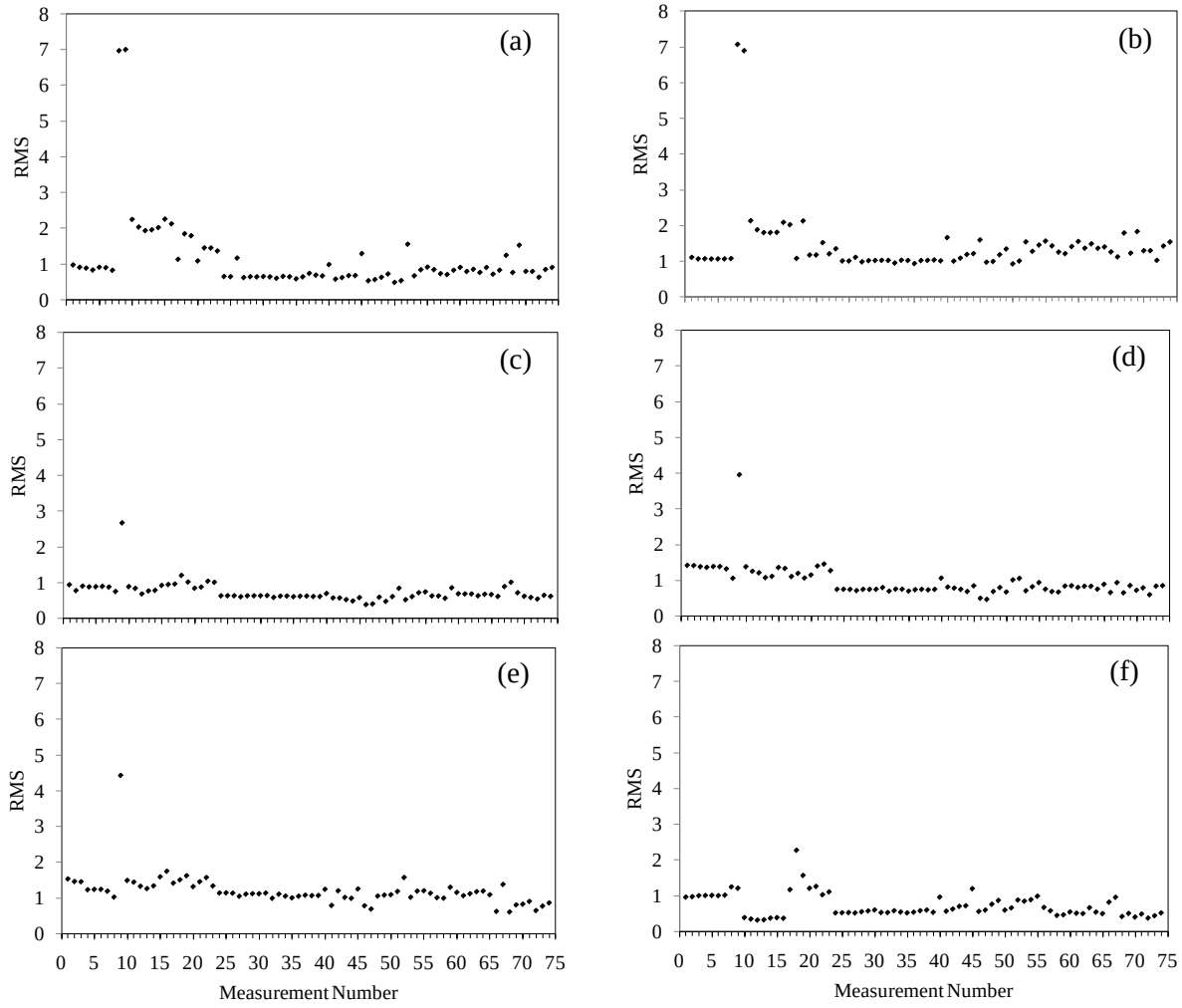

Figure 6.17 - RMS Damage Index at June from path: (a) S0=>S2/S3=>S0; (b) S0=>S3/S3=>S0; (c) S3=>S4/S3=>S0; (d) S3=>S5/S3=>S0; (e) S3=>S6/S3=>S0 and (f) S1=>S0/S3=>S0

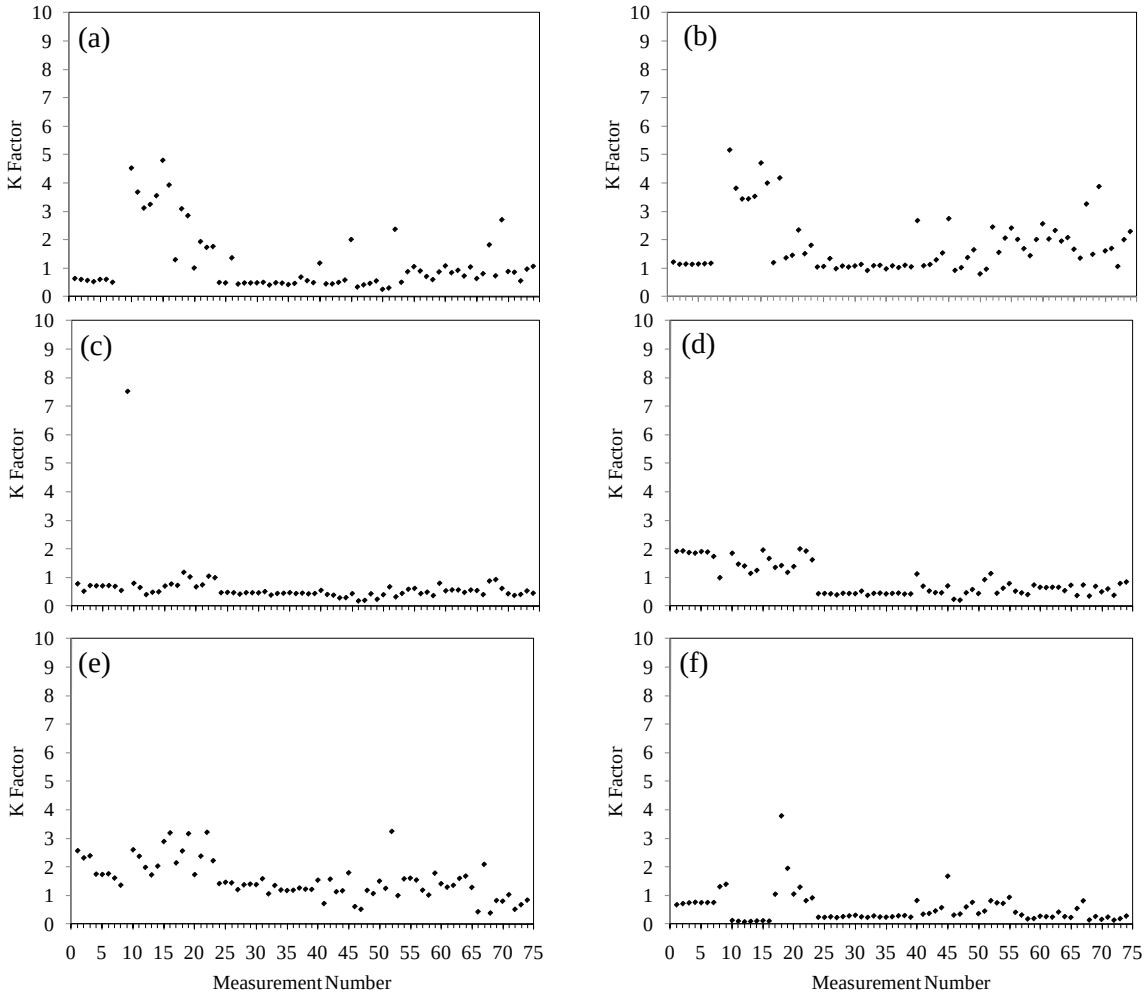

Figure 6.18 - K factor Damage Index at June from path: (a) S0=>S2/S3=>S0; (b) S0=>S3/S3=>S0; (c) S3=>S4/S3=>S0; (d) S3=>S5/S3=>S0; (e) S3=>S6/S3=>S0 and (f) S1=>S0/S3=>S0

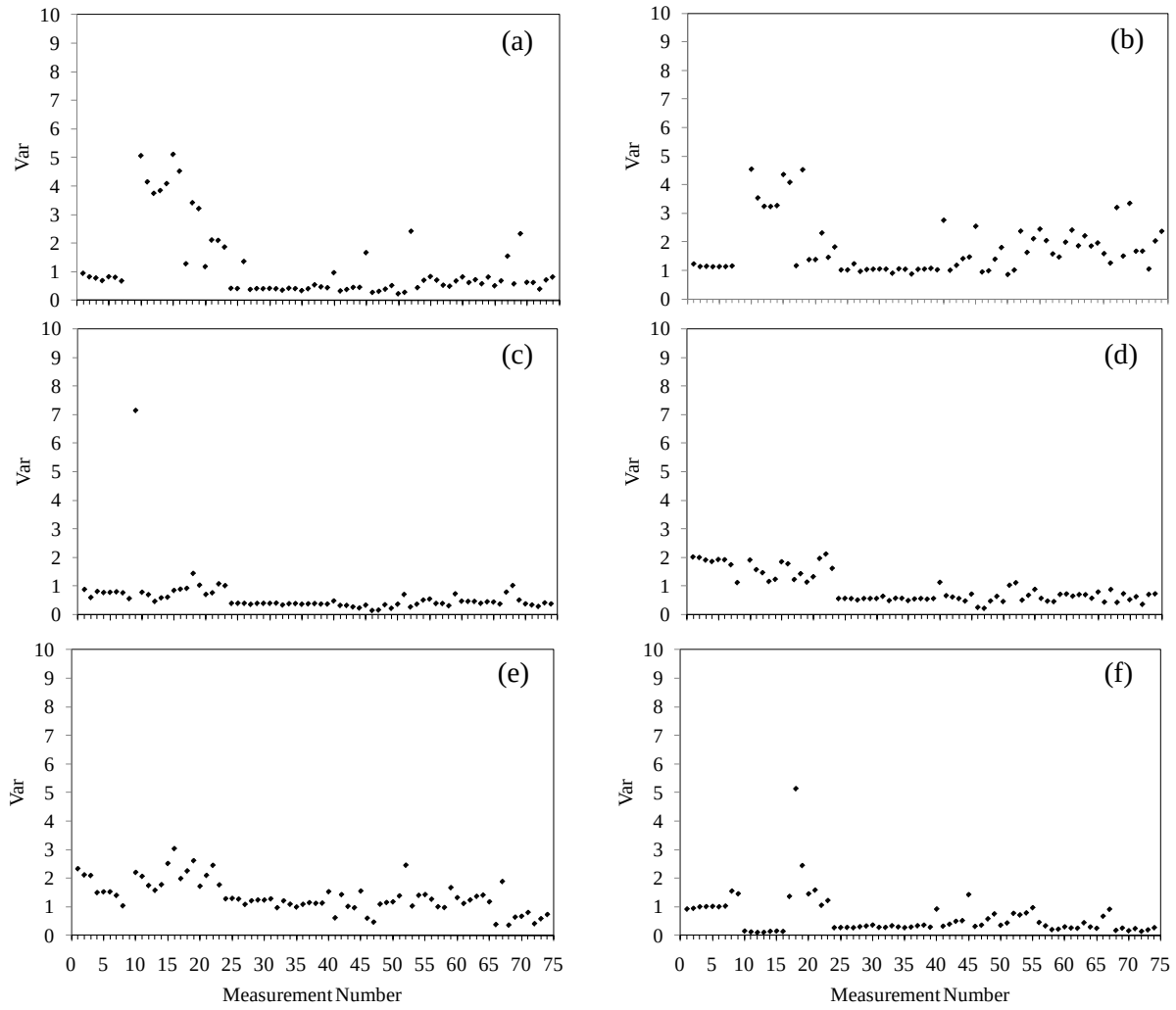

Figure 6.19 - Variance Damage Index at June from path: (a) S0=>S2/S3=>S0; (b) S0=>S3/S3=>S0; (c) S3=>S4/S3=>S0; (d) S3=>S5/S3=>S0; (e) S3=>S6/S3=>S0 and (f) S1=>S0/S3=>S0

The potential reason could be the low signal to noise ratio (SNR) for this test compared with previous tests: the lower SNR signals are more vulnerable to the environmental factors, as the distortion and vibration could make it difficult to discriminate the background noise and signals. Furthermore, the reason resulted in the difference on the performance with same measurement system and same type sensors between the two structures should be the different geometries of two structures which make the wave propagation modes significantly vary from each other. The experiment setup, specifically the PZTs departure further from each other compared with the first structure experiment, and the wave attenuation degraded the SNR which also increased the uncertainty in the experiment.

7.0 CONCLUSIONS

7.1 DISCUSSION

This thesis presents the results of a study about sensing technology for highway sign support structures. The objective of this study is to develop an inspection/monitoring technology to assess the structural soundness of such structures.

This report presents the research and development outcomes of two NDE/SHM methodologies aimed at detecting damage in sign support structures. The first method consists of the excitation and detection of guided ultrasonic waves at frequencies ranges between 100 kHz and 300 kHz by means of an array of small piezoceramic transducers (PZT). The detected waves were processed by extracting statistical features from the time waveforms and feeding an unsupervised learning algorithm based on the outlier analysis. The second NDE/SHM method investigated in this study was the electromagnetic impedance method, which exploits the mechanical impedance of a structure to monitor in real-time changes in structural stiffness and damping. Because direct measurements of the mechanical impedance of a structure are difficult to obtain, the electromechanical coupling effect of the host structure (the sign support in this work) and a PZT is measured. In fact whenever a PZT is driven by an electrical current, the structure is deformed and produces a local dynamic response. This response is detected by the same PZT as an electrical response, which is analyzed by an impedance analyzer. Any damage in the host structure results in changes to its mechanical impedance, which will be observed by changes in the electrical impedance of the PZT material.

In the framework of the research works associated with the sensing technology the following activities were conducted: 1) large scale testing at the Watkins-Haggart laboratory at the University of Pittsburgh (Pitt); and 2) field testing along interstate 279 few miles north of Pittsburgh. The experiments at Pitt aimed at developing a robust ultrasonic signal processing and

impedance method analysis for field deployment. Robustness against noise, low-frequency (very few Hertz) vibration, and environmental variations were considered. The density of the array (number of PZTs per unit length) was determined with the goal of minimizing the cost per sensing unit. On one of the main chords of each structure tested in the field, PZT were bonded and data were collected on a weekly basis.

7.2 SUMMARY OF FINDINGS

Chapter 1 motivated the study and described the outline of the report.

Chapter 2 demonstrated that currently only four NDE techniques are considered for the inspection of sign support structures: visual inspection; liquid penetrant; magnetic particles, and ultrasonic testing. Visual inspection is the most widely used and the most economic solution. However it is ineffective to detect internal flaws. Some of them however are very expensive like the Xray technique which also carried out safety issues related to radiation. Other technique like acoustic emission, ultrasonic guided waves, or EMI can be used although no practical employment in the field has been reported for overhead sign structures.

Chapter 3 described: 1) the structure tested at the University of Pittsburgh; 2) the hardware and software used for the experiments and the test protocol; 3) the structural health monitoring algorithm applied to the propagation of guided waves. The sensing system adopted in this study cost about $10-15 a piece excluding the wiring needed to connect them to the NI-PXI. The data acquisition system including the software is at about $12,000-$15,000 and can control up to thirty-two PZTs. As such the hardware/software scheme presented in this chapter would be able to control up to n • (n-1) wave propagation paths, where n = 32. The Labview program used to control both monitoring systems was built in house and has flexible to be modified at the user convenience and necessity. Software program used has been proposed. However, for larger number of transducers the software tasks should be optimized to secure fast execution and lower time consumption.

Chapter 4 described the results of the SHM algorithm applied to GUW data. It was found that:

• PZT as far as 2 meters (~7 feet) are able to detect guided waves with large signal to noise ratio;

• several PZT pairs are able to detect the presence of a small size crack around the weld toe;

• certain waveform paths are more sensitive than other paths which therefore should be ignored;

• multivariate analysis outperforms univariate analysis;

• the appropriate combination of certain features may outperform the use of all of the features selected for the study;

• certain frequencies, namely 150 kHz, 175 kHz, and 200 kHz are more sensitive to the presence of damage than the other frequencies considered;

• few wave propagation paths can be used, which therefore implies that a lower number of PZT may be used to monitor a joint; the dynamic load would not affect the guided wave measurements and therefore the approach appears to be robust against field loading conditions;

• extreme care must be paid to the handling of the wiring connection and PZT conditions to mitigate false positives.

• environmental factors such as low-warm temperatures or dry-rain-snow conditions over the chord and the sensors may alter significantly the values of the damage index ratios considered in this study.

Chapter 5 described the results of the SHM algorithm applied to EMI data. It was found that:

• the hardware/software system proposed here may replace the use of high cost impedance analyzers or LCR meters which are conventionally used in the measurements of the electromechanical impedance;

• the method is less sensitive to the presence of damage growth when compared to the performance of the UGW measurement;

• the application of the outlier analysis greater improve the sensitivity of the method;

• the position of the crack with respect to the EM transducers was very likely unfavorable, which means that for a bulk structure like the truss the location of the PZT to exploit the

EMI method must be carefully evaluated;

• extreme care must be paid to the handling of the wiring connection and PZT conditions to mitigate false positives.

Chapter 6 described the results of the field tests. It was found that:

• The methodology is robust for field deployment;

• Temperature plays an important role in the quantitative measurement of the damage index ratios;

• The Raindrops may cause false positives.

APPENDIX A

TRUSS INFORMATION FOR LABORATORY TEST

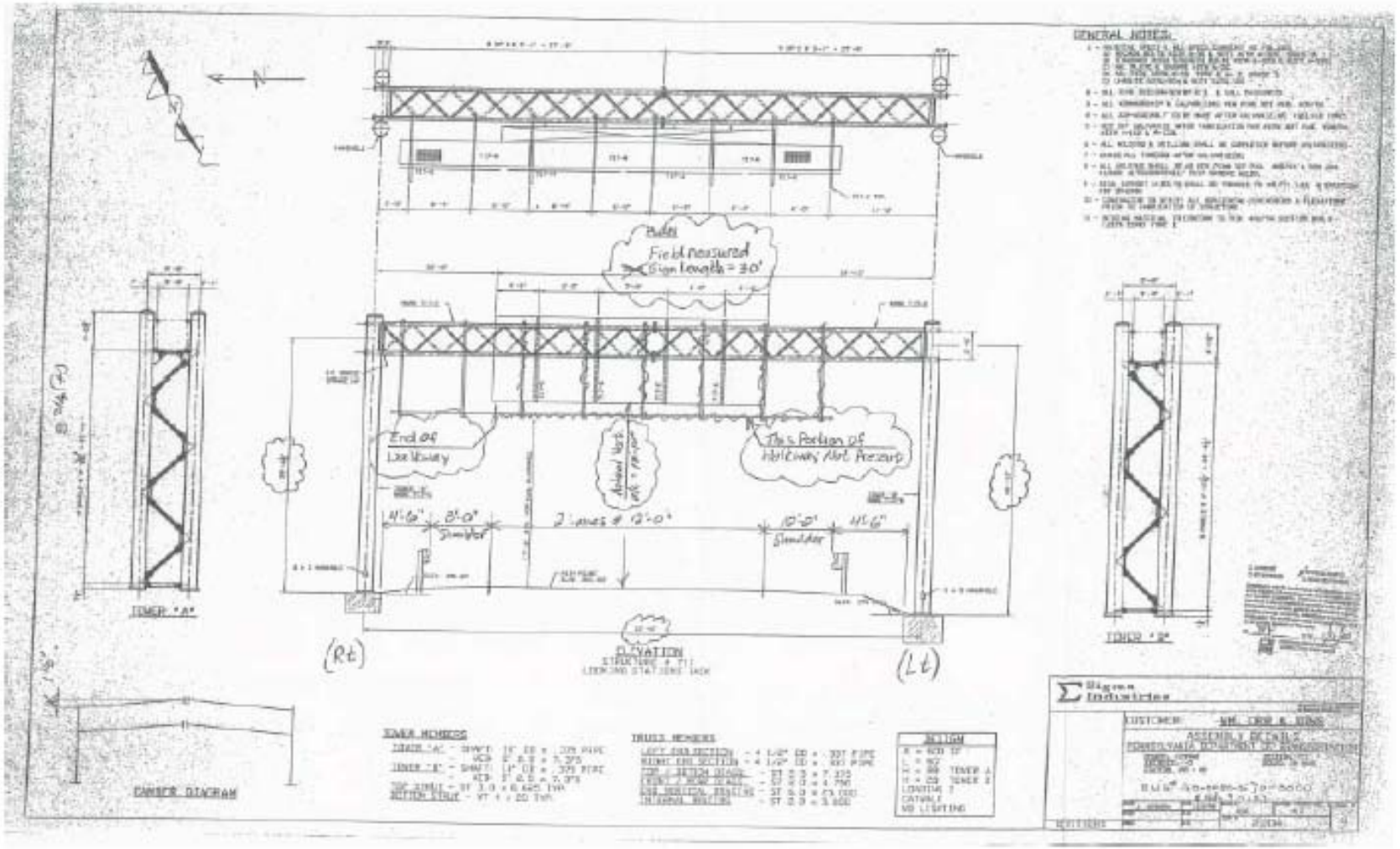
GENERAL NOTES:
Field measured Sign length = 30'
End of Luminary
This Portion of Walkway Not Present
4'-6"
8'-0"
Shoulder
2 lanes @ 12'-0"
10'-0"
Shoulder
4'-6"
TOWER "A"
TOWER "B"
ELEVATION
(Rt)
(Lt)
TOWER DIAGRAM
TOWER MEMBERS
TRUSS MEMBERS
SECTION
Sign Industries

APPENDIX B

TRUSS INFORMATION FOR FIELD TEST 1

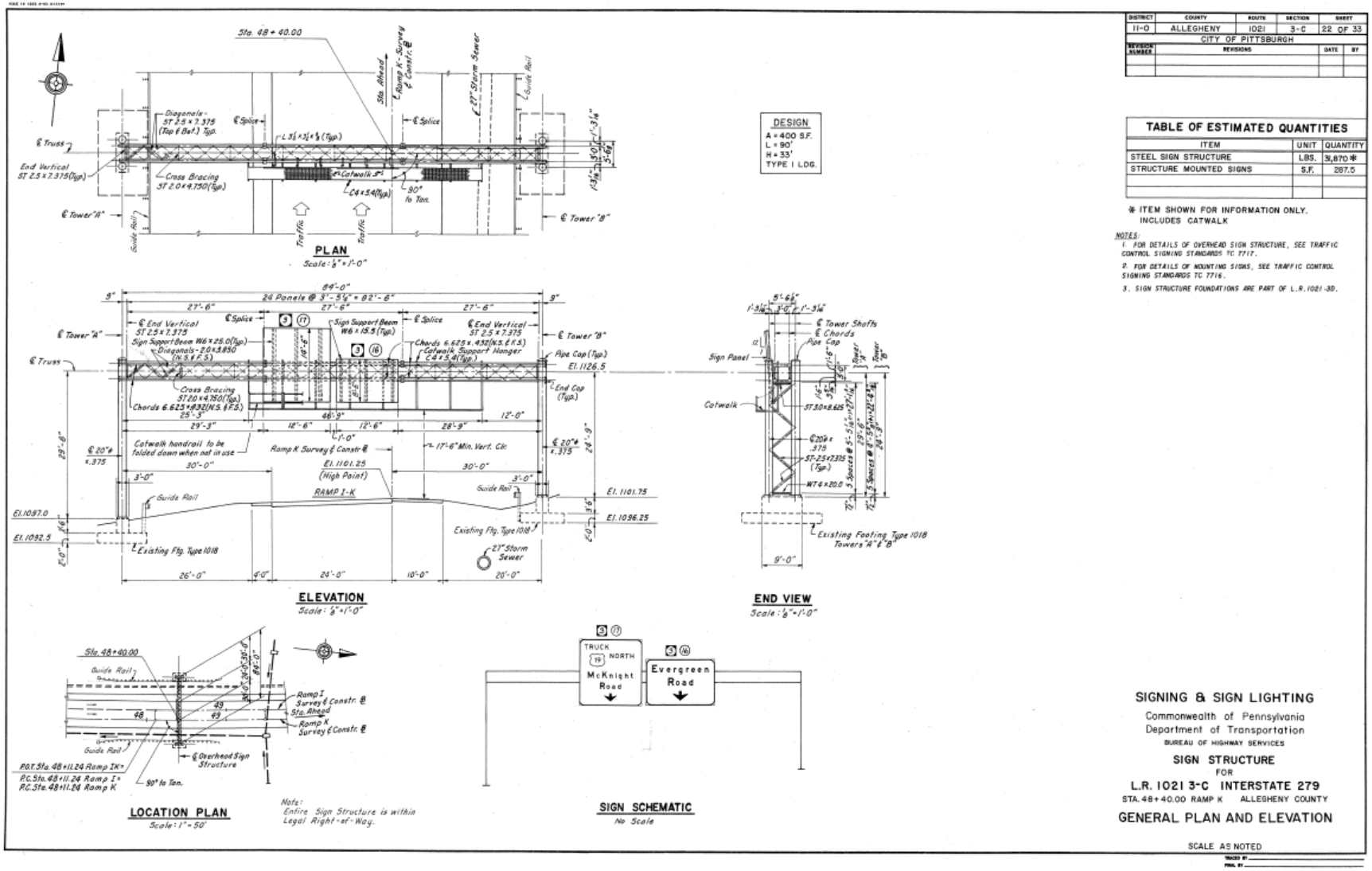

DISTRICT	COUNTY	ROUTE	SECTION	SHEET
11-0	ALLEGHENY	1021	3-C	22 OF 33

CITY OF PITTSBURGH

REVISION NUMBER	REVISIONS	DATE	BY

TABLE OF ESTIMATED QUANTITIES

ITEM	UNIT	QUANTITY
STEEL SIGN STRUCTURE	LBS.	36,870 *
STRUCTURE MOUNTED SIGNS	S.F.	287.5

* ITEM SHOWN FOR INFORMATION ONLY. INCLUDES CATWALK

NOTES:
1. FOR DETAILS OF OVERHEAD SIGN STRUCTURE, SEE TRAFFIC CONTROL SIGNING STANDARDS TC 7717.
2. FOR DETAILS OF MOUNTING SIGNS, SEE TRAFFIC CONTROL SIGNING STANDARDS TC 7716.
3. SIGN STRUCTURE FOUNDATIONS ARE PART OF L.R. 1021-3D.

SIGNING & SIGN LIGHTING

Commonwealth of Pennsylvania
Department of Transportation
BUREAU OF HIGHWAY SERVICES

SIGN STRUCTURE
FOR
L.R. 1021 3-C INTERSTATE 279
STA. 48+40.00 RAMP K ALLEGHENY COUNTY

GENERAL PLAN AND ELEVATION

SCALE AS NOTED

TRACED BY
FINAL BY

APPENDIX C

TRUSS INFORMATION FOR FIELD TEST 2

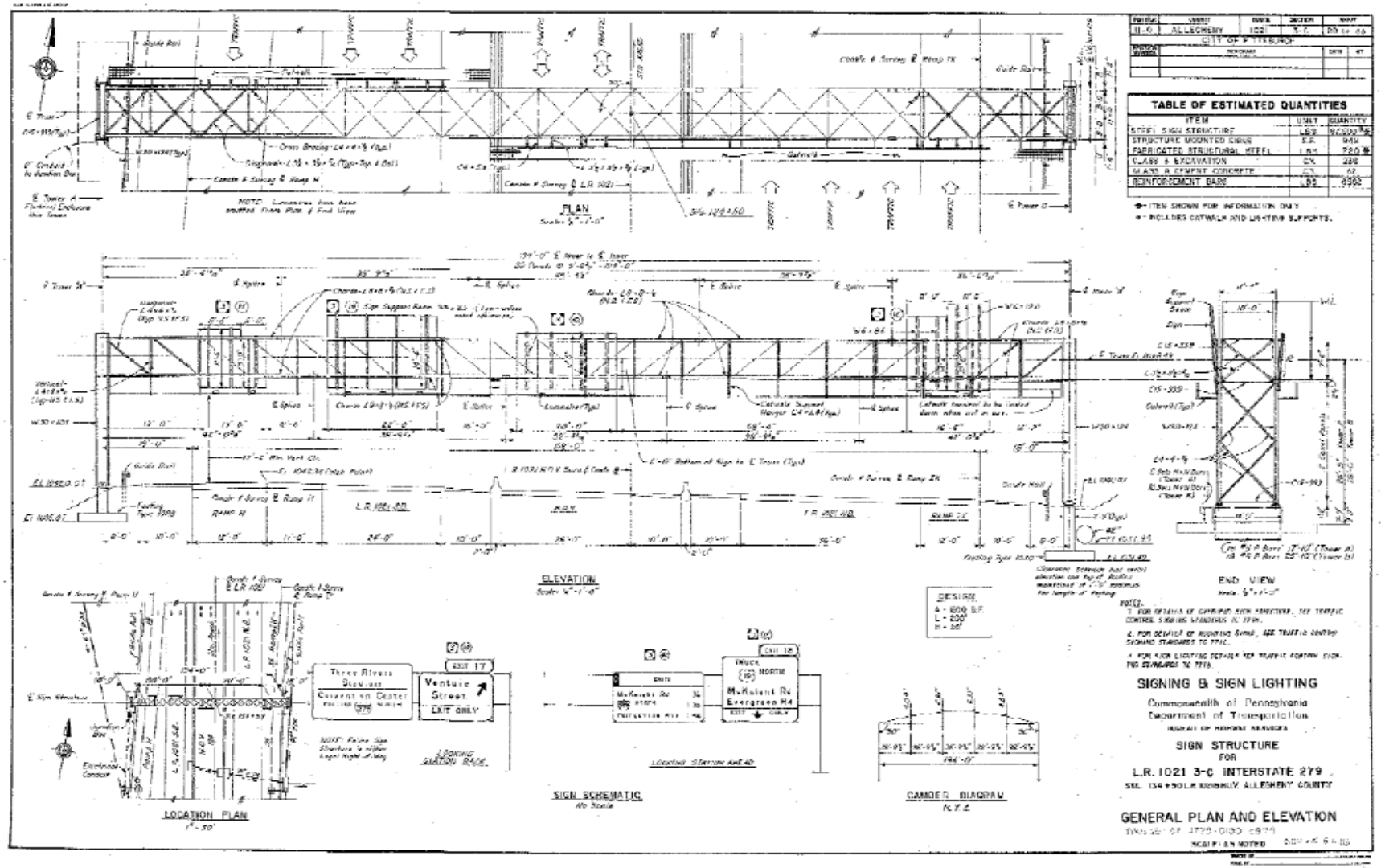
TABLE OF ESTIMATED QUANTITIES
ITEM | UNIT | QUANTITY
STEEL SIGN STRUCTURE | LBS. | 97,000 *
STRUCTURE MOUNTED SIGNS | S.F. | 945
FABRICATED STRUCTURAL STEEL | LBS. | 780 **
CLASS B EXCAVATION | C.Y. | 236
CLASS B CEMENT CONCRETE | C.Y. | 62
REINFORCEMENT BARS | LBS. | 6963
* ITEM SHOWN FOR INFORMATION ONLY
** INCLUDES CATWALK AND LIGHTING SUPPORTS.
PLAN
ELEVATION
END VIEW
LOCATION PLAN
SIGN SCHEMATIC
CAMBER DIAGRAM
SIGNING & SIGN LIGHTING
Commonwealth of Pennsylvania
Department of Transportation
SIGN STRUCTURE
FOR
L.R. 1021 3-C INTERSTATE 279
SEC. 134 ROUTE 1021 ALLEGHENY COUNTY
GENERAL PLAN AND ELEVATION

BIBLIOGRAPHY

[1] Standard Specifications for Structural Supports for Highway Signs, Luminaires, and Traffic Signals, 4th Edition. American Association of State Highway and Transportation Officials (AASHTO).Washington, D.C., 2001.

[2] Dexter, R.J. and Ricker, M.J.. "Fatigue Resistant Design of Cantilevered Signal, Sign andLight Supports." NCHRP Report 469, Transportation Research Board, Washington, D.C., 2002.

[3] Ginal, S.. "Fatigue Performance of Full-Span Sign Support Structures Considering Truck Induced Gust and Natural Wind Pressures." MSCE thesis, Marquette University, Milwaukee, WI, 2003.

[4] Guidelines for the Installation, Inspection, Maintenance, and Repair of Structural Supports for Highway Signs, Luminaires, and Traffic Signals. Federal Highway Administration (FHWA), 2005.

[5] Dexter, R. J., K. Johns, and R. Di Bartolo. "Smart Sign Support." Civil Engineering, Nol. 70, No. 9, pp. 62-65. , 2000.

[6] Standard Specifications for Structural Supports for Highway Signs, Luminaires, and Traffic Signals. American Association of State Highway and Transportation Officials (AASHTO). With Interims, Washington, D.C., 1994.

[7] Mix, P.E.. Introduction to nondestructive testing : a training guide, 2nd ed.. Hoboken, N.J. Wiley Interscience, 2005.

[8] Kessler, S. S., Spearing, S. M., Attala, M. J., Cesnik, C. E. S. and Soutis, C.. "Damage Detection in Composite Materials Using Frequency Response Methods." Composites, Part B: Engr., 33, 87-95, 2002.

[9] Boller C.. "Structural Health Management of Ageing Aircraft and Other Infrastructure." Monograph on Structural Health Monitoring, Institute of Smart Structures and Systems, 1-59, 2002.

[10] Bhalla, S. (2004). "A Mechanical Impedance Approach for Structural Identification, Health Monitoring and Non-Destructive Evaluation Using Piezo-Impedance Transducers" Ph.D Thesis, Nanyang Technological University, Singapore.

[11] Shull P. J.. Nondestructive Evaluation – Theory, Techniques, and Applications. Marcel Dekker, 2002.

[12] TWI 2008 http://www.twi.co.uk/content/ksijm001.html, last access July 10th 2008.

[13] Farrar, C.. "Structural Health Monitoring" class notes, Univ. of California, San Diego, 2002.

[14] Pelletier E, Grenier M, Chahbaz A and Bourgelas T.. "Array Eddy current for Fatigue Crack Detection of Aircraft Skin Structures." Proc., 5th Intl. Workshop, Advances in Signal Processing for Non Destructive Evaluation of Materials, Québec City, Canada, 85-92, 2006.

[15] Diaz A.A., Mathews R.A., Hixon J. Doctor S.R.. "Assessment of Eddy Current Testing for the Detection of Cracks in Cast Stainless Steel Reactor Piping Components." U.S. Nuclear Regulatory Commission Washington, DC 20555-0001, NRC Job Code Y6604, 2007.

[16] Lamtenzan D, Washer G, and Lozev M.. "Detection and Sizing of Cracks in Structural Steel Using the Eddy Current Method." US Department of Transportation, Federal Highway Administration, McLean, VA, FHWA-RD-00-018, 2000.

[17] Laubach M, Montgomery M, Cope D.. "Summary and Comparison Report on Teardown Evaluation of Cessna 402A and Cessna 402C Airplanes." U.S. Department of Transportation, Federal Aviation Administration DOT/FAA/AR-07/35, 2007.

[18] Balaskó, M., Sváb, E., Kuba, A., Kiss, Z., Rodek, L., and Nagy, A.. "Pipe corrosion and deposit study using neutron-and gamma-radiation sources." Nuclear Institute and Methods in Physics Research, A., 2005.

[19] Wang, P.. "Acoustic Emission Testing and FEA of Cantilevered Traffic Signal Structures." Mater thesis, University of Wyoming, 1999.

[20] Liang, C., Sun, F. P. and Rogers, C. A.. "Coupled electromechanical analysis of adaptive material systems- determination of the actuator power consumption and system energy transfer." Journal of Intelligent Material Systems and Structures, 5(1), 12-20, 1994.

[21] Sun, F. P., Chaudry, Z., Rogers, C. A., Majmundar, M. and Liang, C.. "Automated real-time structure health monitoring via signature pattern recognition." Proc., Smart Structures Materials Conference, San Diego, California, SPIE, 2443, 236-247, 1995.

[22] Wetherhold, R.; Messer, M.; Patra, A.. "Optimization of directionally attached piezoelectric Actuators." J. Engr. Mat. Techn., Vol 125, pp.148-152, 2003.

[23] Giurgiutiu, V., Reynolds, A. and Rogers, C. A.. "Details of the Electro-Mechanical (E/M) Impedance Health Monitoring of Spot-Welded Structural Joints." SPIE 6th Annual International Symposium on Smart Structures and Materials, Newport Beach, CA, Paper 3668-34, 1999.

[24] Hoon T, Toshihiko M, Tang C.K and Chiu W.K. “Fatigue Crack Detection Using Piezoelectric Elements.” SIF 2004 Structural Integrity and Fracture,1999. http://eprint.uq.edu.au/archive/00000836

[25] Xing K. J and. Fritzen C.P.. “Monitoring of Growing Fatigue Damage Using the E/M Impedance Method.” Key Engineering Materials, Vol. 347, pp 153-158, 2007.

[26] Park, G., Sohn, H., Farrar, C. R. and Inman, D. J.. “Overview of Piezoelectric Impedance-Based Health Monitoring and Path Forward.” The Shock and Vibration Digest, SAGE Publications, 35(6), 451-463, 2003.

[27] Connor, R.J.. “Draft Final Report – Results of the Investigation into the Cause of the Observed Cracking on VMS Support Structures in Penn DOT District 4-0.” Draft Final Report - Results of the Investigation into the Cause of the Observed Cracking on VMS Support Structures in Penn DOT District 4-0, 2008.

[28] Lanza di Scalea, F. and Salamone, S.. “Artificial Wind Generation and Structural Response.” J. Acoust. Soc. Am., Vol. 124, No. 1, 161-174, 2008.